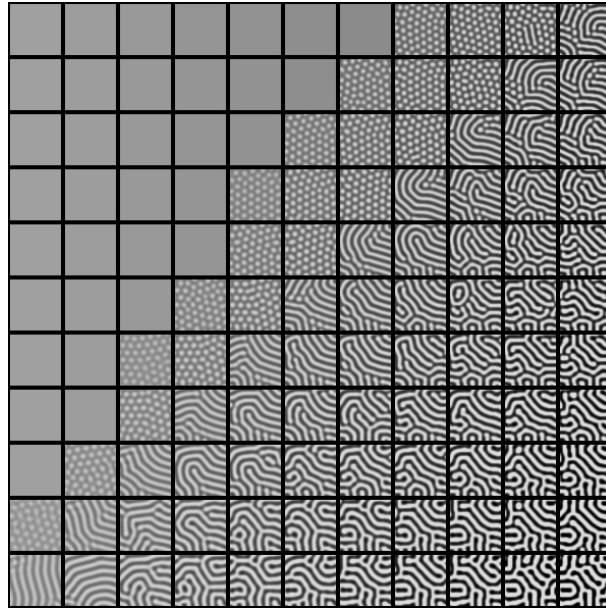


Morphology of Experimental and Simulated Turing Patterns



Diplomarbeit

von

Christian Scholz

Erlangen,
August 2009

Friedrich-Alexander-Universität zu Erlangen-Nürnberg
Lehrstuhl für Theoretische Physik I
Prof. Dr. Klaus Mecke

Zusammenfassung

Chemische Nichtgleichgewichtsprozesse, bei denen sich durch Diffusion und Reaktion sogenannte *Turing Muster* bilden, also heterogene Konzentrationsprofile, sind als Modell für spontane Musterbildung bekannt. In dieser Arbeit werden derartige Muster aus der Chlorit-Iodid-Malonsäure (CIMA) Reaktion mit Turing Mustern quantitativ verglichen, die man aus dem numerischen Modell von Lengyel und Epstein (LE) erhält. Dieses Modell basiert auf einer nichtlinear partiellen Differentialgleichung, die die CIMA Reaktion vereinfacht beschreiben soll.

Eine quantitative morphologische Analyse mittels Minkowski Funktionalen, die durch die Arbeit von Mecke (PRE, 53(5)) inspiriert ist, zeigt signifikante Unterschiede zwischen den Konzentrationsprofilen in den Mustern der CIMA Reaktion und des LE Modells. Dies weist darauf hin, dass das deterministische LE Modell, obwohl es den grundlegenden Charakter der CIMA Reaktion reproduziert, nicht die richtigen Konzentrationsprofile erzeugt.

Die im Experiment gemessenen Muster sind als 2D Graustufenbilder gegeben. Die Konzentrationsprofile aus dem LE Modell erhält man durch die numerische Lösung des zugehörigen Reaktions-Diffusions Systems.

Minkowski Funktionalen sind morphologische Maße aus der Integralgeometrie, mit denen sich Graustufenbilder morphologisch charakterisieren lassen. Die Analyse zeigt, dass CIMA und LE Muster in allen Minkowski Funktionalen Unterschiede zeigen, wenn größere Bildausschnitte der experimentellen Muster betrachtet werden. In einer lokalen Analyse, d.h. für geordnete Teilbereiche der experimentellen Muster, ergeben sich jedoch Übereinstimmungen zwischen den Mustern. Die Möglichkeit, dass additives Gaußsches weißes Rauschen die Unterschiede zwischen numerischen und experimentellen Mustern erklärt wurde ausgeschlossen.

Ein erweitertes Modell, das auf der statistischen Überlagerung von stationären Mustern aus dem LE Modell basiert, erzeugt Muster mit einer guten morphologischen Übereinstimmung mit den experimentellen Konzentrationsprofilen und reproduziert zusätzlich die Morphologie der turbulenten Muster, die in der CIMA Reaktion von Ouyang und Swinney gefunden wurden (Chaos, 1(4)). Dies weist darauf hin, dass turbulente Muster als dynamische Überlagerung von grundlegenden Mustern verstanden werden können.

Abstract

Turing patterns formed in the chlorite-iodide-malonic acid (CIMA) reaction, a far from equilibrium chemical reaction-diffusion system, are morphologically compared to patterns obtained in the Lengyel-Epstein (LE) model, which is based on a non-linear partial differential equation and believed to model the CIMA reaction.

A quantitative morphological analysis via Minkowski functionals, inspired by the work of Mecke (PRE, 53(5)), shows significant differences between the concentration profiles of patterns in the CIMA reaction and the LE model. This indicates that the deterministic LE model, while reproducing the basic character of the CIMA reaction, does not reproduce the correct concentration profiles.

The concentration profiles measured in the experiment are given as 2D greyscale images for the CIMA reaction. The LE concentration profiles are obtained by solving the corresponding reaction-diffusion equation numerically using a finite-difference method.

Minkowski functionals are morphological measures from integral geometry and characterize the morphology of greyscale images. Our analysis shows that the CIMA and LE patterns differ in all Minkowski functionals, when extended fractions of patterns are analyzed. However a local agreement between crystalline, i.e. more ordered parts of the experimental patterns, and the patterns obtained in the LE model is found. We have excluded the possibility that additional additive white noise in the reaction-diffusion equations leads to an agreement of numerical and experimental patterns.

An extended model based on the statistical superposition of basic patterns obtained from the LE model produces patterns with a good morphological agreement to the experimental hexagonal and lamellar Turing patterns. It also reproduces, for the first time, the morphology of the turbulent phase, identified by Ouyang and Swinney (Chaos, 1(4)). This indicates that turbulent patterns could be described as a dynamically fluctuating superposition of basic patterns.

Danksagung

Zunächst möchte ich mich im besonderen bei Herrn Dr. Gerd Schröder-Turk und Prof. Dr. Klaus Mecke für die ausgezeichnete Betreuung der Diplomarbeit, die Beantwortung zahlreicher Fragen und die vielen hilfreichen Anregungen bedanken. Ich danke außerdem den Mitarbeitern des Lehrstuhls für Theoretische Physik I für die vielen Diskussionen und die freundliche Arbeitsatmosphäre. Im besonderen bedanke ich mich bei Sebastian Kapfer für die Hilfe bei der 2D Minkowski Analyse mit seinem Programm “papaya”, bei Stephanie Häffner und Daniel Göring für die numerischen und analytischen Vorarbeiten, bei Markus Spanner für die Hilfe bei der Berechnung der covering radius transform, Herrn Prof. Dr. Hajo Leschke für Anregungen zu den stochastischen partiellen Differentialgleichungen, sowie Johannes Reinhard und Christian Goll für die Hilfe bei Bash-Script und Latex Problemen. Den System-Admins Sebastian Kapfer, Johannes Reinhard und Christian Goll danke ich auch für die gut funktionierende Computer-Architektur.

Weiterhin bedanke ich mich bei Herrn Prof. Dr. Jan-Peter Meyn und den Mitarbeitern des Lehrstuhls für Didaktik der Physik für die Hilfsbereitschaft zum Versuch über Muster in geschüttelter granularer Materie. Dort, sowie bei allen anderen Helfern, bedanke ich mich auch für die gesamte Zusammenarbeit während der Vorbereitung zur Weihnachtsvorlesung, für die dieser Versuch ursprünglich aufgebaut wurde.

Bei Herrn Dr. Qi Ouyang und Herrn Prof. Dr. Harry Swinney bedanke ich mich für die originalen Daten der CIMA Reaktion, die ich über Herrn Mecke erhalten habe. Außerdem bedanke ich mich bei Herrn Patrick De Kepper für zusätzliche experimentelle Daten der CDIMA Reaktion.

Großer Dank gilt außerdem Sandy für viel Hilfe, Geduld, Verständnis und Durchhaltevermögen und meinen Eltern, auf deren Hilfe ich mich immer und uneingeschränkt verlassen konnte.

Contents

1	Introduction	11
1.1	Turing patterns in chemical systems	11
1.2	Previous analysis of Turing pattern formation	12
1.3	Morphological analysis with Minkowski functionals	14
1.4	Pattern formation in other systems	14
2	Turing patterns in the CIMA reaction	17
2.1	Experimental Setup	17
2.2	Lengyel-Epstein (LE) model for the CIMA reaction	20
2.2.1	Derivation of the reaction-diffusion equations	20
2.2.2	Linear Stability Analysis	22
2.3	Other reaction-diffusion models	25
3	Numerical solution of 2D reaction-diffusion equations	27
3.1	Explicit finite difference scheme	27
3.2	Semi-implicit Crank-Nicolson scheme	29
3.3	Von Neumann stability analysis	32
3.3.1	Explicit finite difference scheme	32
3.3.2	Semi-implicit Crank-Nicolson scheme	33
3.4	Convergence to stationary patterns	35
3.5	Discretization of stochastic partial differential equations	37
4	Patterns in the Lengyel-Epstein model	39
4.1	Parameter-space of the Lengyel-Epstein model	39
4.1.1	Stationary solutions	39
4.1.2	Oscillatory solutions	48
4.2	Concentration fluctuations of stable homogeneous states	48
5	Morphology of experimental and numerical Turing patterns	51
5.1	Minkowski analysis for 2D images	51
5.1.1	Minkowski functionals for bodies in \mathbb{E}^2	51
5.1.2	Minkowski functionals for pixelized images	52
5.1.3	Analysis of greyscale images and length scale normalisation	53
5.2	Minkowski functionals of patterns in the CIMA reaction	55
5.3	Minkowski functionals of simulated patterns in the LE model	60
5.4	Local Minkowski functionals of patterns in the CIMA reaction	66

5.5	Minkowski-maps of patterns in the CIMA reaction	72
5.6	Minkowski analysis of the CDIMA reaction (De Kepper et al.) . . .	75
5.7	Minkowski functionals of patterns in other reaction-diffusion models	78
6	Influence of additive noise on pattern formation in the LE model	81
6.1	Influence on pattern stability	81
6.2	Influence on convergence	82
6.3	Influence of noise on pattern morphology	82
7	Statistical ensemble of superposed basic patterns	87
7.1	A simple model with superposition of patterns	87
7.2	Minkowski analysis for superposed patterns	90
7.2.1	Hexagonal state	90
7.2.2	Lamellar state	92
7.2.3	Turbulent state	92
7.3	Interacting pattern gas	97
7.3.1	Derivation of the interaction energy	97
7.3.2	Second order approximation	98
7.3.3	Numerical results	99
7.4	Conclusion	100
8	Summary and outlook	103
9	Pattern formation in granular systems	105
9.1	Experimental setup	105
9.2	Measurements and observed patterns	106
A	Details on experimental datasets	109

Chapter 1

Introduction

1.1 Turing patterns in chemical systems

In 1952 Alan Turing proposed a model for biological pattern formation, which is based on the reaction and diffusion of so-called morphogenes in biological tissue and can be described mathematically by a reaction-diffusion partial differential equation [61]. The concentrations of the morphogenes vary spatially, i.e. form a stationary pattern. Counter-intuitively these patterns occur not despite but because of the diffusion, although diffusion often has a smoothing effect.

Turing mainly analyzed linear reaction kinetics and focused his numerical research on a one dimensional system, i.e. a ring of 20 cells, which was the largest system that he could probably handle numerically in 1952 on “the Manchester University Computer”. In his paper he also argued that although a complete mathematical analysis could be done for the ring of cells, “the computational treatment of a particular case was most illuminating” [61]. Turing analyzed the divergence or convergence of different modes in his linearized model. However for complex stationary patterns he knew that nonlinear terms would have to be taken into account to prevent diverging concentrations. In his paper he suggests the use of “a digital computer” to do extensional work with nonlinear reaction terms. Unfortunately Ref. [61] was Turing’s last publication before his death in 1954.

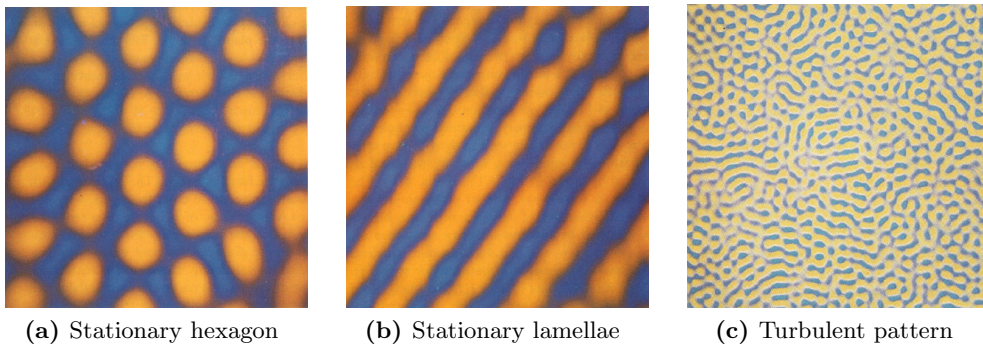


Figure 1.1: Turing patterns found by Ouyang and Swinney. Stationary hexagonal and lamellar patterns, as well as turbulent patterns are reported. (Images are reproduced from Ref. [47])

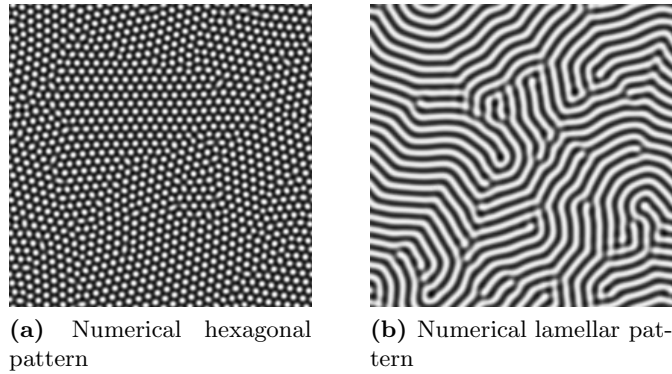


Figure 1.2: Stationary Turing patterns obtained as numerical solutions in the LE model.

In 1971 Prigogine and his group proposed a new nonlinear reaction-diffusion system, the so-called Brusselator and studied it quantitatively [16]. The numerical analysis of the model showed that pattern formation occurred in a one dimensional system. Other models were proposed afterwards with applications in biological systems such as the Schnakenberg, Gierer-Meinhardt, FighHugh-Nagamo and Gray-Scott model and led to a variety of numerical and analytical analyses of pattern formation in two- and three-dimensional reaction-diffusion systems, see Refs. [6, 11, 14, 43, 44, 49] for examples.

However it took another 20 years until in 1990 first evidence of stationary Turing pattern formation in a chemical system, the so-called CIMA reaction, was reported by Castets et al. [7]. The experiment consisted of a continuously fed thin agarose gel stripe, into which chemicals can diffuse but convection currents are suppressed, resulting in a pure reaction-diffusion system. Another reactor used by Ouyang and Swinney in 1991 led to the observation of stationary hexagonal and lamellar as well as turbulent Turing patterns [47], such as shown in Fig. 1.1.

A corresponding reaction-diffusion model, which is used in this thesis for numerical analysis was proposed by Lengyel, Rabai and Epstein in 1990 and is referenced to as the Lengyel-Epstein (LE) model [30]. In contrast to phenomenological models the LE model is derived directly from a simplified description of the reaction kinetics of the CIMA reaction.

1.2 Previous analysis of Turing pattern formation

Investigations have shown good qualitative agreement of stationary patterns in the LE model, as shown in Fig. 1.2, and patterns in the CIMA reaction as far as pattern types and wavelengths are concerned for regions of the parameter space, where the simplifications of the LE model are justified [25, 54]. A full linear stability analysis with numerical analysis of possible localized structures can be found in Ref. [21]. The dimensionality of the patterns, i.e. the actual three-dimensional structure

of the experimental quasi-2D patterns is analyzed in Ref. [12, 46, 55], where also spatio-temporal effects due to interactions of different Turing patterns in the three dimensional system are analyzed and a simple resonance of patterns has also been discussed in Ref. [17] to explain the formation of rhombic and black-eyed patterns. The possibility of spatio-temporal patterns in the LE model is discussed in Ref. [53], where spatio-temporal patterns are found as oscillating hexagonal patterns in a very small region of the parameter space. However no theoretical model which reproduces the turbulent patterns reported in Ref. [47] has been found yet. Although spatio-temporal patterns could be obtained in coupled reaction-diffusion systems no evidence of similar turbulence is found in any model based on deterministic partial differential equations [67].

The effect of noise on Turing pattern formation in a generic reaction-diffusion system has been studied by Leppänen in Ref. [33] and patterns have been found to be very robust against noise. The robustness of pattern formation against noise is also confirmed for the LE model in chapter 6 in this thesis.

The usual approaches to obtain information about spatial structures such as Turing patterns are Fourier transformations and autocorrelation functions [47]. Whereas these methods provide useful information about ordered patterns like the characteristic wavelength they can be insufficient for characterizing more irregular structures. Figure 1.3 shows two hexagonal concentration profiles and a one-dimensional cross-section, where the grey-value is shown. Although both patterns have the same wavelength there are obvious morphological differences.

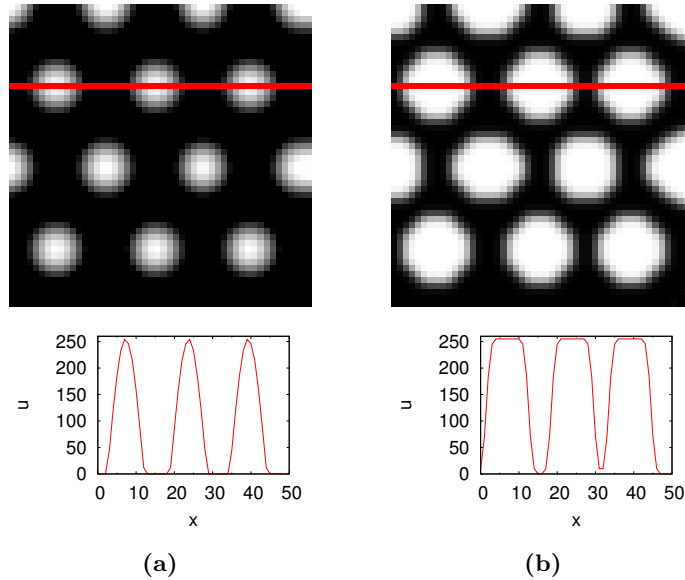


Figure 1.3: Two artificial hexagonal patterns with the same wavelength but morphologically different concentration profiles. The line in the images indicates the cross-section shown below.

1.3 Morphological analysis with Minkowski functionals

A quantitative approach to characterize and compare experimental and numerical patterns is given by the so-called Minkowski functionals. Minkowski functionals are measures from integral geometry and can be used to characterize the morphology of greyscale images [38]. Minkowski functionals are useful to describe irregular structures, as they give a measure of the connectivity of domains in the image. Recent applications include the characterization of spinodal decompositions in thin polymer films during dewetting processes in Ref. [35] and the characterization of structure formation in thin films of cylinder forming block copolymers [51].

A Minkowski analysis for the experimental patterns has been done by Mecke [37], who showed that the transition of experimental patterns in the CIMA reaction can be described by symmetry breaking in certain coefficients that describe the functional form of the Minkowski functionals. The analysis in this thesis is an application of this method to experimental and simulated Turing patterns.

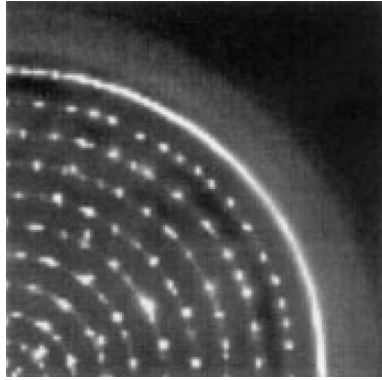
1.4 Pattern formation in other systems

Apart from the CIMA reaction, only two other chemical systems which produce stationary patterns under laboratory conditions have been found. One is the iodate-ferrocyanide-sulfite (FIS) reaction, which produces patterns under finite amplitude perturbations, see Ref. [24], and the recently discovered thiourea-iodate-sulfite (TuIS) reaction in Ref. [19], where a general design scheme for pattern forming chemical reactions is proposed. Another non-biological system with Turing pattern formation was reported in silver/antimony electrodeposits on surfaces [56].

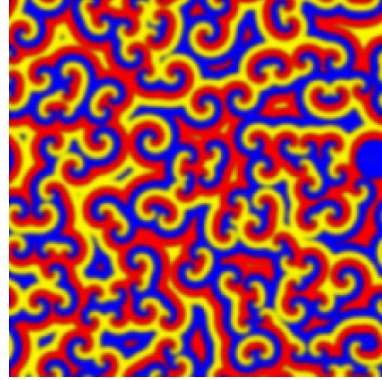
Following Turing's original idea reaction-diffusion equations are used to describe pattern formation in biological organisms such as hydra in Ref. [15] or the spread of brain tumors in Ref. [44] and bacterial patterns as described in Ref. [62] and shown in Fig. 1.4a. Furthermore reaction-diffusion equations can successfully model spatial population dynamics in predator-prey systems, where finite-size effects give rise to additive noise that influences pattern formation, such as shown in Fig. 1.4b and analyzed in recent work by Reichenbach et al. [52].

Nonlinear pattern formation can also be seen in ferromagnetic fluids in external magnetic fields, known as Rosensweig-instability [8]. Other mechanisms of pattern formation include self-organization of block co-polymers, which separate into distinct domains that can form ordered patterns or the formation of fractal branch structures by diffusion-limited aggregation [5].

Another mechanism of pattern formation was found in vertically shaken granular media, as reported in Ref. [39]. A similar system with a variety of patterns, such as shown in Fig. 1.5, is analyzed in this thesis. It is the simplicity of the experimental system, which only consists of a thin layer of beads and a driving plate, which makes them particularly interesting.



(a) “Bacteria” in a reaction-diffusion model forming concentric rings with region of high cell density (white) and low cell density (black). (Image reproduced from Ref. [62])



(b) Steady spiral state in a noisy three species cyclic competition model. Each color represents one of the three species. (Image reproduced from Ref. [52])

Figure 1.4: Pattern formation in ecological systems, such as bacteria and species competition. Such systems can be described by reaction-diffusion equations, which show spatial patterns formation.

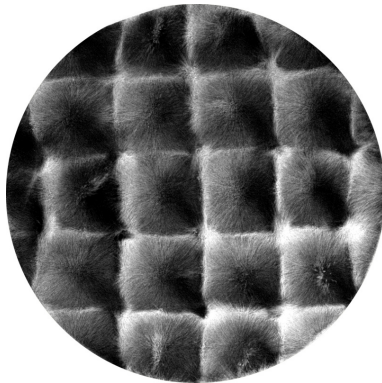


Figure 1.5: Square and stripe patterns in vertically shaken granular media, see chapter 9.

Chapter 2

Turing patterns in the CIMA reaction

The so-called CIMA reaction that involves chlorite-iodide and malonic acid, was the first experimental realization of a Turing pattern forming system. The Lengyel-Epstein (LE) model is the corresponding albeit simplified reaction-diffusion (RD) partial differential equation that is believed to describe the CIMA reaction at a phenomenological level. While the LE model is truly two-dimensional, the experimental CIMA setup is a thin, but three-dimensional system. This chapter describes the experimental setup of the CIMA system and derives the LE reaction-diffusion equations. A linear stability analysis for the LE partial differential equations is given that determines the parameters for which pattern formation is expected.

2.1 Experimental Setup

The first evidence of Turing Pattern formation in a chemical reaction under controlled laboratory conditions was reported in 1990 by Castets et al. [7]. The experiments were conducted for a chlorite-iodide-malonic acid (CIMA) reaction within a cooled gel-strip reactor loaded with a starch indicator. The formation of hexagonal and lamellar structures observable in the concentration profile of a blue starch-triiodide complex within a thin band in the reactor was found, as shown in Fig. 2.1. In Castets' setup, chlorite, iodide and malonic acid diffuse into the gel strip from two compartments A and B. Consequently a chemical concentration gradient forms in the reactor with a thin region where the concentrations correspond to the necessary conditions for Turing instabilities.

In 1991 Ouyang and Swinney measured quasi two-dimensional stationary hexagonal and lamellar Turing patterns in the CIMA reaction in an open two-sided gel disk reactor, see Fig. 2.2a. They also observed non-stationary turbulent patterns, referred to as *chemical turbulence* [47]. Representative patterns of all three states are shown in Fig. 2.3.

In Ouyang's setup, chlorite, iodide and malonic acid are continuously supplied through compartments A and B, where they are transparent. Similarly to Castets' gel-strip reactor the reactants diffuse into the gel reactor, which is shown schematically in Fig. 2.2b. Therein a chemical concentration gradient forms and for the appropriate concentrations, a region of Turing instability forms. In contrast to

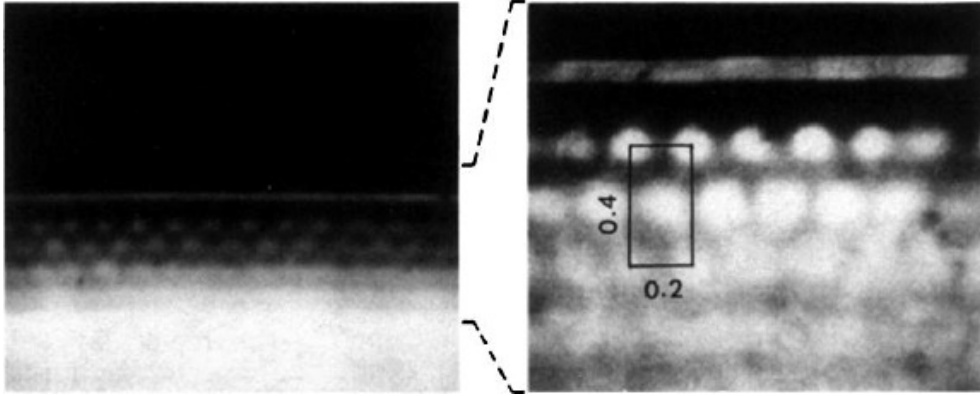


Figure 2.1: First evidence for Turing Pattern formation in a gel-strip reactor. The reactants diffuse into the gel-strip from compartment on the sides (i.e. top and bottom in the image). The pictures are side-views of the Turing structures, i.e. perpendicular to the concentration gradient in the gel-strip. (Image reproduced from Ref. [7])

Castets' gel-strip reactor the gel in Ouyang's experiment is thinner and viewed from the top, which results in observable extended quasi two-dimensional Turing patterns.

The dimensionality of patterns was discussed in Ref. [46], which showed that the patterns obtained in Ref. [47] were two-dimensional. However three-dimensional patterns are possible for different configurations, as shown in Ref. [12]. Numerical analysis of three-dimensional Turing patterns can be found in Ref. [58], where also a periodic minimal surface, the gyroid, is found as a solution. An advanced setup that shares the same principle, the open one-sided gel disk reaction, was used in later experiments to avoid effects of to the actual three-dimensional structure of the reactor [54]. In the case of three-dimensional Turing structures the observed quasi two-dimensional patterns consist of the spatial average of all layers of patterns in the system. The occurrence of rhombic patterns, traveling waves and spatio-temporal patterns, different from those observed in Ref. [47] has been attributed to the three-dimensional structure of the experiment [55]. However rhombic patterns were also predicted for quasi two-dimensional systems [45]. A small region with a rhombic array can even be found in the top right corner of the hexagonal pattern of Fig. 2.3 and the occurrence of rhombic patterns in the CIMA reaction was further verified in Ref. [17].

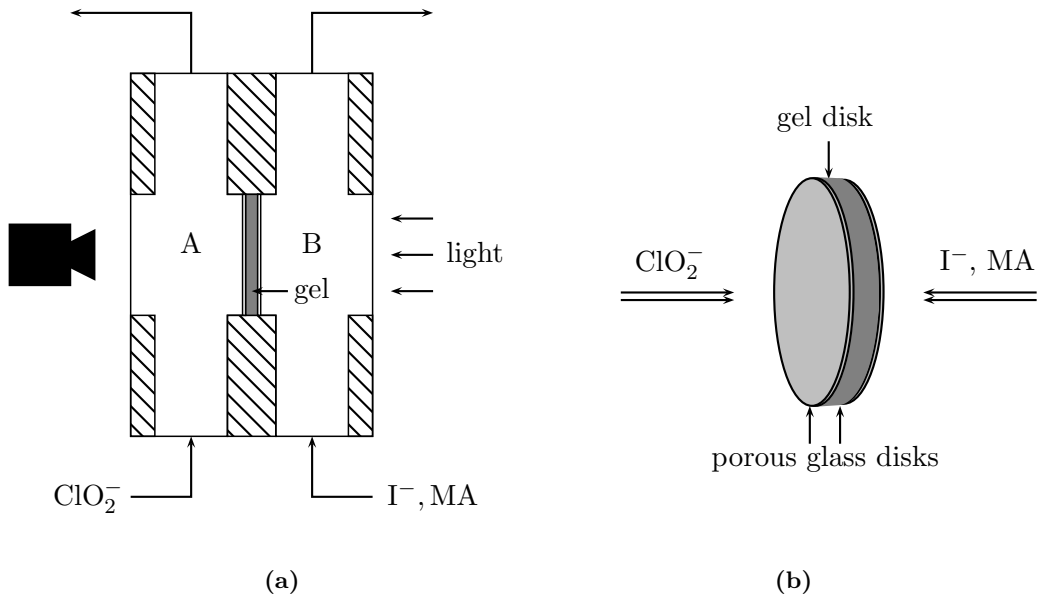


Figure 2.2: (a) Experimental setup of a two-sided gel reactor, such as used in Ref. [47]. A cross section of the cylindrical device is shown. The gel-reactor, where the pattern formation occurs separates compartments A and B, from where the chemicals diffuse into the gel. All individual reactants are transparent in the compartments. A concentration gradient forms in the gel with a region of pattern formation for sufficient concentrations of the reactants in the compartments. (b) The gel-reactor, as shown in Fig. 2.2a consists of a thin gel disk (2 mm) in between two porous glass disks, which separate the gel from the compartments A and B to prevent stirring effects of fluid convection. The reactants can diffuse into the gel, where a concentrations gradient forms. For sufficient temperature and concentrations in the compartments pattern formation can be observed.

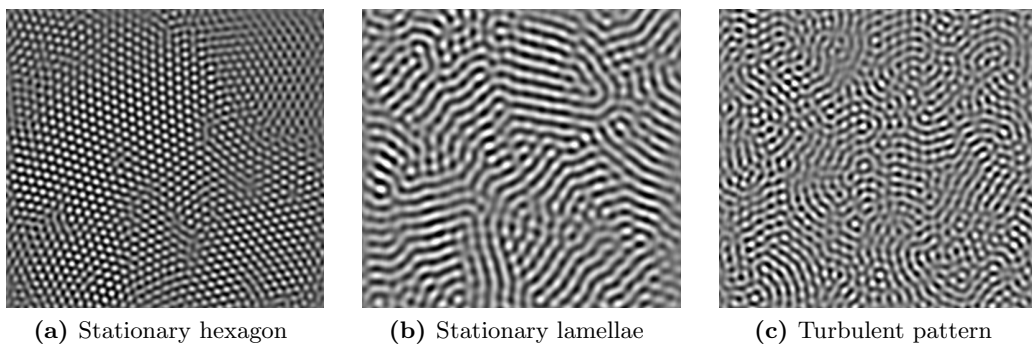


Figure 2.3: Turing Patterns found by Ouyang and Swinney. Stationary hexagonal and lamellar patterns, as well as turbulent patterns are reported in Ref. [47]. The concentration of the reactants in the compartments is given in Fig. 5.7. The region shown in the images is about 36 mm^2 .

2.2 Lengyel-Epstein (LE) model for the CIMA reaction

The Lengyel-Epstein (LE) model is based on the stoichiometric reaction equations that are believed to describe the CIMA reaction. The region of Turing pattern formation in the parameter space of the LE model can be derived using linear stability analysis.

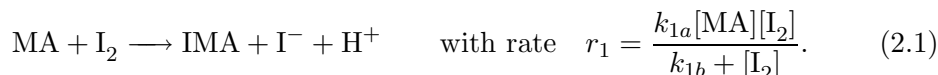
2.2.1 Derivation of the reaction-diffusion equations

A theoretical model for the chemical mechanism behind the CIMA reaction was proposed by Lengyel and Epstein in 1992 [27]. A brief overview of the model that covers all the important aspects is given in Ref. [54], while a detailed description is given in Ref. [28].

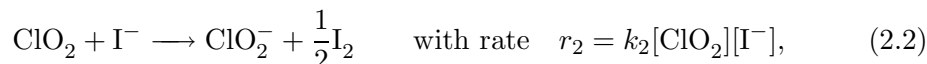
Lengyel and Epstein identified the key reactants in the system and the crucial role of the starch indicator as a complexing agent, i.e. it weakly binds iodide and iodine to slow down the effective diffusion rates, see also Ref. [1]. An underlying reaction in the CIMA experiment, the chlorine-dioxide-iodine-malonic acid (CDIMA) reaction is responsible for the pattern formation.

In the CIMA reaction chlordioxide and iodine are produced as intermediates with near constant concentration and the process is again described by the CDIMA reaction. Consequently both reactions are mathematically equivalent.

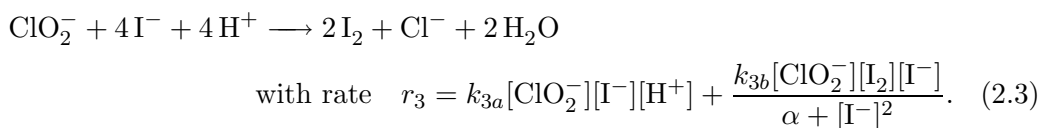
The reaction is described by three stoichiometric¹ equations of the five independent chemical ingredients MA, I₂, ClO₂, ClO₂⁻ and I⁻ as shown in Ref. [30] and Ref. [29]. The first is the reaction of malonic acid (MA) and iodine (I₂):



The second is a reaction between chlorine dioxide (ClO₂) and iodide (I⁻):



and the third component reaction between chlorite (ClO₂⁻) and iodide (I⁻) is

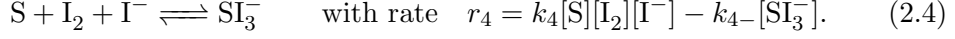


Cl⁻ and IMA are inert products of the process, while the concentration [H⁺] is treated as constant. Concentrations of any reactant are written with square brackets []. A reversible complexation² of iodine and iodide results in a slower effective diffusion rate for the activator iodide, as the starch-triiodide complex is immobile

¹An introduction to stoichiometry is found in Ref. [65]

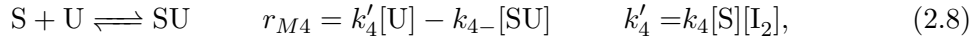
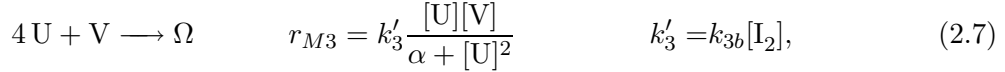
²The formation of chemical complexes, see Ref. [65].

in the gel. This mechanism results in a fourth reaction equation that has to be considered:



where $[S]$ represents the concentration of complexing sites, e.g. the concentration of starch in the gel. The effective rate laws for r_1 and r_3 account for complicated autocatalytic intermediate steps in the full reaction mechanism [9, 22, 29].

Eq. (2.1-2.3) together with Eq. (2.4) yields a seven component reaction-diffusion system. However for a wide range of experimental conditions $[ClO_2^-]$ and $[I^-]$ change rapidly by several orders of magnitude, while $[ClO_2]$, $[I_2]$ and $[MA]$ vary much more slowly [26]. Treating the slowly varying concentrations as constant and assuming that the concentration of starch is large and uniformly distributed in the gel, the model can be reduced to a two variable reaction-diffusion system, referred to as the Lengyel-Epstein (LE) model:



with $U = I^-$ and $V = ClO_2^-$. Symbolically α denotes the constant reactants and Ω the inert products. SU is the chemical complex formed by starch and iodide. The concentrations $[S]$ and $[A]$ are constant and $[SU]$ is assumed to be a linear function of $[U]$ for large concentrations of S . In the rate equation for r_{M3} the k_{3a} term from Eq. (2.3) has been neglected [29]. The resulting reaction diffusion equations are

$$\frac{\partial[U]}{\partial t} = k'_1 - k'_2[U] - k'_4[SU] - 4k'_3 \frac{[U][V]}{\alpha + [U]^2} + D_U \nabla^2[U], \quad (2.9)$$

$$\frac{\partial[V]}{\partial t} = k'_2[U] - k'_3 \frac{[U][V]}{\alpha + [U]^2} + D_V \nabla^2[V], \quad (2.10)$$

$$\frac{\partial[SU]}{\partial t} = k'_4[U] - k_{4-}[SU]. \quad (2.11)$$

Adding Eq. (2.9) and Eq. (2.11) and using that for large concentrations of the complexing agent S ,

$$[SU] = \frac{k'_4}{k_{4-}}[U] = K'[U] \quad \text{with} \quad K' = \frac{k_4}{k_{4-}}[S][I_2],$$

i.e. $[SU]$ is proportional to $[U]$, one obtains

$$(1 + K') \frac{\partial[U]}{\partial t} = k'_1 - k'_2[U] - 4k'_3 \frac{[U][V]}{\alpha + [U]^2} + D_U \nabla^2[U]. \quad (2.12)$$

After rescaling the differential equations become

$$\frac{\partial u}{\partial t'} = \nabla_{r'}^2 u + a - u - 4 \frac{uv}{1+u^2} = \nabla_{r'}^2 u + f(u, v), \quad (2.13)$$

$$\frac{\partial v}{\partial t'} = \sigma \left[c \nabla_{r'}^2 v + b \left(u - \frac{uv}{1+u^2} \right) \right] = \sigma c \nabla_{r'}^2 v + g(u, v), \quad (2.14)$$

with

$$\begin{aligned} u &= \frac{[U]}{\sqrt{\alpha}}, & v &= \frac{k'_3}{\alpha k'_2} [V], & c &= D_V/D_U, \\ a &= \frac{k'_1}{\sqrt{\alpha} k'_2}, & b &= \frac{k'_3}{\sqrt{\alpha} k'_2}, & \mathbf{r}' &= \sqrt{k'_2/D_U} \mathbf{r}, \\ t' &= \frac{k'_2}{\sigma} t, & \sigma &= (1 + K'). \end{aligned}$$

In this thesis Eq. (2.13) and Eq. (2.14) will be referred to as LE model. For convenience the rescaled time and space variables t' and \mathbf{r}' will be written as t and \mathbf{r} again.

The LE model also shows an interesting difference to phenomenological reaction diffusion models such as the Brusselator, described in section 2.3. Two-component reaction-diffusion systems are generally understood as activator-inhibitor models, with a local activation and a long range inhibition [44]. However the LE model is slightly counterintuitive, as u is always self-inhibitory, i.e. it always suppresses its own production. However around the homogeneous steady state u happens to be less self-inhibitory, when more of it is produced, i.e. the derivative with respect to u is positive in the region of Turing pattern formation, as shown in section 2.2.2. Consequently u can be considered as the activator in the system and v as the inhibitor, as it inhibits its own production and the production of u .

In the Brusselator model the patterns for activator and inhibitor are in opposite phase. However due to the general self-inhibition of the activator in the LE model the patterns for u and v are in phase, as shown in section 4.1.

2.2.2 Linear Stability Analysis

Pattern formation in reaction-diffusion systems is always associated with an instability of the homogeneous steady state. Consider a two-component system with at least one homogeneous steady state, i.e. the roots u_0 and v_0 of the reaction terms. This state will always be a solution of the system, however, it is not always stable, i.e. when the system is in a perturbed state it does not converge to the homogeneous steady state, depending on the parameters.

There are two different transitions in the parameter space. The first is called a *Hopf bifurcation* and marks the transition from a region with a stable homogeneous steady state to a region where it is unstable, when the diffusion constants are set to zero. In the unstable regime any system which is not exactly in the homogeneous

steady state will either diverge or converge to a periodic solution³. The second is called a Turing bifurcation, which marks the transition from a region with a stable homogeneous steady state to a region, where the homogeneous state is unstable, when taking diffusion into account. In the unstable regime spatially heterogeneous steady states, i.e. Turing patterns can be stable solutions, i.e. a system which is not exactly in the homogeneous state but spatially perturbed will converge into a Turing state. As diffusion is the source of the second instability it is also called diffusion-driven instability.

The transitions in the parameter space, i.e. the region where the system exhibits diffusion-driven instability, can be found by linear stability analysis. Therefore the system is linearized by expanding the reaction terms around the homogeneous steady state and the time-evolution of single Fourier modes is analyzed with and without diffusion. The homogeneous steady state of the LE model can be derived from the reaction terms in Eq. (2.13) and Eq. (2.14):

$$g(u, v) = \sigma b \left(u - \frac{v u}{1 + u^2} \right), \quad (2.15)$$

$$f(u, v) = a - u - 4 \frac{v u}{1 + u^2}. \quad (2.16)$$

The homogeneous steady state is given by

$$g(u_0, v_0) = 0 \quad \text{and} \quad f(u_0, v_0) = 0. \quad (2.17)$$

Solving Eqs. (2.17) for u_0 and v_0 yields

$$v_0 = 1 + \alpha^2 = 1 + \frac{a^2}{25} \quad \text{and} \quad u_0 = \alpha = \frac{a}{5}. \quad (2.18)$$

Then Eq. (2.13) and Eq. (2.14) are linearized around the homogeneous steady state and diffusion is neglected. The linearized equations can be solved by an exponential ansatz and the transition from convergence to divergence, i.e. the Hopf bifurcation, can be obtained from the transition from negative to positive real part of the exponent.

To find the transition from a linearly stable to an linearly unstable state in presence of diffusion a similar analysis has to be done, taking diffusion into account. Solving the linearized reaction-diffusion system equations in Fourier Space yields the dispersion relation and the transition from only modes with negative real part of the exponent to some modes with positive real part of the exponent gives the Turing bifurcation.

Both Hopf and Turing bifurcation will depend on the linearized reaction terms but only the Turing bifurcation depends on the diffusion coefficients. For a general reaction-diffusion system with reaction terms f and g and ratio of diffusion coefficients d the following conditions have to be fulfilled for Turing Pattern formation.

³See Poincaré-Bendixson theorem in Ref. [59].

A full derivation is given in Ref. [44]:

$$f_u + g_v < 0, \quad (2.19)$$

$$f_u g_v - f_v g_u > 0, \quad (2.20)$$

$$d f_u + g_v > 0, \quad (2.21)$$

$$(d f_u + g_v)^2 - 4 d (f_u g_v - f_v g_u) > 0. \quad (2.22)$$

Eqs. (2.19) - 2.20) give the Hopf bifurcation while Eqs. (2.21) - 2.22) give the Turing bifurcation. For the LE model the linearized reaction terms are given by

$$f_u = \left. \frac{\partial f}{\partial u} \right|_{u_0, v_0} = \frac{3\alpha^2 - 5}{1 + \alpha^2}, \quad f_v = \left. \frac{\partial f}{\partial v} \right|_{u_0, v_0} = -4 \frac{\alpha}{1 + \alpha^2}, \quad (2.23)$$

$$g_u = \left. \frac{\partial g}{\partial u} \right|_{u_0, v_0} = \sigma b \frac{2\alpha^2}{1 + \alpha^2}, \quad g_v = \left. \frac{\partial g}{\partial v} \right|_{u_0, v_0} = -\sigma b \frac{\alpha}{1 + \alpha^2} \quad (2.24)$$

and $d = \sigma c$. Inserting Eqs. (2.23 - 2.24) into Eqs. (2.19 - 2.22) yields the conditions

$$\sigma b \alpha > 3\alpha^2 - 5, \quad (2.25)$$

$$\frac{\sigma b \alpha}{1 + \alpha^2} > 0, \quad (2.26)$$

$$\sigma b \alpha < (3\alpha^2 - 5) d, \quad (2.27)$$

$$9d^2\alpha^4 - 30d^2\alpha^2 - 26d\alpha^3\sigma b + 25d^2 - 10d\sigma b\alpha + \sigma^2 b^2\alpha^2 > 0. \quad (2.28)$$

Assuming that $\sigma, d, \alpha > 0$ and considering Eq. (2.27), Eq. (2.28) yields for the Turing bifurcation

$$b_T = \frac{c}{5a} \left(13a^2 + 125 - 4\sqrt{10a}\sqrt{a^2 + 25} \right) \quad (2.29)$$

Additionally Eq. (2.25) yields for the Hopf bifurcation

$$b_H = \frac{1}{\sigma} \left(\frac{3}{5} a - \frac{25}{a} \right), \quad (2.30)$$

and the region of Turing instability is given by

$$b_H < b < b_T, \quad (2.31)$$

i.e. the region of the parameter space, where the homogeneous steady state is stable without diffusion but unstable, when diffusion is taken into account. The curves b_H and b_T are shown in section 4.1 for parameters that resemble the experimental conditions. Additionally in regions where the homogeneous steady state is unstable with and without diffusion the convergence to heterogeneous steady states is often favorable. Only in regions, where $b_H > b > b_T$ and when $b_T \approx b_H$, oscillatory and spatio-temporal solutions can occur.

Linear stability analysis distinguishes convergent from divergent modes, however only the modes with a real part of the exponent, which is exactly zero will give a linearly stable standing wave pattern. However the full nonlinear reaction terms expand the number of stable modes and bound the divergent modes, so that complex heterogeneous patterns can form in the system from randomly disturbed initial conditions.

2.3 Other reaction-diffusion models

Apart from the LE model which is based on the chemical mechanism of the CIMA reaction, phenomenological models with simple reaction kinetics for pattern formation in reaction-diffusion systems have been suggested. A well-established model, proposed in Ref. [16] is the so-called Brusselator, which is motivated by simple but unphysical chemical reaction equations with two diffusing and reacting intermediates u and v . The corresponding reaction-diffusion system is given by

$$\frac{\partial u}{\partial t} = D_u \nabla^2 u + a - (b + 1)u + u^2 v, \quad (2.32)$$

$$\frac{\partial v}{\partial t} = D_v \nabla^2 v + bu - u^2 v, \quad (2.33)$$

with constants D_u , D_v , a and b . A detailed analysis of pattern formation in the Brusselator model can be found in Ref. [48].

A generic approach to a reaction-diffusion system leads to the model proposed and analyzed in Ref. [6], referred to as the generic Brusselator, where general nonlinear reaction terms are expanded around a steady state up to third order and the coefficients are conveniently chosen to keep the model simple, but generate a diversity of patterns. The specific form of the system is:

$$\frac{\partial u}{\partial t} = D\delta \nabla^2 u + \alpha u(1 - r_1 v^2) + v(1 - r_2 u), \quad (2.34)$$

$$\frac{\partial v}{\partial t} = \delta \nabla^2 v + v(\beta + \alpha r_1 u v) + u(\gamma + r_2 v), \quad (2.35)$$

with constants D , δ , α , β , r_1 and r_2 . The generic Brusselator model has also been used to study the effect of noise on Turing pattern formation [31]. Other reaction-diffusion systems with pattern formation are the Schnakenberg [57], Gierer-Meinhardt [15], Gray-Scott [49], Thomas [60] and Bazykin model⁴ [36], which all have similar phenomenological reaction terms.

While the kinetics of these models are greatly simplified we show in chapter 5 that the concentration profiles of similar states are morphologically similar. This indicates that the difference between experimental and simulated patterns, shown in chapter 5 is not due to the specific form of the reaction kinetics, but appears to be a more generic property of deterministic reaction-diffusion Turing models.

⁴The Bazykin model is a modified Lotka-Volterra predator-prey system [64].

Chapter 3

Numerical solution of 2D reaction-diffusion equations

Two-component reaction-diffusion systems can be solved numerically using a finite-difference discretization. An explicit scheme and a semi-implicit Crank-Nicolson scheme based on the methods described in Ref. [50] are described in this chapter. Both schemes are stable for suitable grid resolutions Δ and Δt , which can be shown by a von Neumann stability analysis. Additionally the schemes can be extended to reaction-diffusion equations with additive noise terms, i.e. stochastic partial differential equations [18].

3.1 Explicit finite difference scheme

A general two-component reaction-diffusion system is given by

$$\frac{\partial u}{\partial t} = D_u \nabla^2 u + f(u, v), \quad (3.1)$$

$$\frac{\partial v}{\partial t} = D_v \nabla^2 v + g(u, v), \quad (3.2)$$

for functions $u(x, y, t)$ and $v(x, y, t)$ that represent the concentrations of substances U and V . We discretize time and spatial coordinates with

$$t_n = n \Delta t \quad x_i = i \Delta x \quad y_j = j \Delta y, \quad (3.3)$$

as illustrated in Fig. 3.1. Eqs. (3.1 - 3.2) can be solved numerically using an explicit scheme, by discretizing the time-derivative with first-order accuracy:

$$\left. \frac{\partial u}{\partial t} \right|_{j,l} = \frac{u_{j,l}^{n+1} - u_{j,l}^n}{\Delta t} + O(\Delta t^2), \quad (3.4)$$

with $u_{j,l}^n = u(x_j, y_l, t_n)$, as described in Ref. [50]. The discretization of the second spatial derivative in two dimensions, where for convenience the spatial discretization is $\Delta x = \Delta y = \Delta$, is given by

$$\nabla^2 u = \frac{u_{j+1,l}^n + u_{j-1,l}^n + u_{j,l+1}^n + u_{j,l-1}^n - 4u_{j,l}^n}{\Delta^2} + O(\Delta^2). \quad (3.5)$$

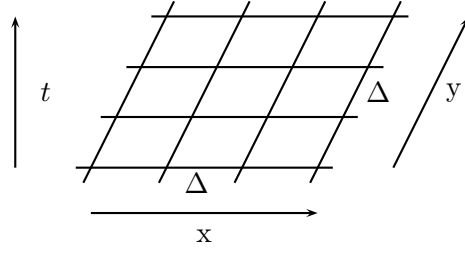


Figure 3.1: Distretized space grid with spatial discretization Δ . A finite-size grid with periodic boundary conditions is used in the numerical calucaltion.

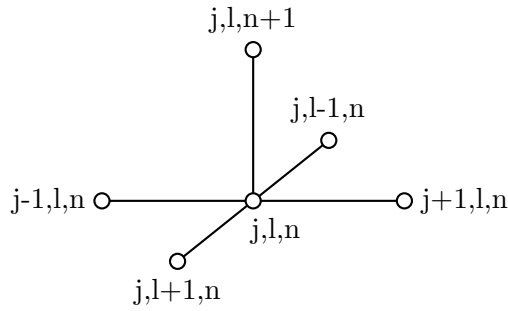


Figure 3.2: Graphical scheme of the Forward-Time-Space-Centered Euler method. The grid sites are depicted as circles connected by lines which indicate the dependence. Each site at time $n + 1$ depends explicitly on the corresponding site at time n and its nearest neighbors.

Therefore the time and spatial discretization of Eq. (3.1) is

$$u_{j,l}^{n+t} = u_{j,l}^n + \gamma_u (u_{j+1,l}^n + u_{j-1,l}^n + u_{j,l+1}^n + u_{j,l-1}^n - 4u_{j,l}^n) + \Delta t f(u_{j,l}^n, v_{j,l}^n) \quad (3.6)$$

and similarly for Eq. (3.2)

$$v_{j,l}^{n+t} = v_{j,l}^n + \gamma_v (v_{j+1,l}^n + v_{j-1,l}^n + v_{j,l+1}^n + v_{j,l-1}^n - 4v_{j,l}^n) + \Delta t g(u_{j,l}^n, v_{j,l}^n) \quad (3.7)$$

with

$$\gamma_u = \frac{D_u \Delta t}{\Delta^2} \quad \text{and} \quad \gamma_v = \frac{D_v \Delta t}{\Delta^2}. \quad (3.8)$$

Eq. (3.6) and Eq. (3.7) can be solved explicitly via forward integration, i.e. calculating the concentration at time-step $n + 1$ from the concentration profile at time-step n , with initial conditions u^0 and v^0 . This type of finite difference scheme is called a Forward-Time-Centered-Space (FTCS) method. A graphical representation of the scheme is shown in Fig. 3.1. Each site (j, l) in the grid at time $n + 1$ depends explicitly on the same site at time n and its four nearest neighbors.

The advantage of the FTCS method is that it is easy to implement. The method is conditionally stable for values of Δt and Δ given by Eq. (3.31), which is obtained by a von Neumann stability analysis in section 3.3.

However the FTCS schemes generally converge more slowly than implicit methods. Therefore a semi-implicit Crank-Nicolson scheme is discussed in the following section.

However due to the system-size dependence of the semi-implicit scheme the FTCS method has been used for the generation of most patterns in this thesis.

3.2 Semi-implicit Crank-Nicolson scheme

For a two-dimensional diffusion equation a FTCS scheme might not be the right choice, as shown in Ref. [50], as a large number of small time-steps has to be calculated to evolve up to a timescale of physical interest. The implicit Crank-Nicolson method gives an unconditionally stable solver for this special case. A scheme is called explicit if the solution for the time-step $n + 1$ is given as an explicit function of the solution at time n , and implicit if it requires the solution of a system of linear equations for each time-step. A semi-implicit scheme for a general reaction-diffusion system, as given by Eq. (3.1) and Eq. (3.2) can be obtained similarly by discretizing the spatial derivative as an average of forward and backward Euler in time:

$$\nabla^2 u = \frac{1}{2} \left(\frac{u_{j+1,l}^n + u_{j-1,l}^n + u_{j,l+1}^n + u_{j,l-1}^n - 4u_{j,l}^n}{(\Delta)^2} + \frac{u_{j+1,l}^{n+1} + u_{j-1,l}^{n+1} + u_{j,l+1}^{n+1} + u_{j,l-1}^{n+1} - 4u_{j,l}^{n+1}}{(\Delta)^2} \right) + O(\Delta^4). \quad (3.9)$$

For the time derivative the same first order discretization is used as for the FTCS scheme:

$$\left. \frac{\partial u}{\partial t} \right|_{j,l} = \frac{u_{j,l}^{n+1} - u_{j,l}^n}{\Delta t} + O(\Delta t^2). \quad (3.10)$$

Using Eq. (3.9) and Eq. (3.10) to discretize the reaction-diffusion system described by Eq. (3.1) and Eq. (3.2) and separating the $\{u, v\}^n$ and $\{u, v\}^{n+1}$ terms yields

$$\begin{aligned} (1 + 2\gamma_u) u_{j,l}^{n+1} - \frac{\gamma_u}{2} (u_{j+1,l}^{n+1} + u_{j-1,l}^{n+1} + u_{j,l+1}^{n+1} + u_{j,l-1}^{n+1}) = \\ (1 - 2\gamma_u) u_{j,l}^n + \frac{\gamma_u}{2} (u_{j+1,l}^n + u_{j-1,l}^n + u_{j,l+1}^n + u_{j,l-1}^n) + \Delta t f(u_{j,l}^n, v_{j,l}^n), \end{aligned} \quad (3.11)$$

and

$$\begin{aligned} (1 + 2\gamma_v) v_{j,l}^{n+1} - \frac{\gamma_v}{2} (v_{j+1,l}^{n+1} + v_{j-1,l}^{n+1} + v_{j,l+1}^{n+1} + v_{j,l-1}^{n+1}) = \\ (1 - 2\gamma_v) v_{j,l}^n + \frac{\gamma_v}{2} (v_{j+1,l}^n + v_{j-1,l}^n + v_{j,l+1}^n + v_{j,l-1}^n) + \Delta t g(u_{j,l}^n, v_{j,l}^n), \end{aligned} \quad (3.12)$$

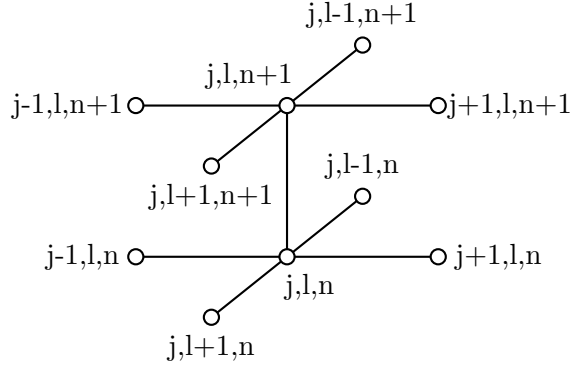


Figure 3.3: Graphical scheme of the semi-implicit Crank-Nicolson method. The grid sites are depicted as circles connected by lines which indicate the dependence. Each site at time $n + 1$ depends implicitly on its nearest neighbors and the corresponding sites at time n .

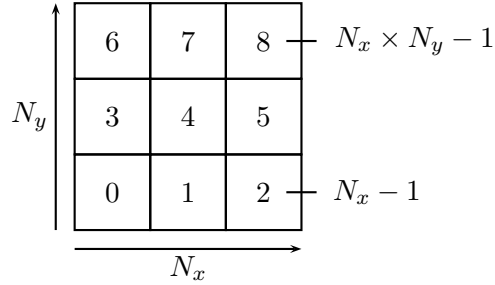


Figure 3.4: The fields u and v can be written as a vector by appending all consecutive rows up to N_y . Eq. (3.12) and Eq. (3.11) can then be written as simple matrix equations.

with

$$\gamma_u = \frac{D_u \Delta t}{\Delta^2} \quad \text{and} \quad \gamma_v = \frac{D_v \Delta t}{\Delta^2}. \quad (3.13)$$

This results in a semi-implicit scheme, as the spatial derivative is treated implicitly, while the reaction terms are treated explicitly. The scheme can be visualized graphically as shown in Fig. 3.2. Each site (j, l) at time-step $n + 1$ depends explicitly on its four nearest neighbors as well as the same site (j, l) at time n and its four nearest neighbors, which results in an implicit dependence on all sites in the grid. Consequently a system of $N_x \times N_y$ linear equations has to be solved at each time-step.

Writing the fields u and v as a vector beginning with the first row and appending each following row up to N_y as illustrated in Fig. 3.4, the coefficients on the left side of Eq. (3.11) and Eq. (3.12) can be written as a matrix with constant entries. Eq. (3.11) and Eq. (3.12) can then be written as a matrix equation, as given by Eq. (3.14) and Eq. (3.15), where $A_{u,v}$ is a block diagonal matrix of size $N \times N$ with system size $N = N_x \times N_y$:

$$\mathbf{A}_u \cdot u^{n+1} = b_u^n(u, v) \quad (3.14)$$

and

$$\mathbf{A}_v \cdot v^{n+1} = b_v^n(u, v). \quad (3.15)$$

\mathbf{A}_u depends only on γ_u and \mathbf{A}_v on γ_v . For periodic boundary conditions \mathbf{A}_u and \mathbf{A}_v can be expressed using

$$\alpha_u = 1 + 2\gamma_u \quad \text{and} \quad \alpha_v = 1 + 2\gamma_v, \quad (3.16)$$

such that

$$\mathbf{A}_u = \begin{pmatrix} \mathbf{a}_u & \mathbf{b}_u & & & \mathbf{b}_u \\ \mathbf{b}_u & \mathbf{a}_u & \mathbf{b}_u & & \\ & \ddots & \ddots & \ddots & \\ & & \mathbf{b}_u & \mathbf{a}_u & \mathbf{b}_u \\ \mathbf{b}_u & & & \mathbf{b}_u & \mathbf{a}_u \end{pmatrix}. \quad (3.17)$$

with

$$\mathbf{a}_u = \begin{pmatrix} \alpha_u & -\frac{\gamma_u}{2} & & & -\frac{\gamma_u}{2} \\ -\frac{\gamma_u}{2} & \alpha_u & -\frac{\gamma_u}{2} & & \\ & \ddots & \ddots & \ddots & \\ & & -\frac{\gamma_u}{2} & \alpha_u & -\frac{\gamma_u}{2} \\ -\frac{\gamma_u}{2} & & & -\frac{\gamma_u}{2} & \alpha_u \end{pmatrix} \quad (3.18)$$

and

$$\mathbf{b}_u = \begin{pmatrix} -\frac{\gamma_u}{2} & & & & \\ & -\frac{\gamma_u}{2} & & & \\ & & \ddots & & \\ & & & -\frac{\gamma_u}{2} & \\ & & & & -\frac{\gamma_u}{2} \end{pmatrix} \quad (3.19)$$

and similar for \mathbf{A}_v . Eq. (3.14) and Eq. (3.15) were solved numerically using a general LU-decomposition routine from Numerical Recipes [50]. \mathbf{A} is a sparse, symmetric and band-diagonal matrix with only five non-zero entries in each row and column, which correspond to each site and its four nearest neighbors. Taking these conditions into account a faster algorithm than a general LU-decomposition should be used, however the lower left and upper right block in \mathbf{A} make it difficult to implement standard sparse matrix algorithms.

3.3 Von Neumann stability analysis

The von Neumann stability analysis is a local analysis, which gives a condition for the numerical stability of any finite-difference scheme for partial differential equations. It should not be confused with the linear stability analysis in section 2.2.2 to determine parameter values for pattern formation. Nonlinear terms have to be linearized about a given solution and for coupled reaction terms the von Neumann analysis has to be applied in its vector form [50].

3.3.1 Explicit finite difference scheme

For a von Neumann stability analysis the reaction equations have to be linearized. Therefore we write the actual solution of the reaction diffusion system as

$$u = u_0 + \delta u \quad \text{and} \quad v = v_0 + \delta v, \quad (3.20)$$

where u_0 and v_0 is the homogeneous steady state and δu and δv are fluctuations not too far away from it. Therefore the nonlinear reaction terms can be expanded up to first order in δu and δv . As u_0 and v_0 solve Eq. (3.6) and Eq. (3.7) exactly the linearized difference equations for δu δv remains:

$$\begin{aligned} \delta u_{j,l}^{n+1} = & \delta u_{j,l}^n + \gamma_u (\delta u_{j+1,l}^n + \delta u_{j-1,l}^n + \delta u_{j,l+1}^n + \\ & \delta u_{j,l-1}^n - 4\delta u_{j,l}^n) + \Delta t f_u \delta u_{j,l}^n + \Delta t f_v \delta v_{j,l}^n, \end{aligned} \quad (3.21)$$

$$\begin{aligned} \delta v_{j,l}^{n+1} = & \delta v_{j,l}^n + \gamma_v (\delta v_{j+1,l}^n + \delta v_{j-1,l}^n + \delta v_{j,l+1}^n + \\ & \delta v_{j,l-1}^n - 4\delta v_{j,l}^n) + \Delta t g_u \delta u_{j,l}^n + \Delta t g_v \delta v_{j,l}^n \end{aligned} \quad (3.22)$$

with

$$\begin{aligned} f_u &= \left. \frac{\partial f}{\partial u} \right|_{u_0, v_0}, & g_u &= \left. \frac{\partial g}{\partial u} \right|_{u_0, v_0}, \\ f_v &= \left. \frac{\partial f}{\partial v} \right|_{u_0, v_0}, & g_v &= \left. \frac{\partial g}{\partial v} \right|_{u_0, v_0}. \end{aligned} \quad (3.23)$$

For a system of coupled linear partial differential equations (PDEs) the von Neumann analysis yields

$$\begin{pmatrix} \delta u^n \\ \delta v^n \end{pmatrix} = \xi^n e^{ik_x j \Delta} e^{ik_y l \Delta} \cdot \begin{pmatrix} \delta u_0 \\ \delta v_0 \end{pmatrix}. \quad (3.24)$$

Inserting this into Eq. (3.21) and Eq. (3.22) and dividing by ξ and $e^{ik_x j \Delta + ik_y l \Delta}$ gives

$$\begin{aligned} (\xi - 1 + 2\chi_u - \Delta t f_u) \delta u_0 - \Delta t f_v \delta v_0 &= 0, \\ (\xi - 1 + 2\chi_v - \Delta t g_v) \delta u_0 - \Delta t g_u \delta v_0 &= 0 \end{aligned} \quad (3.25)$$

with

$$\chi_u = 2\gamma_u \sin^2 \frac{k_x \Delta}{2} + 2\gamma_u \sin^2 \frac{k_y \Delta}{2} \quad (3.26)$$

and

$$\chi_v = 2\gamma_v \sin^2 \frac{k_x \Delta}{2} + 2\gamma_v \sin^2 \frac{k_y \Delta}{2}. \quad (3.27)$$

Eq. (3.25) can be written as a matrix equation:

$$\begin{pmatrix} \xi - \alpha_u & -\Delta t f_v \\ -\Delta t g_u & \xi - \alpha_v \end{pmatrix} \cdot \begin{pmatrix} \delta u_0 \\ \delta v_0 \end{pmatrix} = 0 \quad (3.28)$$

with

$$\alpha_u = 1 - 2\chi_u + \Delta t f_u \quad \text{and} \quad \alpha_v = 1 - 2\chi_v + \Delta t g_v, \quad (3.29)$$

which has nontrivial solutions only if the determinant is zero, i.e.

$$(\xi - \alpha_u)(\xi - \alpha_v) - (\Delta t)^2 f_v g_u = 0. \quad (3.30)$$

So the condition $|\xi| < 1$ has to be fulfilled for the solutions

$$\xi_{\pm} = \frac{1}{2} \left[(\alpha_u + \alpha_v) \pm \sqrt{(\alpha_u + \alpha_v)^2 + 4(\Delta t)^2 f_v g_u} \right]. \quad (3.31)$$

Obviously the stability depends on Δt , Δ and the linearized reaction terms f_u, f_v and g_u, g_v . Consequently the time and spatial discretization have to be adjusted for the considered part of the parameter space, when a system is solved numerically. For the numerical solutions in chapter 4 the fixed discretization parameters where $\Delta = 1$ or $\Delta = 0.5$ with $\Delta t = 0.01$ or $\Delta t = 0.001$ respectively. This ensures $|\xi_{\pm}| < 1$ for the analyzed parameter space.

3.3.2 Semi-implicit Crank-Nicolson scheme

We linearize the difference equation Eq. (3.11) and Eq. (3.12) about the homogeneous steady state using Eq. (3.20) to obtain a linearized difference equation for δu

$$\begin{aligned} & (1 + 2\gamma_u) \delta u_{j,l}^{n+1} - \frac{\gamma_u}{2} \left(\delta u_j^{n+1}, l + \delta u_{j-1,l}^{n+1} + \delta u_{j,l+1}^{n+1} + \delta u_{j,l-1}^{n+1} \right) \\ & = (1 - 2\gamma_u) \delta u_{j,l}^n + \frac{\gamma_u}{2} \left(\delta u_j^n, l + \delta u_{j-1,l}^n + \delta u_{j,l+1}^n + \delta u_{j,l-1}^n \right) + \Delta t \left(f_u \delta u_{j,l}^n + f_v \delta v_{j,l}^n \right) \end{aligned} \quad (3.32)$$

and similar for δv :

$$\begin{aligned} & (1 + 2\gamma_v) \delta v_{j,l}^{n+1} - \frac{\gamma_v}{2} \left(\delta v_j^{n+1}, l + \delta v_{j-1,l}^{n+1} + \delta v_{j,l+1}^{n+1} + \delta v_{j,l-1}^{n+1} \right) \\ & = (1 - 2\gamma_v) \delta v_{j,l}^n + \frac{\gamma_v}{2} \left(\delta v_j^n, l + \delta v_{j-1,l}^n + \delta v_{j,l+1}^n + \delta v_{j,l-1}^n \right) + \Delta t \left(g_v \delta v_{j,l}^n + g_u \delta u_{j,l}^n \right). \end{aligned} \quad (3.33)$$

The ansatz from Eq. (3.24) yields

$$\left[\xi - \frac{1 - \chi_u}{1 + \chi_u} - \Delta t \frac{f_u}{1 + \chi_u} \right] \delta u_0 - \Delta t \frac{f_v}{1 + \chi_u} \delta v_0 = 0 \quad (3.34)$$

and

$$\left[\xi - \frac{1 - \chi_v}{1 + \chi_v} - \Delta t \frac{g_v}{1 + \chi_v} \right] \delta v_0 - \Delta t \frac{g_u}{1 + \chi_v} \delta u_0 = 0 \quad (3.35)$$

with

$$\chi_u = 2\gamma_u \sin^2 \frac{k_x \Delta}{2} + 2\gamma_u \sin^2 \frac{k_y \Delta}{2} \quad (3.36)$$

and

$$\chi_v = 2\gamma_v \sin^2 \frac{k_x \Delta}{2} + 2\gamma_v \sin^2 \frac{k_y \Delta}{2}, \quad (3.37)$$

or as a matrix equation

$$\begin{pmatrix} \xi - \beta_u & -\Delta t \frac{f_v}{1 + \chi_u} \\ -\Delta t \frac{g_u}{1 + \chi_v} & \xi - \beta_v \end{pmatrix} \cdot \begin{pmatrix} \delta u_0 \\ \delta v_0 \end{pmatrix} = 0 \quad (3.38)$$

with

$$\beta_u = \frac{1 - \chi_u}{1 + \chi_u} + \Delta t \frac{f_u}{1 + \chi_u} \quad \text{and} \quad \beta_v = \frac{1 - \chi_v}{1 + \chi_v} + \Delta t \frac{g_v}{1 + \chi_v}. \quad (3.39)$$

Eq. (3.38) can only have nontrivial solutions if the determinant is zero. Consequently we get

$$(\xi - \beta_u)(\xi - \beta_v) - (\Delta t)^2 f_v g_u = 0. \quad (3.40)$$

So the condition $|\xi| < 1$ has to be fulfilled for the solutions

$$\xi_{\pm} = \frac{1}{2} \left[(\beta_u + \beta_v) \pm \sqrt{(\beta_u + \beta_v)^2 + 4(\Delta t)^2 f_v g_u} \right]. \quad (3.41)$$

The stability depends on the time and spatial discretization Δt , Δ and the values of the linearized reaction terms f_u, f_v and g_u, g_v . However as $1 + \chi_u$ and $1 + \chi_v$ are always larger than one the stability is less dependent on Δ for a suitable set of parameters than it is for the FTCS method. Common parameters used for the semi-implicit method were $\Delta = 1$ and $\Delta t = 0.1$, which ensures $|\xi_{\pm}| < 1$.

3.4 Convergence to stationary patterns

The numerical convergence of the stationary solutions in the Turing regime depends on the scheme used for the calculation and on the parameters used in the nonlinear reaction terms. For the explicit FTCS algorithm, solving the LE model, this is illustrated in Fig. 3.5, where the absolute change of concentrations summed over all points in the grid relative to the size $N^2 = 200^2$ after 1000 time-steps is shown, given by

$$\Delta u_i = \sum_{j,l} \left| u_{j,l}^{n_i} - u_{j,l}^{n_i-1} \right| \quad \text{with} \quad n_i = i \cdot 1000. \quad (3.42)$$

The inverted hexagonal and lamellar states converge after about 20,000 time-steps, as shown in Fig. 3.5a and Fig. 3.5b, while the hexagonal state has to overcome a metastable transient state and converges after about 50,000 time-steps, see Fig. 3.5c. However the required time-steps for convergence can depend on the chosen parameters and the values given here can only be considered as a rough estimate.

A similar analysis for the semi-implicit Crank-Nicolson method is shown in Fig. 3.6 for a system of size $N^2 = 50^2$. Apart from transient metastable states that appear more dominant for smaller systems no qualitative difference in the time evolution can be observed. Depending on the parameters a larger time-step of approximately one order of magnitude compared to the FTCS method is possible, when using the semi-implicit method. However the semi-implicit method in its current implementation (i.e. with LE decomposition to solve the linear equation system) has a computing time proportional to N^6 , where N is the linear system size. In this implementation the larger computing time makes the semi-implicit Crank Nicolson method slower than the explicit FTCS method, despite the larger time-step for the semi-implicit method. Therefore the explicit scheme has been used for the numerical analysis of the LE model in this thesis.

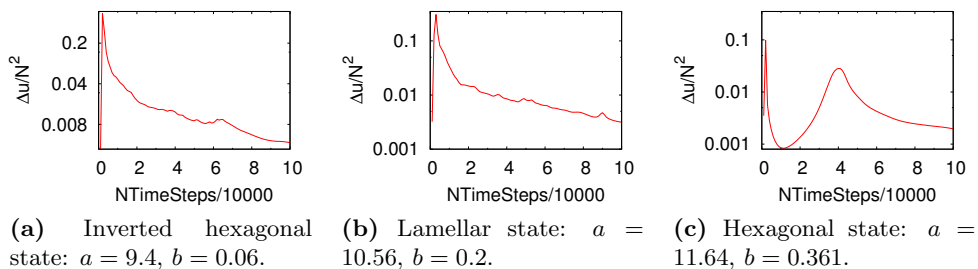


Figure 3.5: The absolute change of concentrations after 1000 time-steps summed over all grid-points in a mesh with $N = 200$ and $\Delta t = 0.01$. Inverted hexagonal and lamellar state converge after about 20,000 time-steps, while the hexagonal state has to overcome a transient state and converges after about 50,000 time-steps. Common parameters for all solutions are $\sigma = 20$ and $c = 1$.

To illustrate the time evolution of the numerical solution a series of hexagonal patterns with increasing time is shown in Fig. 3.7. A transient metastable state can be recognized at 10,000 – 40,000 time-steps, after which the system converges into its final state.

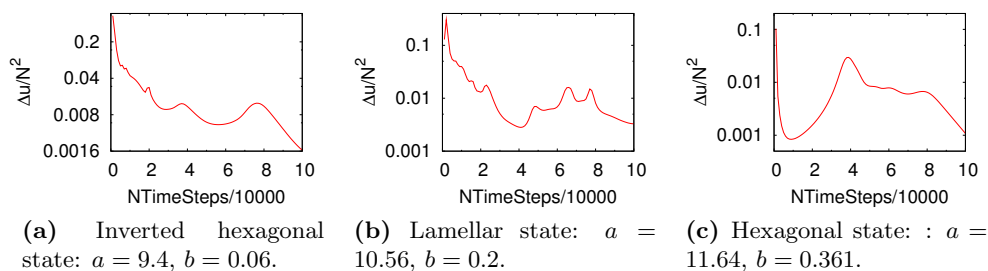


Figure 3.6: The absolute change of concentrations after 1000 time-steps summed over all grid-points in a mesh with $N = 50$ and $\Delta t = 0.01$. Inverted hexagonal and lamellar state converge early about 20,000 time-steps, while the hexagonal state has to overcome a transient state and converges after about 50,000 time-steps.

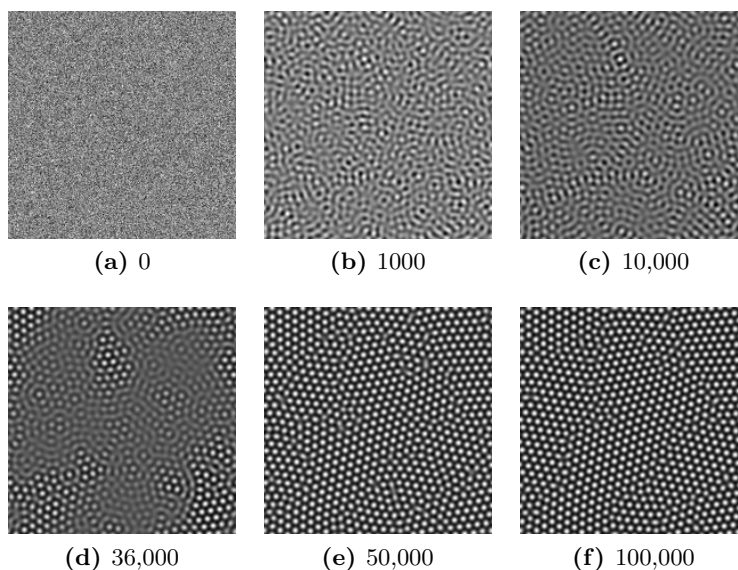


Figure 3.7: A series of patterns in the hexagonal state ($\sigma = 20$, $c = 1$, $a = 11.64$, $b = 0.361$) with increasing time. The number of elapsed time-steps is given below each pattern. The system overcomes a transient metastable state at 36,000 time-steps and reaches its final state after about 50,000 time-steps with $\Delta t = 0.01$.

3.5 Discretization of stochastic partial differential equations

The numerical solution of stochastic partial differential equations (SPDE) is an active field of research [18, 23]. Methods that work well for deterministic partial differential equations (DPDE) cannot be immediately applied to SPDEs.

We apply a simple finite-difference method, see Ref. [2], to the LE model with additive Gaussian white noise. The stochastic partial differential equations, corresponding to Eqs. (2.13 - 2.14), are

$$\frac{\partial u}{\partial t} = D_u \nabla^2 u + f(u, v) + \zeta_u \xi_u(\mathbf{r}, t), \quad (3.43)$$

$$\frac{\partial v}{\partial t} = D_v \nabla^2 v + g(u, v) + \zeta_v \xi_v(\mathbf{r}, t), \quad (3.44)$$

where ξ_u and ξ_v denote the Gaussian white noise with

$$\langle \xi_i \rangle = 0 \quad \langle \xi_i(\mathbf{r}, t) \xi_j(\mathbf{r}', t') \rangle = \delta_{ij} \delta(\mathbf{r} - \mathbf{r}') \delta(t - t'), \quad (3.45)$$

i.e. delta-correlated in time and space with zero mean and variance one. ζ_u and ζ_v are positive constants and give the intensity of the noise, i.e. the width of the distributions. The formulation of Eq. (3.44) bears some mathematical problems. Intuitively this adds random fluctuations to the production rates of u and v . However this would mean the concentrations become a stochastic process, which are almost certainly not differentiable. For Eq. (3.44) a mathematically rigorous meaning ξ has to be considered as a generalized derivative of a stochastic process, called Wiener process W , or as a physicist would call it, Brownian motion [18]. In two spatial dimensions ξ is written as

$$\xi(\mathbf{r}, t) = \frac{\partial W(\mathbf{r}, t)}{\partial x \partial y \partial t}. \quad (3.46)$$

W has independent increments so that

$$\int_{t^i}^{t^{i+1}} \int_{x^j}^{x^{j+1}} \int_{y^k}^{y^{k+1}} dW = \sqrt{dt} \sqrt{dx} \sqrt{dy} \eta_{ijk} \quad (3.47)$$

with

$$dt = t^{i+1} - t^i, \quad (3.48)$$

$$dx = x^{j+1} - x^j, \quad (3.49)$$

$$dy = y^{k+1} - y^k, \quad (3.50)$$

$$(3.51)$$

and

$$\eta_{ijk} \in N(0, 1) \forall i, j, k, \quad (3.52)$$

where $N(0,1)$ denotes the normal distribution with zero mean and variance one. As dt , dx and dy do not depend on i, j, k the indices of η are obsolete and merely indicate the independence of all three dimensions.

Using Eq. (3.47) the stochastic term can be discretized by random numbers drawn from a normal distribution. Intuitively we start with a finite-difference scheme for an ordinary partial differential equation and add random numbers, where the intensity of the noise is rescaled depending on Δt , Δx and Δy , at each site and each time-step. Eq. (3.46) can be discretized as

$$\frac{\partial W}{\partial t \partial x \partial y} \approx \frac{\Delta W_{j,l}^n}{\Delta t \Delta x \Delta y} = \frac{\sqrt{\Delta t} \sqrt{\Delta x} \sqrt{\Delta y} \eta_{j,l}^n}{\Delta t \Delta x \Delta y} = \frac{1}{\sqrt{\Delta t \Delta x \Delta y}} \eta_{j,l}^n, \quad (3.53)$$

where $\eta_{j,l}^n \in N(0,1)$ are normally distributed random numbers with zero mean and variance one. Consequently the semi-discretized version of Eq. (3.44) with $\Delta x = \Delta y = \Delta$ is

$$u_{j,l}^{n+1} = u_{j,l}^n + D_u \Delta t \cdot \nabla^2(u_{j,l}) + \Delta t f(u_{j,l}^n, v_{j,l}^n) + \zeta_u \frac{\sqrt{\Delta t}}{\Delta} \eta_{(u)j,l}^n, \quad (3.54)$$

$$v_{j,l}^{n+1} = v_{j,l}^n + D_v \Delta t \cdot \nabla^2(v_{j,l}) + \Delta t g(u_{j,l}^n, v_{j,l}^n) + \zeta_v \frac{\sqrt{\Delta t}}{\Delta} \eta_{(v)j,l}^n, \quad (3.55)$$

where $\nabla^2(u_{j,l})$ and $\nabla^2(v_{j,l})$ have to be replaced by the discretized spatial derivative corresponding to the method used, for a fully discretized scheme.

Depending on the discretization of the spatial derivative this method can be applied to the FTCS and the semi-implicit Crank-Nicolson scheme. However as discussed in Ref. [2] the finite-difference discretization given by Eq. (3.53) converges to the analytic solution if

$$\frac{\Delta^2}{\sqrt{\Delta t}} \rightarrow 0. \quad (3.56)$$

This result means that when using the FTCS scheme the discretization error cannot be minimized below a certain threshold, no matter how fine the discretization is, if we require the algorithm to be stable.

Chapter 4

Patterns in the Lengyel-Epstein model

This chapter gives a detailed analysis of pattern types and transitions observed in the Lengyel-Epstein model. The relevant parameter space with two variables is mapped with respect to the observed patterns, by numerically solving the reaction-diffusion equations. Pattern formation occurs beyond the Turing bifurcation and continues below the Hopf bifurcation.

4.1 Parameter-space of the Lengyel-Epstein model

The Lengyel-Epstein model shows stationary solutions and oscillatory solutions for a small range of the parameter space, when the Hopf bifurcation occurs above the Turing bifurcation. Spatio-temporal patterns are not found for the analyzed parameters.

4.1.1 Stationary solutions

The necessary conditions for Turing instabilities, i.e. pattern formation, in the LE model were derived in section 2.2.2, as a function of the four independent parameters σ , D , a and b , using linear stability analysis.

Experimental restrictions allow to reduce the parameter space to two remaining parameters. First, the two diffusion coefficients are constant¹ and their ratio is close to unity for both iodide and chlorite, as the temperature is held constant during the experiment. Second, the concentration of starch is fixed when preparing the gel in the reactor and the concentration of iodide is not changed during the measurement. Consequently σ can be treated as constant. However the concentration of starch was not given in Ref. [47] and σ also depends on the concentration of iodine, which is an intermediate in the CIMA reaction. Consequently a correct estimate of σ is difficult. According to Ref. [54] acceptable values for the CDIMA reaction are $c = D_v/D_u = 1.07$ and $\sigma \in [1 - 1000]$ depending on the iodine concentrations. Ref. [26] assumes a minimum value of $\sigma = 8$ for the CIMA reaction. The values for the numerical solution have been chosen as $\sigma = 20$ and $c = 1$ for all results presented in this thesis.

¹These diffusion constants are not to be confused with the effective diffusion of iodide, which is significantly influenced by starch and hence the ratio of effective diffusion constants is very different from unity.

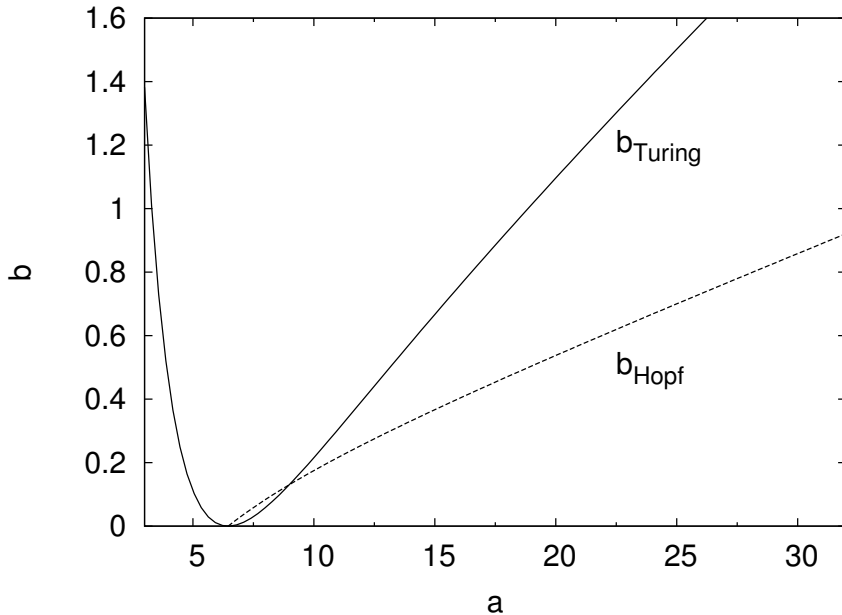


Figure 4.1: Turing and Hopf bifurcation given by Eq. (4.1) and Eq. (4.2) for $\sigma = 20, c = 1$. The intersections occur at $a_1 = 5/3\sqrt{15} \approx 6.455$ and $a_2 = 525/\sqrt{3415} \approx 8.984$. The region above the second intersection between b_H (dashed) and b_T (solid) is where Turing instabilities should occur.

The two remaining parameters, a and b correspond to the constant concentrations of ClO_2^- , I^- and MA in the compartments, which can be varied easily during a series of measurements. Consequently we restrict our analysis to the a - b -parameter space, in particular to regions, where Turing instabilities occur.

As shown in Eq. (2.29) and Eq. (2.30) in section 2.2.2 the Turing and Hopf bifurcations occur along the lines

$$b_H(a) = \frac{1}{\sigma} \left(\frac{3}{5} a - \frac{25}{a} \right), \quad (4.1)$$

$$b_T(a) = \frac{c}{5a} \left(13a^2 + 125 - 4\sqrt{10a}\sqrt{a^2 + 25} \right). \quad (4.2)$$

$$(4.3)$$

Fig. 4.1 shows the Turing and Hopf bifurcation given by Eq. (4.1) and Eq. (4.2) in the a - b -plane for the $\sigma = 20$ and $c = 1$.

Turing pattern formation, i.e. Turing instabilities, should occur for values of b , which lie below the Turing bifurcation and above the Hopf bifurcation. We refer to this region of the parameter space as the Turing region. At different parts of the Turing region different types of patterns can occur. Typical representation of the three ordered states, inverted hexagonal, lamellar and hexagonal, are shown in Fig. 4.2.

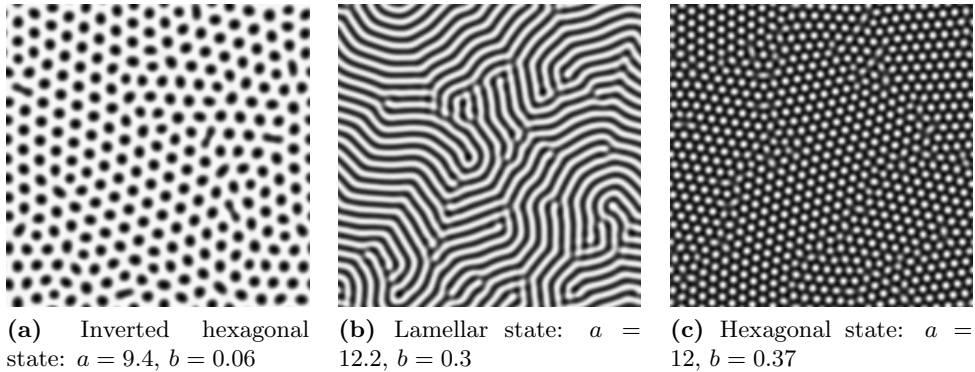


Figure 4.2: Typical patterns for the three different symmetries, which occur in the parameter space. To obtain more detailed patterns the spatial mesh consists of 200 by 200 grid points with a spatial discretization of $\Delta = 1$ solved via Euler forward integration with $\Delta t = 0.01$ and 100000 time-steps.

In the following the patterns obtained for u will be analyzed, while patterns in v will not be treated explicitly. This choice is motivated by the fact that in the experiment the patterns are obtained in the concentration of SI_3^- , which is a function of $[\Gamma^-]$, i.e. u . Additionally in the LE model there is no qualitative morphological difference between patterns in u and v . Fig. 4.3 shows both patterns for the hexagonal state. Both patterns are in phase and barely distinguishable. A slightly smoother concentration gradient is found for v and the absolute values for the concentration are different. As explained in section 2.2.1, this is an important distinction between the LE model and other reaction-diffusion models, such as the Brusselator, where u and v are in opposite phase.

To illustrate the pattern selection in different regions of the parameter space, the numerical solution has been calculated for certain consecutive values from $a = 0.6 - 31.8$ and $b = 0.055 - 1.555$. The system was solved on a mesh of 200×200 grid points with periodic boundary conditions and a spatial discretization $\Delta = 1$ using a FTCS Euler-integration algorithm, as described in section 3.1. The resulting patterns for u after a sufficient number of time-steps are shown in Fig. 4.4. The grey-value is proportional to the concentration of u . Black corresponds to the global maximum and white to the minimum concentration of the patterns, i.e. all concentrations are rescaled to a range from I_{\min} to I_{\max} . I_{\max} can be found for the pattern at $(a, b) = (31.8, 0.205)$ and I_{\min} occurs for the pattern at $(a, b) = (0.6, 1.555)$. Parts of the parameter space, where numerical errors or unphysical negative concentrations occur, are shaded.

Figure 4.5a shows the average concentration $\langle u \rangle$ for each of the patterns in Fig. 4.4 and Fig. 4.5b shows the range of concentrations for each pattern, i.e. the difference

$$\Delta u = u_{\max} - u_{\min} \quad (4.4)$$

for the local minimum and maximum concentrations u_{\max} and u_{\min} . As indicated

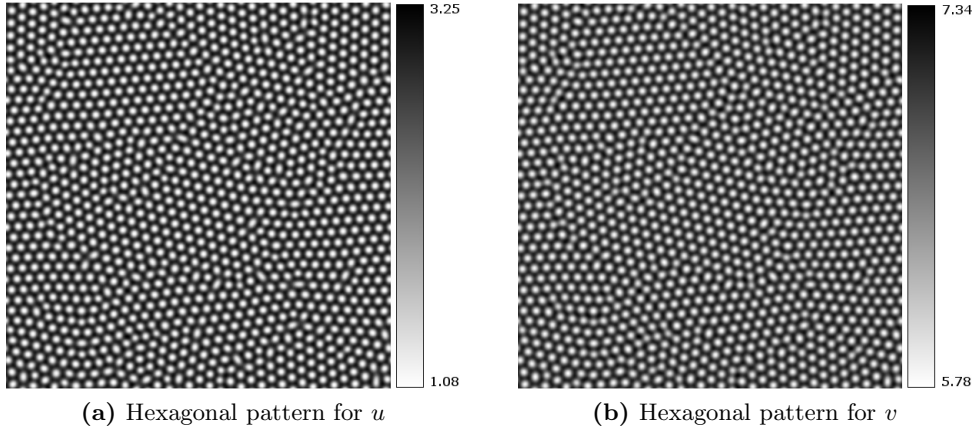


Figure 4.3: Corresponding numerical patterns for u (left) and v (right) for the hexagonal state. Both patterns are in phase, in contrast to other reaction-diffusion models. Here no qualitative morphological difference between both patterns can be observed.

for $b = 0.055$ all patterns except those for $a = 10.2$ and $a = 12.6$ are nearly homogeneous. The transition from a region of stable homogeneous steady states to pattern formation, i.e. the Turing bifurcation line is clearly visible in Fig. 4.5b. The transition is also obvious in Fig. 4.4 where the boundary between heterogeneous patterns and homogeneous solutions is obviously given by the Turing bifurcation. However pattern formation also occurs in regions, where the homogeneous steady state would always be linearly unstable, i.e. the Turing instability is generally preferred over the Hopf instability and a stationary heterogeneous pattern forms instead of an oscillatory solution. As a result the Hopf bifurcation line cannot be identified in the figure.

Looking at Fig. 4.4 the largest variety of patterns can be seen from the onset of pattern formation to a region, where the patterns do not change qualitatively, for larger a or b .

Figure 4.6 gives more detailed information on this part of the parameter space, which reaches from $(a, b) = (10.2, 0.055)$ to $(a, b) = (19.8, 0.805)$.

Within the observed part of the parameter space, hexagonal patterns, inverted hexagonal, i.e. honeycomb patterns, lamellar patterns, mixed states and disordered patterns can be identified. However only lamellar, hexagonal and disordered patterns occur in the Turing instability region. The pattern selection from an inverted hexagonal to a lamellar state can be identified in Fig. 4.6. It is visualized with a more detailed resolution in the parameter region from $a = 7 - 15$ and $b = 0 - 0.2$ in Fig. 4.7. Fig. 4.8 shows the pattern selection from a lamellar state to an hexagonal state in the parameter region of $a = 10.2 - 13.8$ and $b = 0.2 - 0.43$.

A mixture of spots and stripes can be seen in some regions of the parameter space in Fig. 4.6, Fig. 4.7 and Fig. 4.8. This phenomenon is called bistability in the

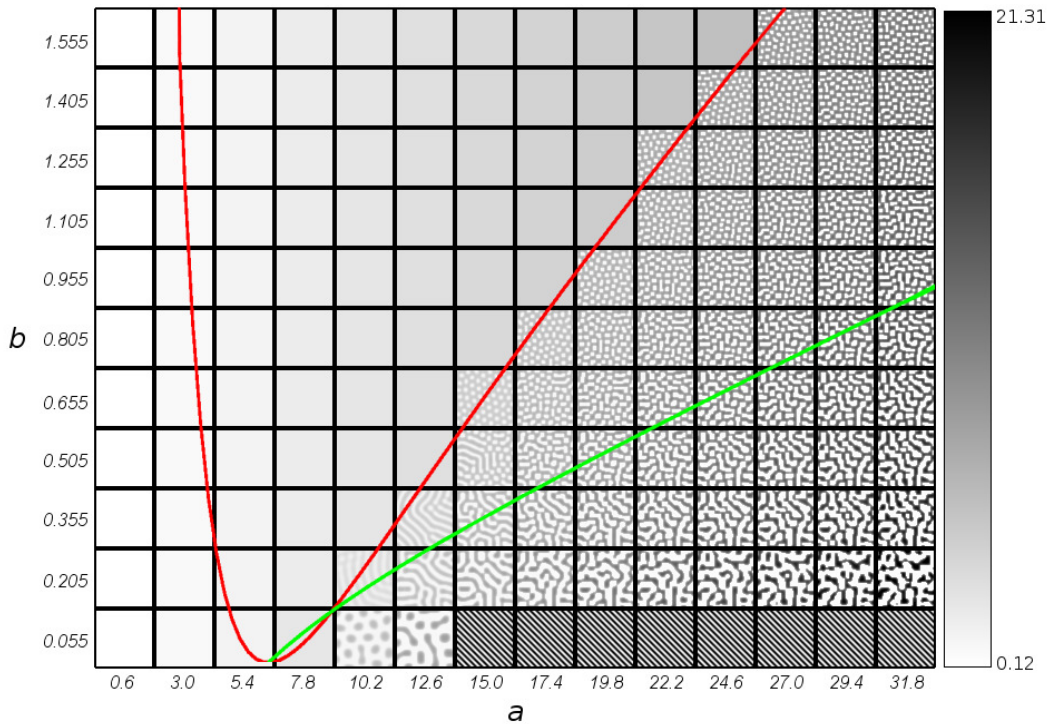
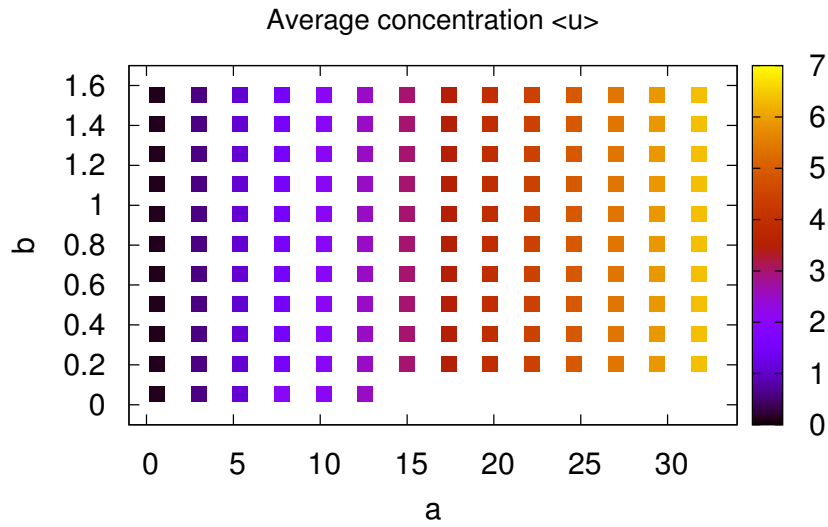


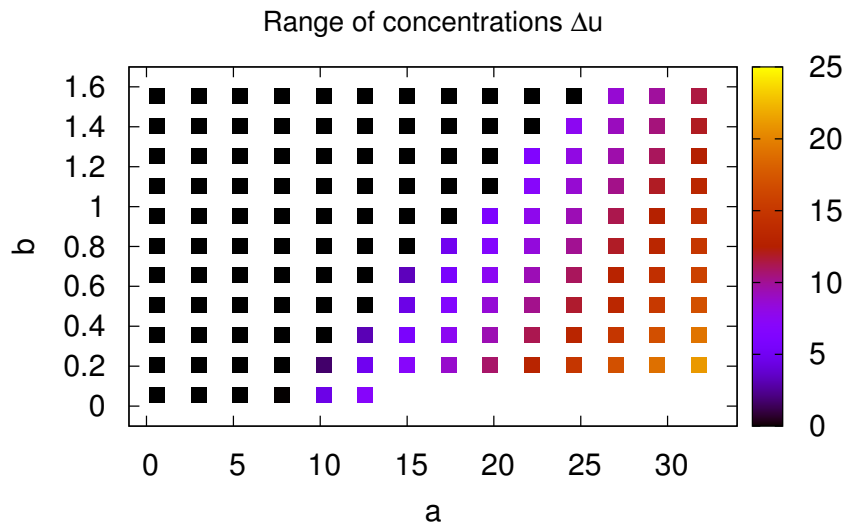
Figure 4.4: Overview of pattern formation in the a - b -plane. Each tile shows a 50x50 pixel sized clip of the numerical solution of the LE model obtained via a FTCS Euler-integration algorithm. The system was solved on a mesh of 200×200 grid points with periodic boundary conditions. All concentration profiles are shown with the same greyscale as shown in the scale bar. Patterns with negative concentrations and overexposed images are shaded. Turing (red) and Hopf bifurcation (green) from Fig. 4.1 are also shown.

mathematics of dynamical systems, i.e. both states are stable solutions for the given parameters. However in the simulation those transient states will evolve to stationary hexagonal or lamellar patterns after a large number of time-steps, while the final state depends on the initial conditions. In general the final state of the system cannot be predicted in bistable regimes and hysteresis is observed [32].

The pattern selection in the parameter space, i.e. the specific regions for each state agree well with the detailed numerical analysis of Ref. [54] and others, see [20, 34, 53, 66] for examples.



(a) Average concentrations for the patterns from Fig. 4.4. The average concentration raised with a and is independent of b .



(b) Range of concentrations for the patterns from Fig. 4.4. A transition from nearly homogeneous to heterogeneous solutions is clearly indicated.

Figure 4.5: The average concentration and the range of concentrations, i.e. the difference between maximum and minimum concentration for the patterns from Fig. 4.4. The color-scale shows the corresponding concentration values.

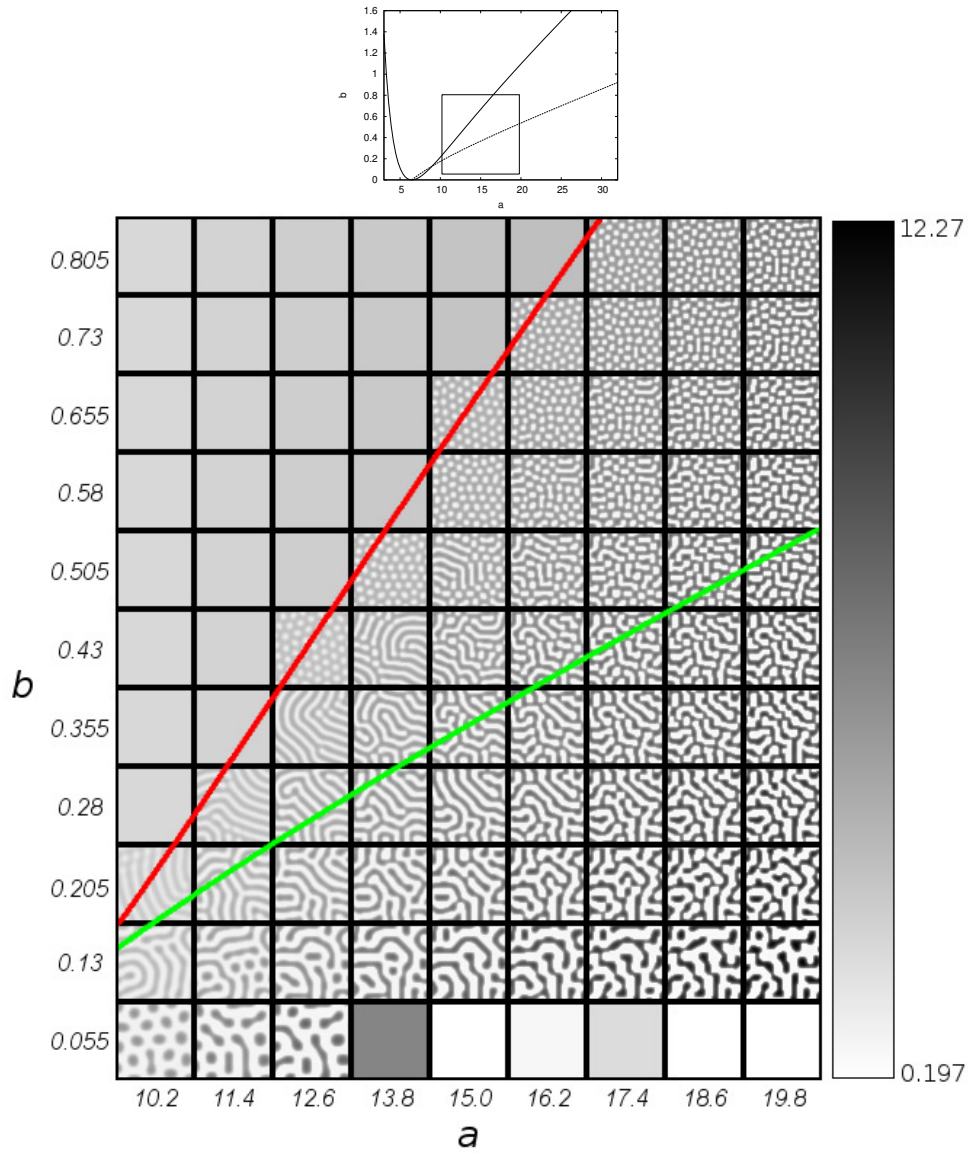


Figure 4.6: A more detailed look at the parameter space for values of $a = 10.2 - 19.8$ and $b = 0.055 - 0.805$. The greyscale on the right shows the corresponding concentrations values. Turing (red) and Hopf bifurcation (green) are also shown.

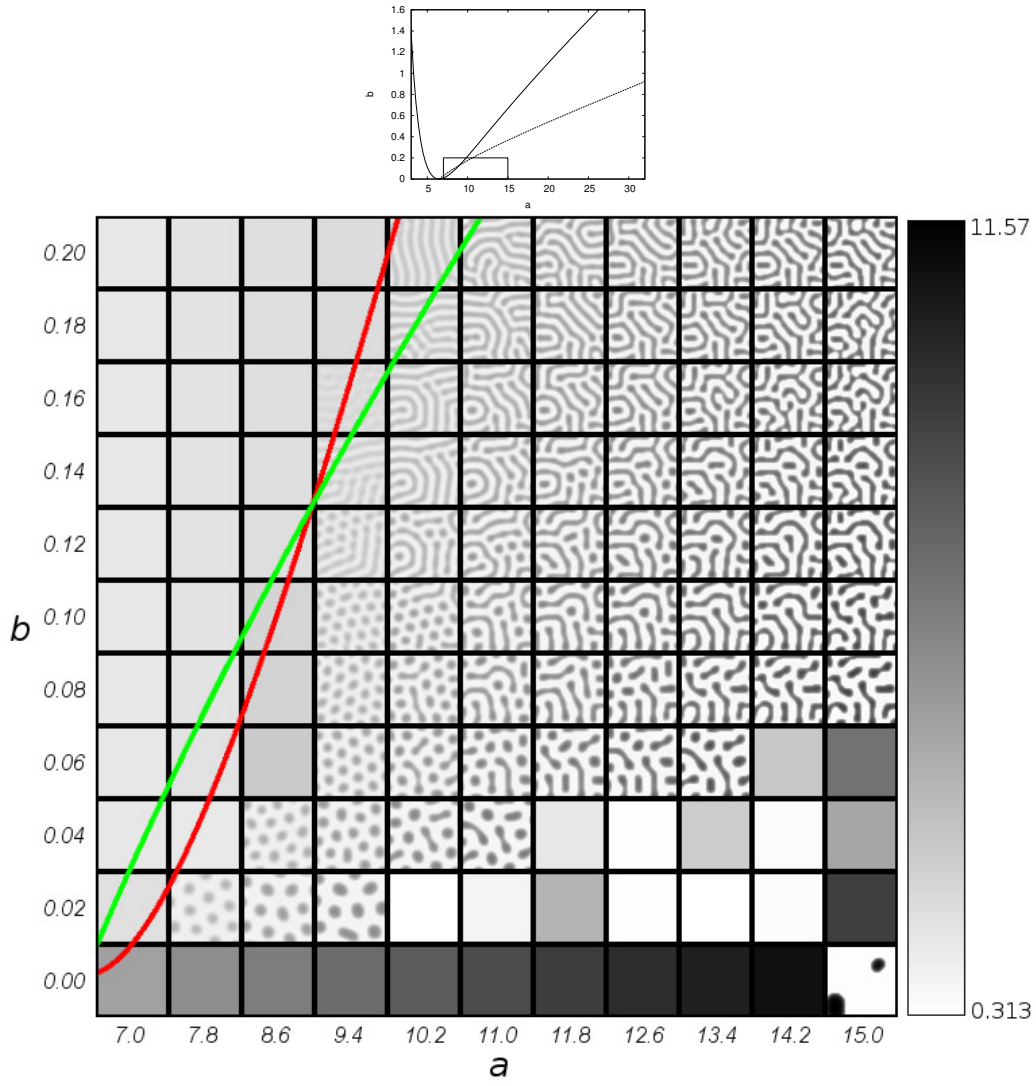


Figure 4.7: Pattern selection from inverted hexagonal to lamellar state in the parameter space for $a = 7 - 15$ and $b = 0 - 0.2$. The greyscale on the right shows the corresponding concentrations values. Turing (red) and Hopf bifurcation (green) are also shown.

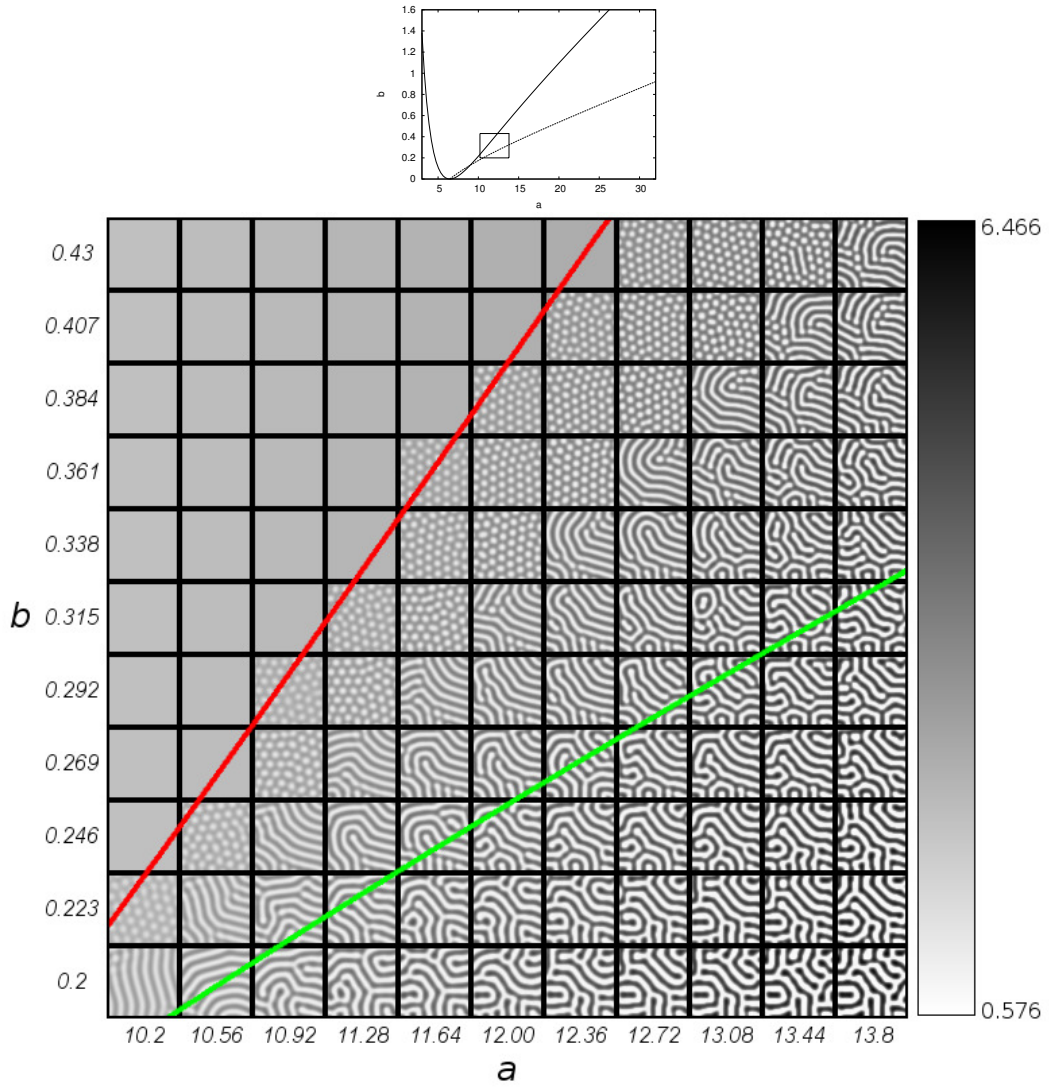


Figure 4.8: Pattern selection from lamellar to hexagonal states in the parameter space for $a = 10.2 - 13.8$ and $b = 0.2 - 0.43$. The greyscale on the right shows the corresponding concentration values. Turing (red) and Hopf bifurcation (green) are also shown.

4.1.2 Oscillatory solutions

Close to the small region of the parameter space in Fig. 4.1, where the Hopf bifurcation occurs for higher values of b than the Turing bifurcation, i.e. from $a_1 \approx 6.455$ to $a_2 \approx 8.984$, the system shows spatial homogeneous oscillatory solutions. The evolutions from a noisy initial state to a homogeneous oscillatory state can be visualized by plotting the average concentration $\langle u \rangle$ of a solution over the simulation time as shown in Fig. 4.9. The time evolution of Δu shows how the system converges to a homogeneous state.

Oscillatory hexagonal patterns, such as obtained in Ref. [53] in a normal-form analysis, were not found for direct numerical integration of the LE model. As reported in Ref. [42] oscillatory hexagonal spots can only be found in the CIMA reaction with a constant background illumination (the CIMA reaction is a photosensitive reaction) as a further control parameter and numerically a much smaller value of σ has to be assumed.

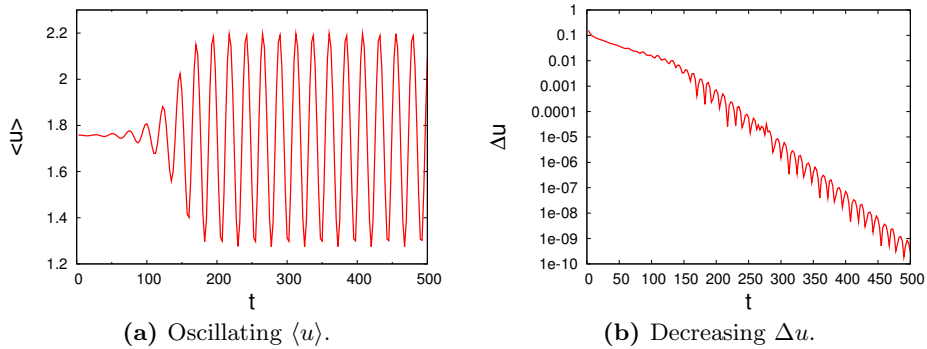


Figure 4.9: The system converges to a homogeneous oscillatory solution in the parameter space of the LE model at $(a, b) = (8.784, 0.118)$.

4.2 Concentration fluctuations of stable homogeneous states

When plotting the patterns with a local greyscale, i.e. with maximum and minimum concentrations of each pattern corresponds to black and white, also the numerical solutions above the Turing bifurcation show patterns. This results in pattern solutions with very small amplitude for parameters above the Turing bifurcation. Note that the same greyscale values in each picture correspond to very different concentrations.

For values of b above the Turing bifurcation the range of concentrations is so small, as indicated in Fig. 4.5b that the patterns seen in the numerical solutions can be con-

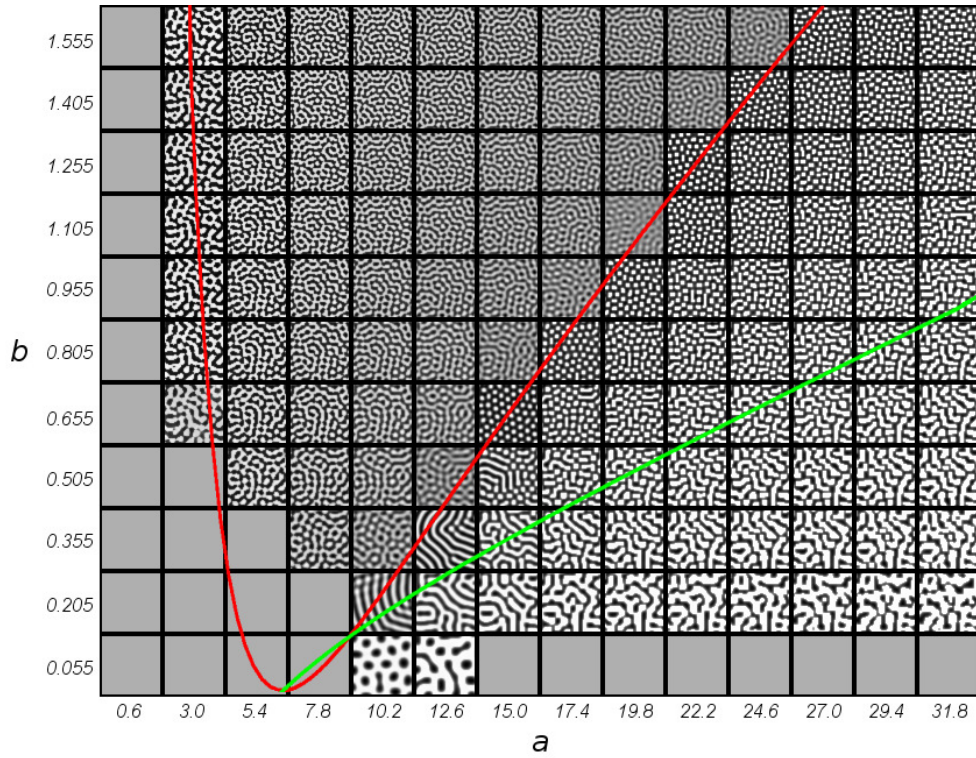


Figure 4.10: The concentration profiles in the analyzed parameter region with a local greyscale. Turing (red) and Hopf bifurcation (green) from Fig. 4.1 are also shown.

sidered merely as artefacts of the non-homogeneous initial conditions. The change of concentrations is at least $10^{-8} \times \langle u \rangle$ smaller, with the average concentration $\langle u \rangle$. Given the numerical accuracy of our finite-difference method, the very low intensity patterns above the Turing bifurcation cannot be rigorously analyzed. It is unclear if they are all numerical artefacts or the result of the nonlinearity of the reaction terms in the LE model. In accordance with Ref. [54] they are considered as homogeneous solutions.

Chapter 5

Morphology of experimental and numerical Turing patterns

Minkowski functionals are introduced as a morphological measure for binary images, following the approach of work of Mecke [37] who morphologically characterized experimental CIMA patterns from Ouyang and Swinney [47]. We apply the same analysis to the experimental data from Ouyang and Swinney and extend it to numerical patterns from the LE model.

The comparison of the Minkowski functionals of experimental and numerical patterns shows a distinct difference in the morphology of the concentration profiles. However, locally in regions of the experimental images that appear well ordered, an agreement between the two patterns is found. A systematic approach, based on the so-called Minkowski-maps, is used to characterize these local variations in the experimental patterns.

5.1 Minkowski analysis for 2D images

Morphological descriptors, so-called Minkowski functionals, are used to characterize the Turing patterns given as 2D greyscale images that are converted to binary black-and-white images using standard thresholding. A marching-square algorithm is used for the numerical calculation of the Minkowski functionals. For a comparison of patterns with different size or image resolution the Minkowski functionals are normalized with the characteristic wavelength obtained by a covering radius transform (CRT) [41].

5.1.1 Minkowski functionals for bodies in \mathbb{E}^2

Integral geometry defines a suitable family of morphological descriptors, the so-called Minkowski functionals, which can be used for a morphological characterization of a black-and-white image, as explained in Ref. [35].

For a body (as a compact set) A with bounding curve ∂A in two dimensional Euclidean space \mathbb{E}^2 three Minkowski functionals exist, namely area, perimeter and

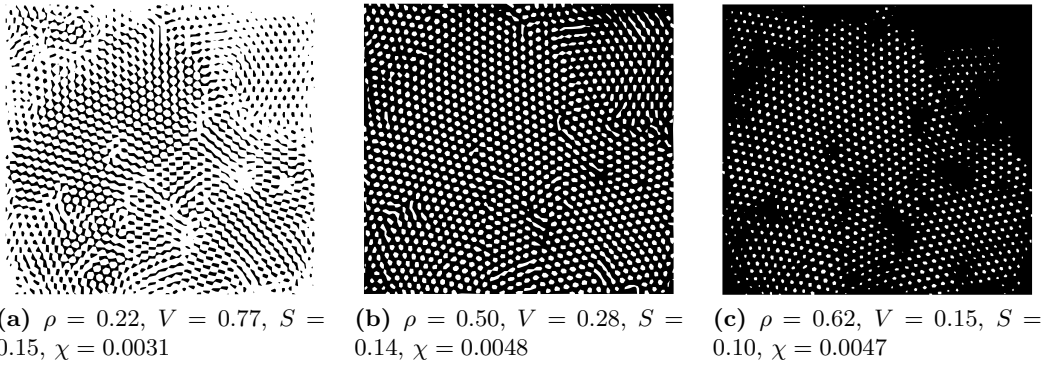


Figure 5.1: Monochrome images generated from the hexagonal Turing Pattern from Fig. 2.3 for different thresholds ρ with the corresponding Minkowski functionals.

Euler characteristic, as given by

$$M_0(A) = \int_A d^2\vec{r}, \quad M_1(A) = \frac{1}{2\pi} \int_{\partial A} d\vec{r}, \quad M_2(A) = \frac{1}{2\pi^2} \int_{\partial A} \frac{1}{R} d\vec{r}. \quad (5.1)$$

The area M_0 is simply the covering area of A , while the perimeter M_1 is the boundary length of the domain. The Euler characteristic M_2 gives the difference of the number of connected components of A and its complement $\mathbb{E}^2 \setminus A$.

Consider for example a white circle of radius r . The area V , perimeter S and Euler characteristic χ are then given by

$$V = \pi r^2, \quad S = 2\pi r, \quad \chi = 1. \quad (5.2)$$

The Minkowski functionals defined in Eq. (5.1) are only defined for black-and-white images. As described in the following section Minkowski functionals can also be used to analyze greyscale images, however the thresholding value ρ has to be introduced as an additional parameter.

5.1.2 Minkowski functionals for pixelized images

The concentration profiles from the experiments and numerical calculation are given as greyscale images. For the Minkowski analysis those concentration profiles are converted to binary images by thresholding. Therefore a threshold parameter ρ is introduced and binary images are created from the greyscale concentration profiles, i.e. all pixels with a grey-value above ρ are set to white, and all below are set to black. Minkowski functionals are then calculated for each resulting monochrome image and analyzed as a function of ρ . Fig. 5.1 shows the resulting binary images for an experimental Turing pattern for three different thresholds. Obviously the Minkowski functionals depend strongly on ρ . This functional dependence on the

threshold makes Minkowski functionals a very convenient measure to characterize the morphology of greyscale images.

To compare images of different size it is convenient to normalize all measures by the total area A of the picture. Therefore we define

$$V = \frac{M_0}{A}, \quad S = \frac{M_1}{A}, \quad \chi = \frac{M_2}{A}. \quad (5.3)$$

For the pixelized datasets, which are obtained in experiments and numerical calculations, the Minkowski functionals are calculated on a polygonal interface obtained by a marching square algorithm [35]. This algorithm reduces the error due to the discretization, relative to a pixel based algorithm, as used in Ref. [37].

5.1.3 Analysis of greyscale images and length scale normalisation

For some comparisons of experimental and numerical patterns, i.e. when the resolution of the patterns is different, the Minkowski functionals have to be rescaled. Furthermore the artefact of a white balance processes during the measurement have to be considered to exclude differences for the generic behavior of the Minkowski functionals, i.e. for values of ρ close to zero and unity.

Characteristic length-scale

The Minkowski functionals defined in Eqs. 5.3 are not dimensionless, but scale with the length scale $\langle D \rangle$ as $S \sim \langle D \rangle$ and $\chi \sim \langle D \rangle^2$. For a detailed quantitative comparison of the experimental and numerical patterns the length scale of the patterns has to be considered. The maximum value of the perimeter and the Euler characteristic depend on the length scale of the analyzed patterns. As experimental and numerical patterns can have a different resolutions the perimeter and Euler characteristic have to be rescaled accordingly to get dimensionless measures, i.e. with $\langle D \rangle$ for the perimeter and $\langle D \rangle^2$ for the Euler characteristic, where $\langle D \rangle$ is the characteristic length scale. The quantity $\langle D \rangle$ can be obtained by a covering radius transform (CRT) [41]. A CRT fills either the white or the black region of a binary image with circles starting from the largest radius possible to smaller radii and producing a greyscale image where each pixel has a grey-value corresponding to the radius of the circle it is contained in. The resulting greyscale image is shown in a histogram and averaged. Depending on the threshold the average grey-value gives a characteristic length scale. The procedure is illustrated in Fig. 5.2.

The CRT of the white and black phase respectively depends greatly on the threshold ρ as illustrated in Fig. 5.3 for $\rho = 0.004$ and $\rho = 0.2$ and shown in Fig. 5.4. However the sum of average radii for black and white regions is less sensitive to ρ and shows a plateau for values of ρ not close to zero or unity, as shown in Fig. 5.4. This value for intermediate ρ gives an approximation of the length-scale for the patterns.

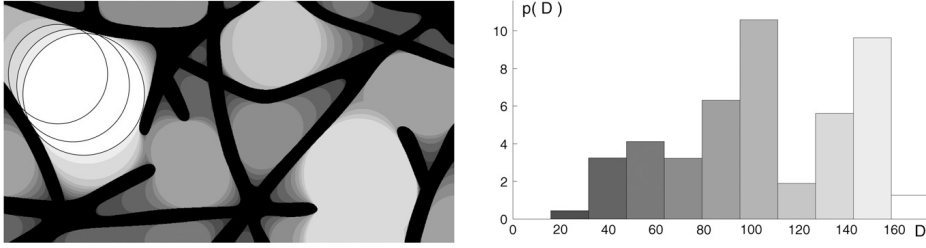
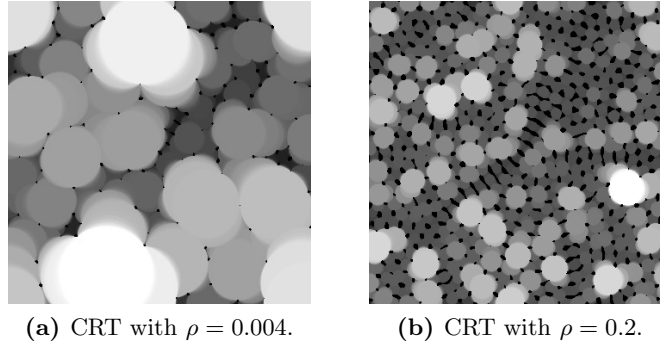


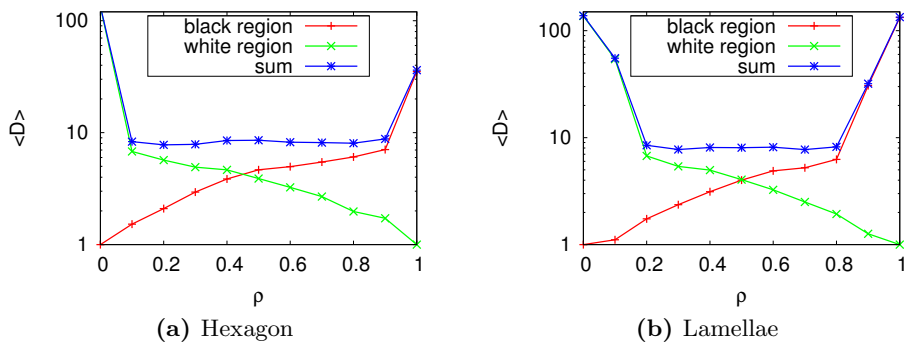
Figure 5.2: Illustration for the maximal covering radius transform of the fluid phase of a collagen network from [41]. (Left) The black parts of the image show a two-dimensional schematic representation of a collagen gel. The grey-value of each pixel in the white region, i.e. a fluid phase, corresponds to the maximal covering radius transform value D . It represents the radius of the largest sphere that covers the pixel and is fully contained in the fluid phase. For clarity, some of the disks have been highlighted by an outline. (Right) The colors in histogram that shows the distribution of the maximal covering radii provide a bar chart mapping of the radius D to color. (Images reproduced from Ref. [41])



(a) CRT with $\rho = 0.004$.

(b) CRT with $\rho = 0.2$.

Figure 5.3: The covering radius transform (CRT) for black or white regions depends greatly on ρ .



(a) Hexagon

(b) Lamellae

Figure 5.4: The sum of average radii for black and white regions obtained by a CRT depending on the threshold for the hexagonal and lamellar patterns from Fig. 5.8. The value of the plateau gives an estimate of the characteristic length scale of the pattern.

Greyscale of experimental patterns

Another influence on the ρ dependence of the Minkowski functionals is given by the experiment, as for the measurement of the concentration profiles a region of best illumination was chosen for the images, i.e. a maximum and minimum intensity. Consequently a few underexposed and overexposed pixels may appear, while the majority lies within the range of I_{\max} and I_{\min} . Whenever tails occur in the histogram of numerical pattern, such as in those proposed in chapter 7 a similar procedure has to be applied to the numerical patterns.

An example is shown in Fig. 5.5. The histogram shows tails of only a few darkest and lightest pixel. These tails are cut off, i.e. 0.05% of the darkest and lightest pixel are set to 255, respectively, while the remaining grey-values are stretched over the 256 original grey-values. The process is illustrated in Fig. 5.5, where the original and post-processed pattern is shown.

This procedure is necessary for the patterns in section 7.2 and was not realized at the beginning of the analysis. However it only effects the generic behavior of the Minkowski functionals, i.e. for thresholds close to zero and unity.

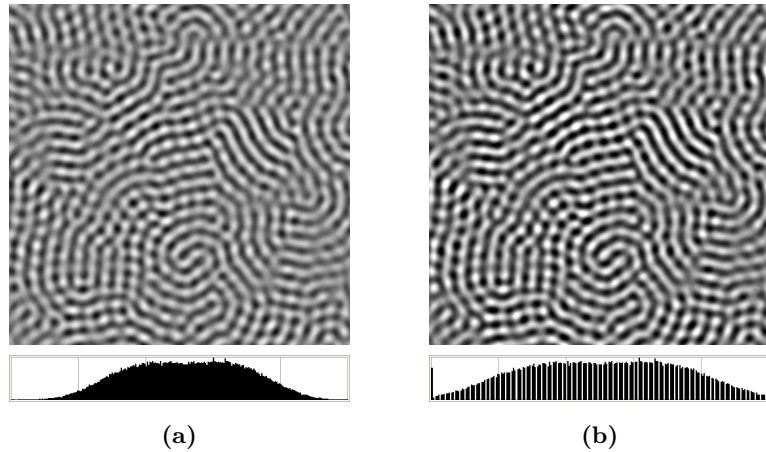


Figure 5.5: Superposed numerical pattern from chapter 7 before and after cutting off the dark and light "tails" with the corresponding histogram shown below.

5.2 Minkowski functionals of patterns in the CIMA reaction

In this section the Minkowski functionals are analyzed for characteristic experimental datasets, one hexagonal, one lamellar and one turbulent pattern. The three patterns and the corresponding Minkowski functionals are shown in Fig. 5.6.

The area $V(\rho)$ decreases monotonously from 1 to 0 for all three states. An obvious difference between the hexagonal and the lamellar and turbulent state is the asymmetry of the Minkowski functionals with respect to ρ for the hexagonal pattern, whereas for the lamellar and turbulent patterns they are quite symmetric. The

perimeter $S(\rho)$ and the Euler characteristic $\chi(\rho)$ tend to zero for nearly white and nearly black images. However a small difference from zero is also indicated for all patterns, when $\rho = 0$, which is related to a few black pixels with grey-values exactly 0. The Euler characteristic is negative for ρ , where disconnected black components dominate the image and positive for ρ , where disconnected white components dominate the image. The transition from a negative to a positive Euler characteristic occurs close to $\rho = 0.5$ for lamellar and turbulent patterns, while the dominance of connected black parts in the hexagonal patterns leads to a transition from negative to positive at $\rho = 0.3$.

As shown in Ref. [37] stationary and turbulent states can be characterized quantitatively by introducing simple combinations of $V(\rho)$, $S(\rho)$ and $\chi(\rho)$, which are found to be accurately described by polynomials up to fourth order in ρ . Particularly those quantities are given by

$$P_V(\rho) = \operatorname{atanh}(2V(\rho) - 1), \quad (5.4)$$

$$P_S(\rho) = \frac{S(\rho)}{V(\rho)(1 - V(\rho))}, \quad (5.5)$$

$$P_\chi(\rho) = \frac{\chi(\rho)}{S(\rho)} \quad (5.6)$$

and it is assumed that they are well approximated by

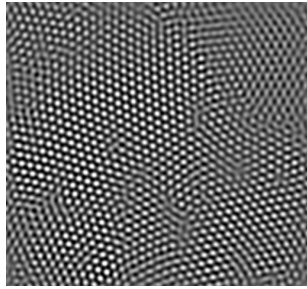
$$P_V(\rho) = P_V^{(0)} + P_V^{(1)} \rho + P_V^{(2)} \rho^2 + P_V^{(3)} \rho^3, \quad (5.7)$$

$$P_S(\rho) = P_S^{(0)} + P_S^{(1)} \rho + P_S^{(2)} \rho^2 + P_S^{(3)} \rho^3 + P_S^{(4)} \rho^4, \quad (5.8)$$

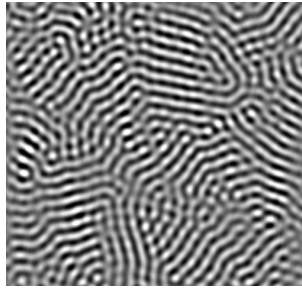
$$P_\chi(\rho) = P_\chi^{(0)} + P_\chi^{(1)} \rho + P_\chi^{(2)} \rho^2 + P_\chi^{(3)} \rho^3. \quad (5.9)$$

The obtained curves from Eq. (5.4 - 5.6) together with the corresponding polynomial fits are shown in Fig. 5.7. For convenience ρ is normalized to the interval $[-1, 1]$. There is an almost perfect agreement of the measured data and the polynomial fits. The coefficients of P_V , P_S and P_χ are given in Table 5.1a.

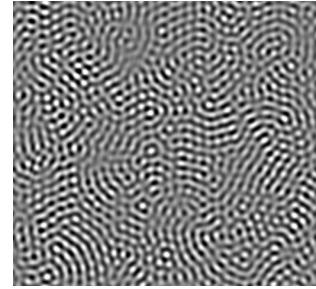
It is argued in Ref. [37] that the polynomial coefficients are characteristic for each state and can be used to visualize the transition between patterns of different phases. The fit coefficients obtained for the experimental patterns are in good agreement with the typical values given in Ref. [37], which are shown in Table 5.1b. The slight difference can be explained by the use of the marching squares algorithm to determine to Minkowski functionals, while a pixel based algorithm has been used in Ref. [37].



(a) Experimental hexagonal pattern. Initial concentrations are: $[\text{ClO}_2^-]_0 = 20\text{mM}$, $[\text{H}_2\text{SO}_4]_0 = 100\text{mM}$, $[\text{I}^-]_0 = 3\text{mM}$, $[\text{MA}]_0 = 9\text{mM}$, $[\text{Na}_2\text{SO}_4]_0 = 4.5\text{mM}$, $[\text{H}_2\text{SO}_4]_0 = 0.5\text{mM}$ and $T = 6.2^\circ\text{C}$. See Fig. 10 in [47].



(b) Experimental lamellar pattern. Initial concentrations are: $[\text{MA}]_0 = 11\text{mM}$, $[\text{I}^-]_0 = 3\text{mM}$, $[\text{ClO}_2^-]_0 = 18\text{mM}$, $[\text{Na}_2\text{SO}_4]_0 = 4.5\text{mM}$, $[\text{H}_2\text{SO}_4]_0^{\text{A}} = 0.5\text{mM}$, $[\text{H}_2\text{SO}_4]_0^{\text{B}} = 8.5\text{mM}$ and $T = 5.8^\circ\text{C}$. See Fig. 7 in [47].



(c) Experimental turbulent pattern. Initial concentrations are: $[\text{ClO}_2^-]_0 = 20\text{mM}$, $[\text{H}_2\text{SO}_4]_0 = 10\text{mM}$, $[\text{I}^-]_0 = 3\text{mM}$, $[\text{MA}]_0 = 9\text{mM}$, $[\text{Na}_2\text{SO}_4]_0 = 4.5\text{mM}$, $[\text{H}_2\text{SO}_4]_0 = 0.5\text{mM}$ and $T = 6.2^\circ\text{C}$. See Fig. 10 in [47].

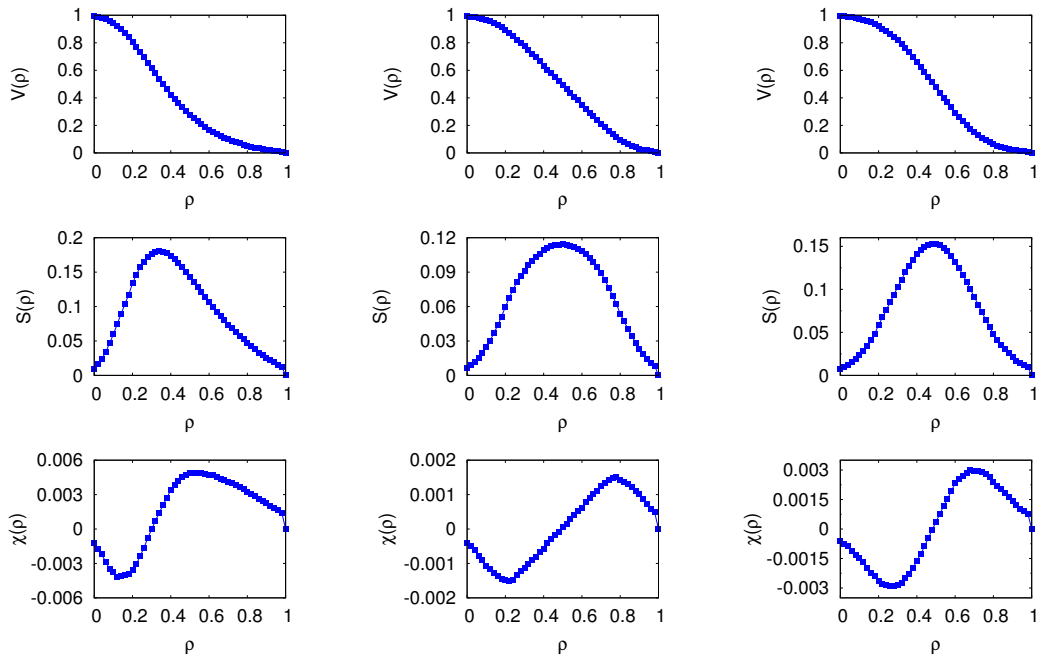
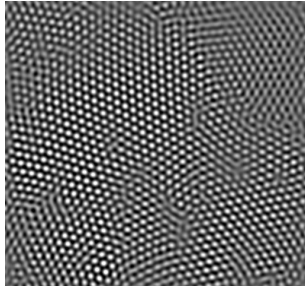
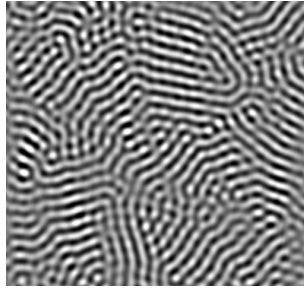


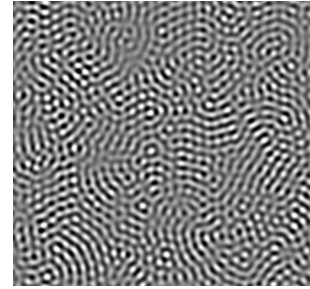
Figure 5.6: Hexagonal and lamellar Turing patterns obtained in the CIMA-reaction (see Ref. [47]) with corresponding Minkowski functionals shown below each pattern.



(a) Experimental hexagonal pattern. Initial concentrations are: $[\text{ClO}_2^-]_0 = 20\text{mM}$, $[\text{H}_2\text{SO}_4]_0 = 100\text{mM}$, $[\text{I}^-]_0 = 3\text{mM}$, $[\text{MA}]_0 = 9\text{mM}$, $[\text{Na}_2\text{SO}_4]_0 = 4.5\text{mM}$, $[\text{H}_2\text{SO}_4]_0 = 0.5\text{mM}$ and $T = 6.2^\circ\text{C}$. See Fig. 10 in [47].



(b) Experimental lamellar pattern. Initial concentrations are: $[\text{MA}]_0 = 11\text{mM}$, $[\text{I}^-]_0 = 3\text{mM}$, $[\text{ClO}_2^-]_0 = 18\text{mM}$, $[\text{Na}_2\text{SO}_4]_0 = 4.5\text{mM}$, $[\text{H}_2\text{SO}_4]_0^{\text{A}} = 0.5\text{mM}$, $[\text{H}_2\text{SO}_4]_0^{\text{B}} = 8.5\text{mM}$ and $T = 5.8^\circ\text{C}$. See Fig. 7 in [47].



(c) Experimental turbulent pattern. Initial concentrations are: $[\text{ClO}_2^-]_0 = 20\text{mM}$, $[\text{H}_2\text{SO}_4]_0 = 10\text{mM}$, $[\text{I}^-]_0 = 3\text{mM}$, $[\text{MA}]_0 = 9\text{mM}$, $[\text{Na}_2\text{SO}_4]_0 = 4.5\text{mM}$, $[\text{H}_2\text{SO}_4]_0 = 0.5\text{mM}$ and $T = 6.2^\circ\text{C}$. See Fig. 10 in [47].

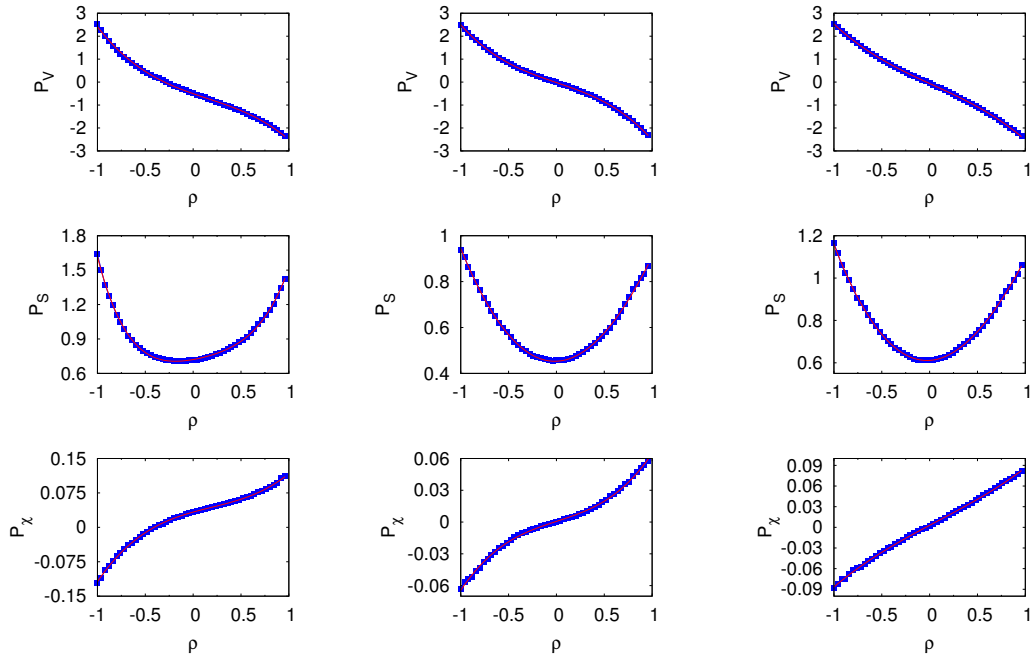


Figure 5.7: Functions P_V , P_S and P_χ defined by Eq. (5.4 - 5.6) (blue) calculated from the Minkowski functionals of the experimental patterns and polynomial fit according to Eq. (5.7), Eq. (5.8) and Eq. (5.9) (red, solid). The fit coefficients are shown in Table 5.1a.

Table 5.1: Coefficients for the polynomial fits in Fig. 5.7 and coefficients given in Ref. [37] as typical values for the experimental patterns. A good agreement with the previous results is found. The slight difference can be explained by the use of the marching squares algorithm to determine the Minkowski functionals.

Pattern type, μ	$P_\mu^{(0)}$	$P_\mu^{(1)}$	$P_\mu^{(2)}$	$P_\mu^{(3)}$	$P_\mu^{(4)}$
Hexagon, V	-0.50	-1.46	0.46	-1.00	–
Hexagon, S	0.72	0.15	0.31	-0.20	0.54
Hexagon, χ	0.033	0.058	-0.034	0.059	–
Lamellae, V	(-0.021)	-1.42	(0.011)	-1.08	–
Lamellae, S	0.45	(0.017)	0.48	(-0.034)	(-0.006)
Lamellae, χ	(0.0006)	0.030	(-0.0004)	0.035	–
Turbulent, V	(-0.061)	-1.91	(0.067)	-0.61	–
Turbulent, S	0.611	(0.029)	0.52	(-0.063)	(-0.0064)
Turbulent, χ	(0.003)	0.074	(-0.003)	(0.012)	–

(a) Best fit coefficients for experimental patterns according to Eq. (5.7 - 5.9) from Ref. [37]. Values which are at least one magnitude smaller than the dominant coefficient are set in parentheses to illustrate the apparent symmetry.

Pattern type, μ	$P_\mu^{(0)}$	$P_\mu^{(1)}$	$P_\mu^{(2)}$	$P_\mu^{(3)}$	$P_\mu^{(4)}$
Hexagon, V	-0.45	-1.59	0.397	-0.82	–
Hexagon, S	0.83	0.14	0.43	-0.18	0.36
Hexagon, χ	0.024	0.056	-0.025	0.033	–
Lamellae, V	(-0.0096)	-1.39	(0.030)	-1.09	–
Lamellae, S	0.55	(-0.021)	0.599	(0.035)	(-0.062)
Lamellae, χ	(-0.00020)	0.024	(-0.000013)	0.031	–
Turbulent, V	(-0.063)	-1.93	(0.058)	-0.536	–
Turbulent, S	0.697	(0.019)	0.554	-0.4	(-0.023)
Turbulent, χ	(0.0026)	0.063	(-0.0039)	(0.0044)	–

(b) Best fit coefficients for experimental patterns according to Eq. (5.7 - 5.9) from Ref. [37]. Values which are at least one magnitude smaller than the dominant coefficient are set in parentheses to illustrate the apparent symmetry.

5.3 Minkowski functionals of simulated patterns in the LE model

The agreement between pattern formation in the Lengyel-Epstein model and the CIMA reaction with respect to wavelength and pattern type has been investigated in Ref. [54]. Theoretical predictions such as the transition from homogeneous steady states to Turing patterns have been found to be in good agreement, despite the simplifications of the model. There is however no quantitative comparison of the concentration profiles between the experimental and numerical patterns, except for their characteristic wavelength.

In this section image analysis via Minkowski functionals is used as a quantitative approach to compare experimental and numerical data, with respect to the pattern morphology. For this analysis Minkowski functionals have been calculated for the numerical solutions of the two-variable LE model with a given set of parameters a, b, D and σ , representing a typical hexagonal and lamellar state, respectively.

Fig. 5.8 shows the numerical patterns calculated for the hexagonal and lamellar state, as well as the corresponding Minkowski functionals. The functions P_V , P_S and P_χ for the numerical patterns are shown in Fig. 5.9 with the corresponding coefficients of the best fits in Table 5.2.

A significant difference between LE and experimental patterns is clearly indicated for both, hexagonal and lamellar patterns. The strong discrepancy is illustrated in Fig. 5.10 and Fig. 5.11, where both, experimental and numerical Minkowski functionals are plotted.

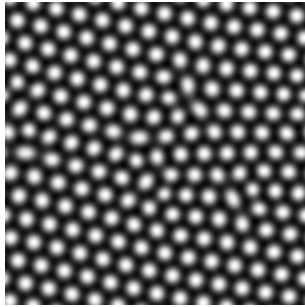
These differences, particularly the plateau that forms in the perimeter and the Euler characteristic for the numerical patterns persist for any numerical and experimental pattern of the same state. These plateaus are the consequence of the well ordered structure of the numerical patterns, whereas the experimental patterns do not appear well-ordered. Obviously a perfectly ordered hexagonal pattern would show a plateau of constant value in the Euler characteristic, as this corresponds to thresh-

Table 5.2: Polynomial fit coefficients found for the numerical patterns from Fig. 5.8 with the corresponding plots in Fig. 5.9.

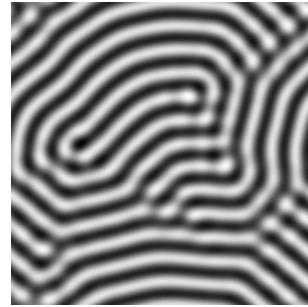
Pattern type, μ	$P_\mu^{(0)}$	$P_\mu^{(1)}$	$P_\mu^{(2)}$	$P_\mu^{(3)}$	$P_\mu^{(4)}$
Hexagon, V	-0.59	-0.14	0.91	2.74	–
Hexagon, S	0.70	0.20	-0.36	-0.53	2.06
Hexagon, χ	0.046	-0.061	-0.082	0.28	–
Lamellae, V	-0.028	-1.38	0.38	-1.37	–
Lamellae, S	0.74	0.19	-1.02	-0.50	3.17
Lamellae, χ	0.0023	-0.057	-0.020	0.25	–

olds, where the image is filled by white spots that constantly decrease in size, but their number remains the same. A similar behavior can be expected for the perimeter of perfectly lamellar patterns. For a certain threshold, stripes that only decrease in their thickness will form, but the perimeter stays the same, when the borders are excluded.

To fully understand the differences between experimental and numerical patterns the effect of the local unordered parts in the experimental patterns has to be analyzed. This can be done by a local analysis of the experimental patterns, which reveals significant local variations in the experimental concentration profiles, as shown in the following section.



(a) Numerical hexagonal pattern, $b = 0.37$, $a = 12$, $D = 1$, $\sigma = 20$



(b) Numerical lamellar pattern, $b = 0.205$, $a = 10.2$, $D = 1$, $\sigma = 20$

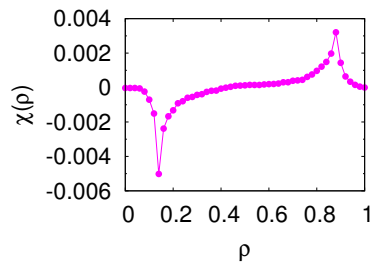
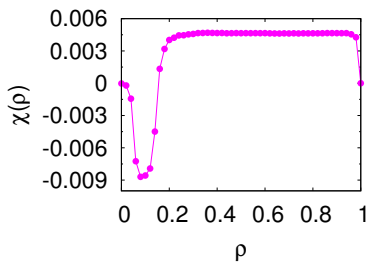
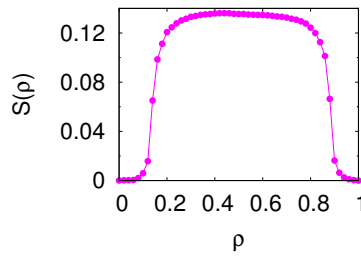
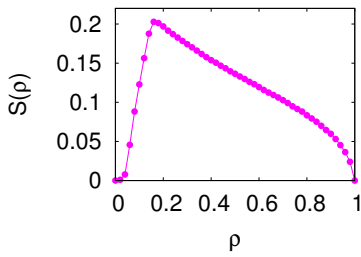
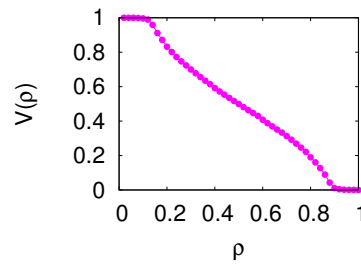
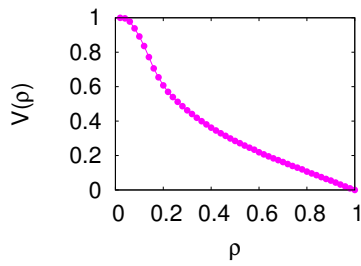
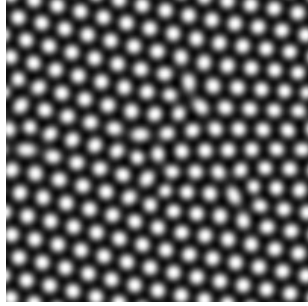
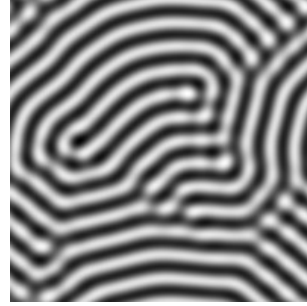


Figure 5.8: Hexagonal and lamellar Turing patterns obtained in the numerical solution of the LE-Model with corresponding Minkowski functionals shown below each pattern.



(a) Numerical hexagonal pattern, $b = 0.37$, $a = 12$, $D = 1$, $\sigma = 20$



(b) Numerical lamellar pattern, $b = 0.205$, $a = 10.2$, $D = 1$, $\sigma = 20$

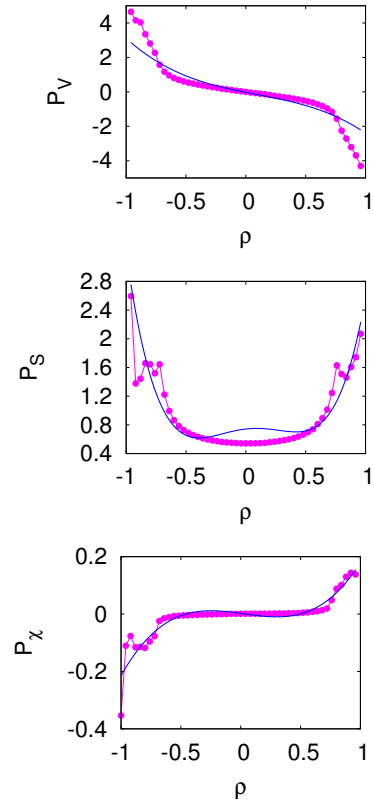
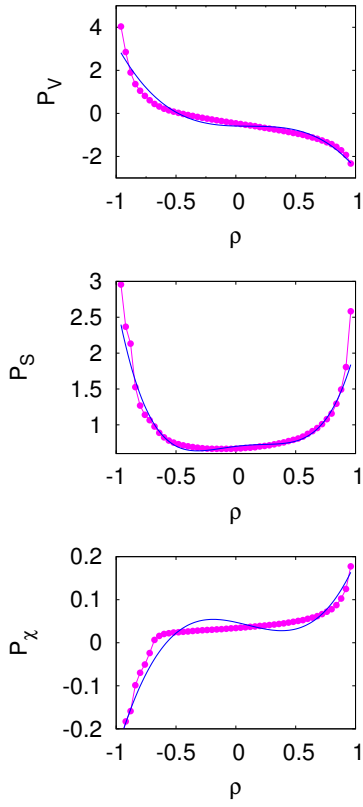
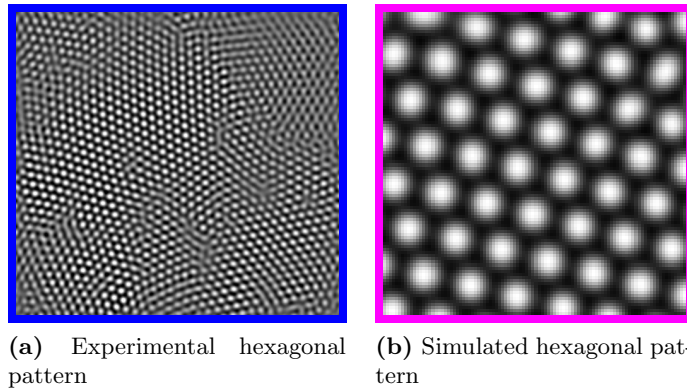


Figure 5.9: Functions P_V , P_S and P_χ defined by Eq. (5.4 - 5.6) (magenta) calculated from the Minkowski functionals and polynomial fits according to Eq. (5.7), Eq. (5.8) and Eq. (5.9) (blue, solid) for the numerical patterns. The fit coefficients are shown in Table 5.2.



(a) Experimental hexagonal pattern (b) Simulated hexagonal pattern

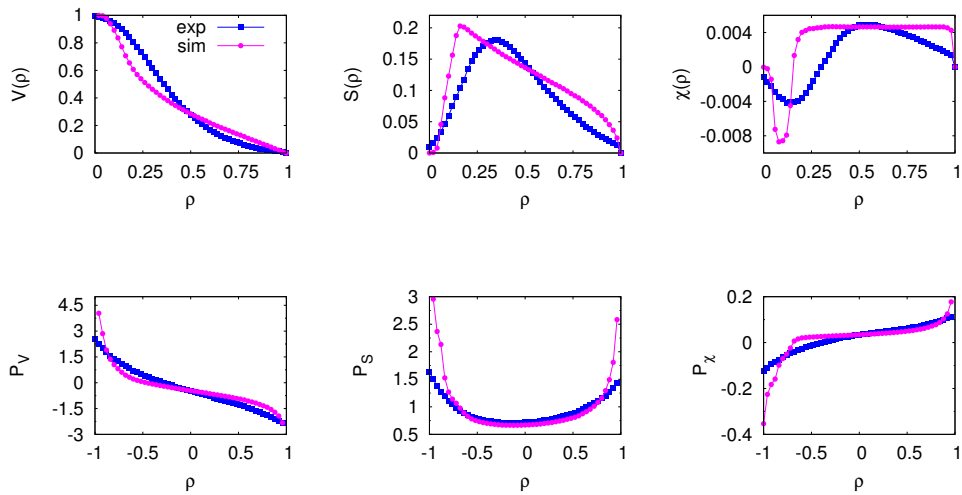
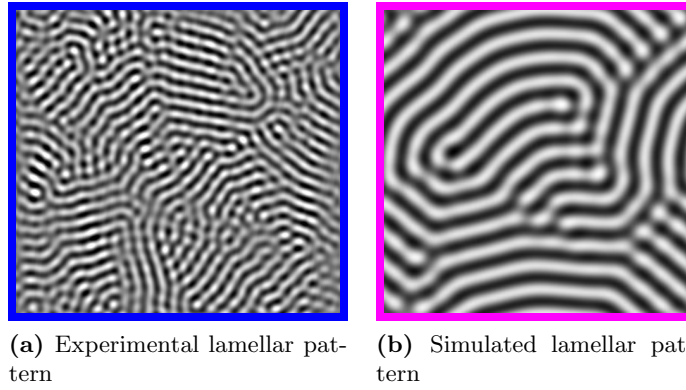


Figure 5.10: Experimental (blue) and numerical (magenta) hexagonal pattern from Fig. 5.6 and the numerical pattern from Fig. 5.8 with the corresponding Minkowski functionals and P_V , P_S , P_χ below. Experimental and numerical patterns show a qualitative morphological difference.



(a) Experimental lamellar pattern

(b) Simulated lamellar pattern

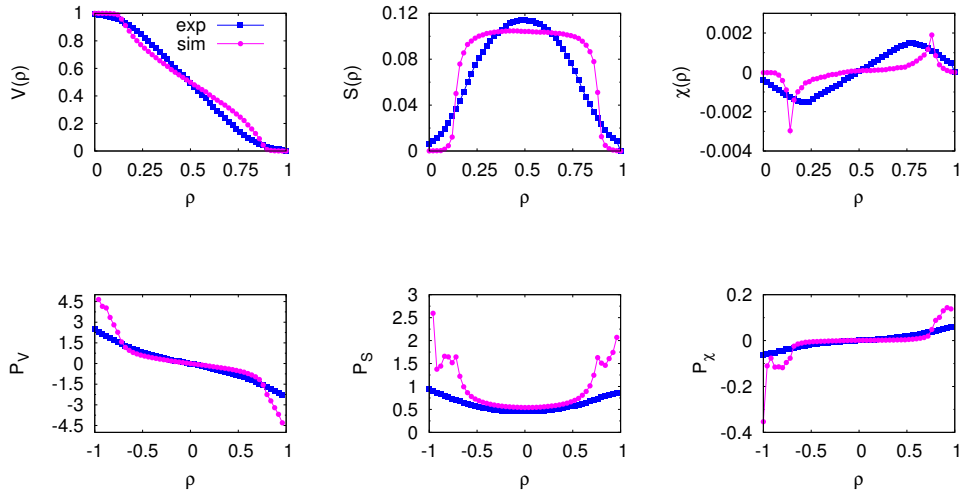


Figure 5.11: Experimental (blue) and numerical (magenta) lamellar pattern from Fig. 5.6 and the numerical pattern from Fig. 5.8 with the corresponding Minkowski functionals and P_V , P_S , P_χ below. A qualitative difference between experimental and numerical pattern is found.

5.4 Local Minkowski functionals of patterns in the CIMA reaction

The effect of local variations in the experimental patterns is analyzed in this section. Neither the hexagonal nor the lamellar patterns show perfectly hexagonal or lamellar symmetry. However while only small grain boundaries occur in the numerical patterns the experimental patterns not only include regions of hexagonal or lamellar symmetry, but also unordered and blurred parts, as well as regions of rhombic or inverted hexagonal symmetry. Indeed the results of this section suggest that the simple quartic polynomial form of the Minkowski functionals from Eqs. (5.4 - 5.6) are crucially influenced by the unordered deviations from the more ordered looking parts.

Local variations are illustrated by analyzing the Minkowski functionals of subsets of the images. Different parts of the experimental hexagonal pattern, i.e. one that appears well-ordered, one with defects and one with rhombic symmetry, are considered in Fig. 5.12. As illustrated the Minkowski functionals of the smaller parts show a different dependency on ρ than for the whole pattern.

The important outcome of this analysis is that the cubic and quartic polynomials defined in Eq. (5.4 - 5.6) are not well approximated by the polynomials defined in Eq. (5.7 - 5.9) while the best fit also shows a qualitative change in its coefficients for the crystalline part of the pattern. Especially the Euler characteristic shows a significant deviation from the fit, when comparing Fig. 5.13 and 5.7.

This indicates that the functional dependence of the Minkowski functionals on ρ is influenced significantly by blurred grain boundaries and defects in the concentration profiles.

The blurred parts of the pattern vanish at different values of the threshold ρ , than the crystalline parts, so that some white domains disappear, when the threshold is increased, instead of gradually decreasing in size and vanishing all at the same threshold. Consequently the Euler characteristic will tend to increase and decrease more gradually than for the case of perfect symmetry, which is illustrated in Fig. 5.12.

The corresponding polynomial fits for P_V , P_S and P_χ are given in Fig. 5.13 with the fit coefficients in Table 5.3.

Table 5.3: Fit coefficients for the polynomial fits in Fig. 5.13.

Pattern type, μ	$P_\mu^{(0)}$	$P_\mu^{(1)}$	$P_\mu^{(2)}$	$P_\mu^{(3)}$	$P_\mu^{(4)}$
Hex. ordered, V	-0.49	-0.68	0.66	-1.38	–
Hex. ordered, S	0.72	0.084	0.068	-0.30	1.00
Hex. ordered, χ	0.041	0.0021	-0.059	0.13	–
Hex. blurred, V	-0.53	-1.31	0.49	-1.89	–
Hex. blurred, S	0.71	0.11	0.66	0.034	0.53
Hex. blurred, χ	0.038	0.063	-0.04	0.087	–

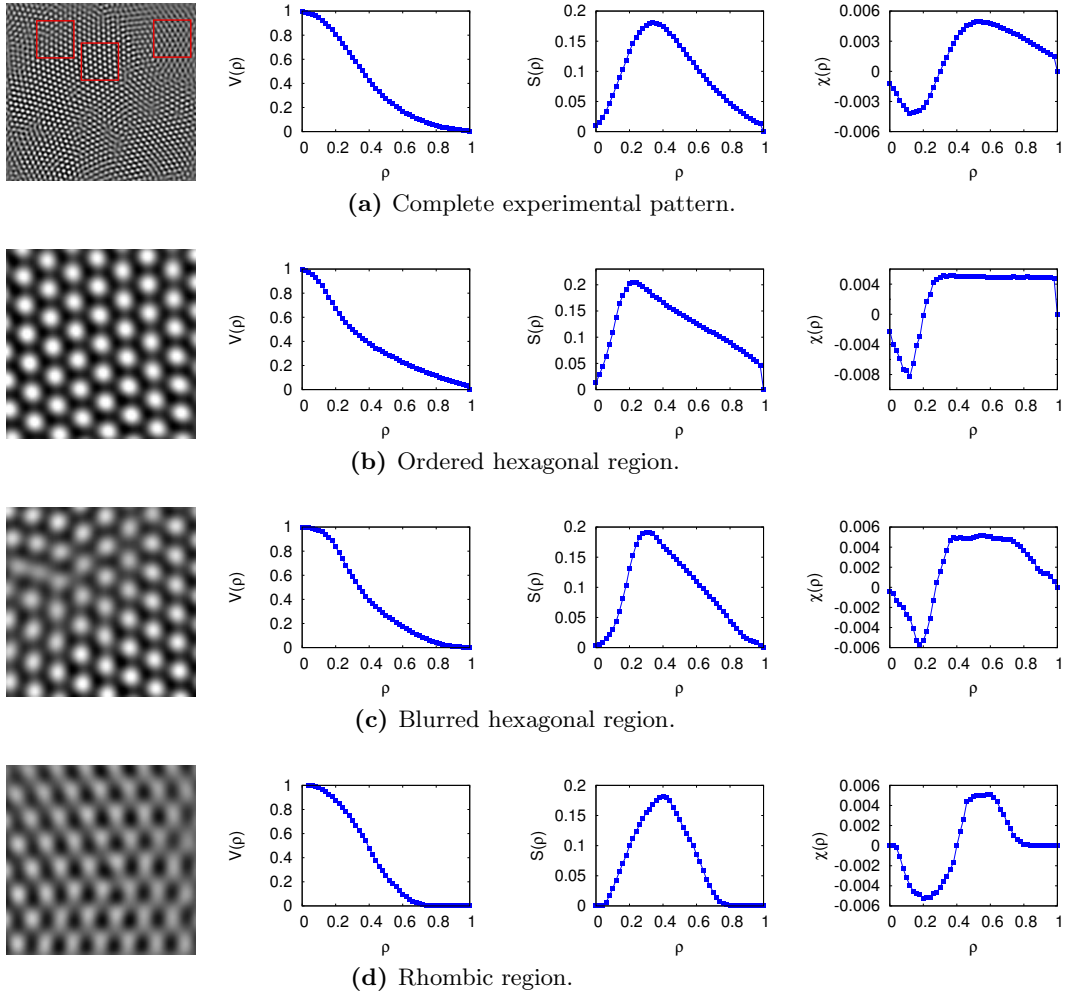


Figure 5.12: The experimental hexagonal pattern from Fig. 5.6 and a well-ordered, blurred and rhombic part of it. The corresponding Minkowski functionals are shown to the right.

For the lamellar case it is not possible to find parts with completely undisturbed lamellar symmetry where blurred grain boundaries vanish at a sufficient size. However parts with less disturbance exist. Fig. 5.14a shows such a part of the experimental lamellar pattern.

Similar to the hexagonal case, when looking at Fig. 5.14b the polynomial fits show a significant deviation from the polynomial fits, when compared to the fits in Fig. 5.7 and a qualitative change in the coefficients can be observed as shown in Table 5.4.

Obviously the difference in numerical and experimental data is related to defects and blurred image parts, which occur in the experimental, but not in the numerical patterns. In fact a good agreement between simulated and experimental patterns

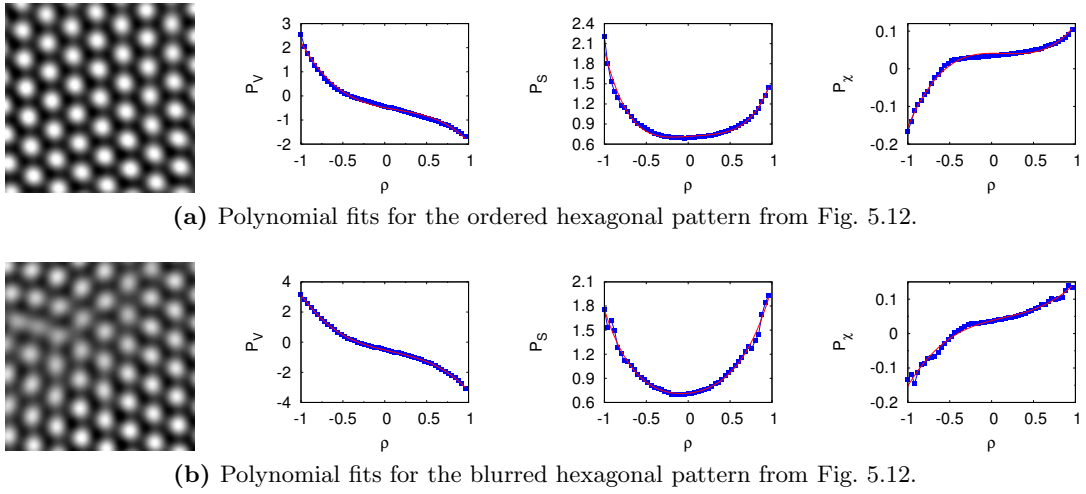


Figure 5.13: P_V , P_S and P_χ for the ordered and blurred hexagonal regions from Fig. 5.12.

Table 5.4: Fit coefficients for the polynomial fits in Fig. 5.14.

Pattern type, μ	$P_\mu^{(0)}$	$P_\mu^{(1)}$	$P_\mu^{(2)}$	$P_\mu^{(3)}$	$P_\mu^{(4)}$
Lam. blurred, V	-0.0042	-0.57	-0.043	-1.41	–
Lam. blurred, S	0.42	0.0084	0.42	0.011	0.20
Lam. blurred, χ	0.00037	-0.013	0.00022	0.076	–

is found when only the more symmetric parts of the experimental patterns are considered. A comparison between two similar hexagonal parts of the numerical and experimental pattern is done in Fig. 5.15, where both patterns and corresponding Minkowski functionals are shown.

Similarly for the lamellar state a smaller part of the experimental pattern is compared to the numerical solution. Both patterns and the resulting Minkowski functionals are shown in Fig. 5.16.

Although a noticeable difference remains for the lamellar pattern, the agreement of numerical and experimental data is much better than for the whole experimental pattern. Nevertheless the characteristic plateau for the hexagonal Euler characteristic and the lamellar perimeter appears in the ordered experimental patterns, as it does in the numerical ones. This results verify that local variations in the experimental patterns can show significant morphological differences. However the local parts in this section have been chosen by obvious visual differences in the patterns' morphology. A full local analysis that takes account of the local effects on the extended experimental patterns is done in the next section via so-called Minkowski-maps.

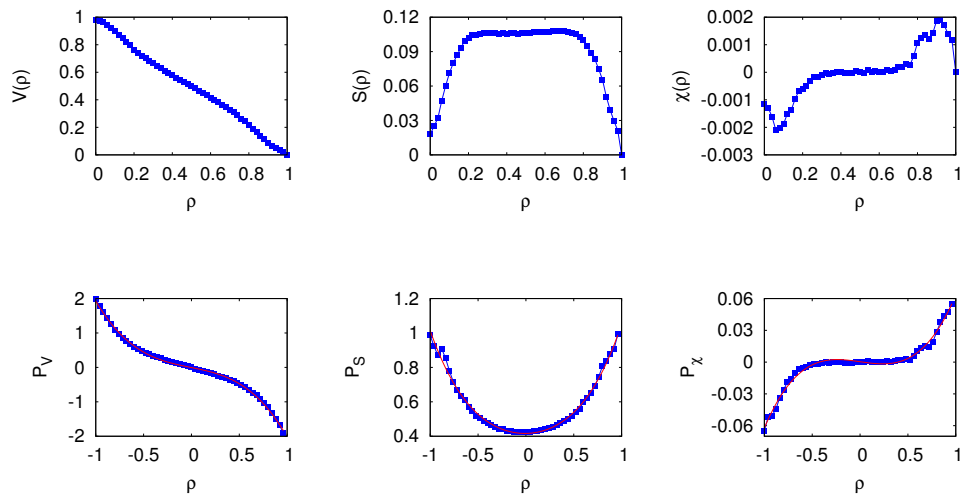
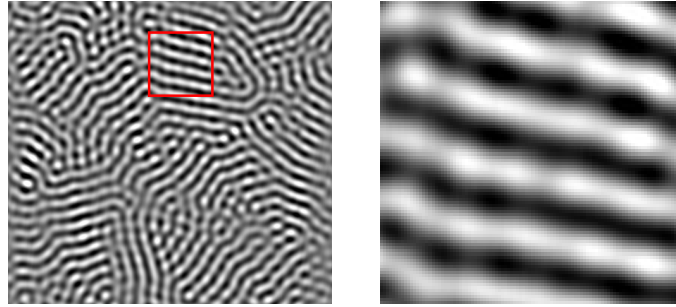


Figure 5.14: A part of the lamellar experimental pattern from Fig. 5.6 with less defects and better lamellar symmetry. The corresponding Minkowski functionals (blue), P_V , P_S , P_χ and polynomial fits (red, solid) are shown below.

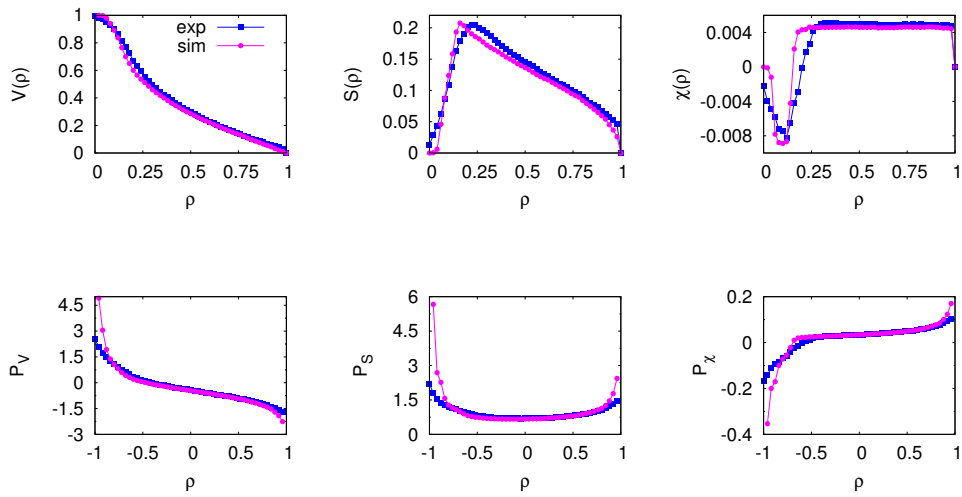
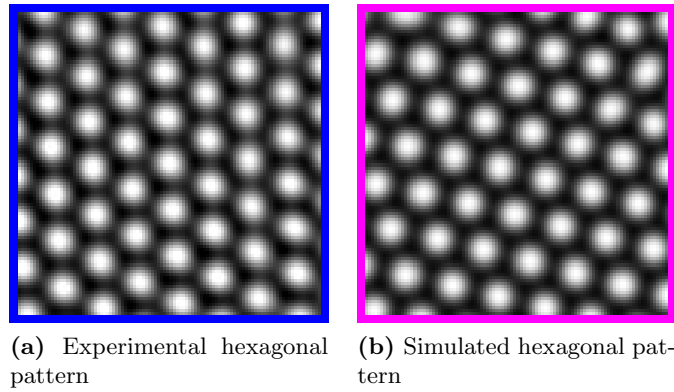
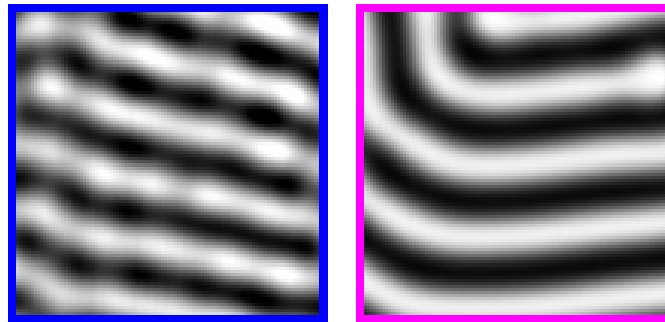


Figure 5.15: Part of the experimental and numerical hexagonal pattern from Fig. 5.6 and Fig. 5.8 with the corresponding Minkowski functionals and P_V , P_S , P_χ below. Good agreement is found for local crystalline parts of the experimental hexagonal pattern, except for the generic behavior for ρ close to zero or unity.



(a) Experimental hexagonal pattern (b) Simulated hexagonal pattern

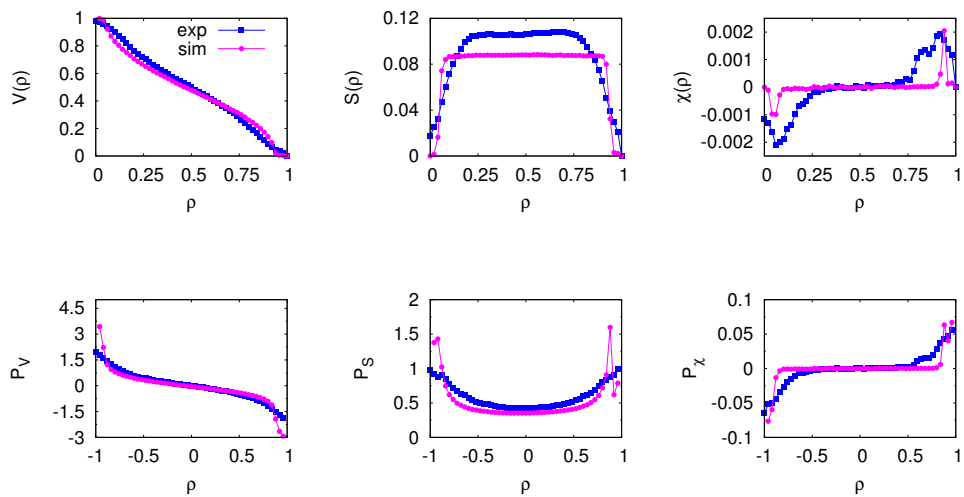


Figure 5.16: Part of the experimental and numerical lamellar pattern from Fig. 5.6 and Fig. 5.8 with the corresponding Minkowski functionals and P_V , P_S , P_χ below. Although noticeable differences persist a better agreement is found for the local lamellar parts.

5.5 Minkowski-maps of patterns in the CIMA reaction

A more systematic approach for quantifying local variations in the experimental concentration profiles is provided by so-called Minkowski maps [51]. A grid of size 5×4 is superposed on the experimental images and the Minkowski functionals are analyzed locally for the domains. Each domain has a size of 100×100 pixels and the grid does not exactly fit the experimental pictures. Consequently the remaining border is cropped from the image. In Fig. 5.17a and 5.18a the concentration profiles from Fig. 5.6 are shown with the superposed grid and truncated borders. Each domain is shown in a different color, which is identical to the color of the graph used for the corresponding Minkowski functionals in Fig. 5.17 and 5.18.

As the Minkowski functionals in Fig. 5.17 and 5.18 indicate, the effects of blurred grain boundaries and unordered regions occurs at smaller length scales in the experimental patterns. The variations in the functional form of the Minkowski functionals are averaged at a larger scale, resulting in the final form of the Minkowski functionals. Obviously only a few domains, in particular, those which appear well-ordered are morphologically similar to the numerical patterns. However a large number of domains shows a different morphology. Some tiles resemble the numerical patterns, some show a similar morphology as the extended pattern and some are reminiscent of the morphology of the rhombic pattern in Fig. 5.12. Those local variations significantly influence the Minkowski functionals for the whole experimental pattern, which would be given by the average of all local Minkowski functionals.

The fact that the unordered parts of the concentration profiles play a significant role for the overall morphology, led to the assumption that patterns could be influenced by superpositions of shifted or rotated patterns, which is the basis of the simple model proposed in chapter 7, as superpositions of ordered patterns would result in unordered parts, where patterns overlap out of phase and ordered structure, where patterns overlap in phase.

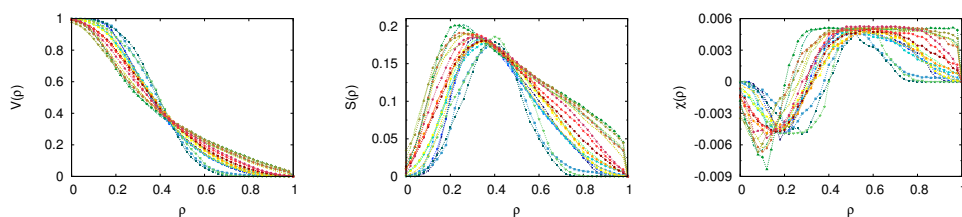
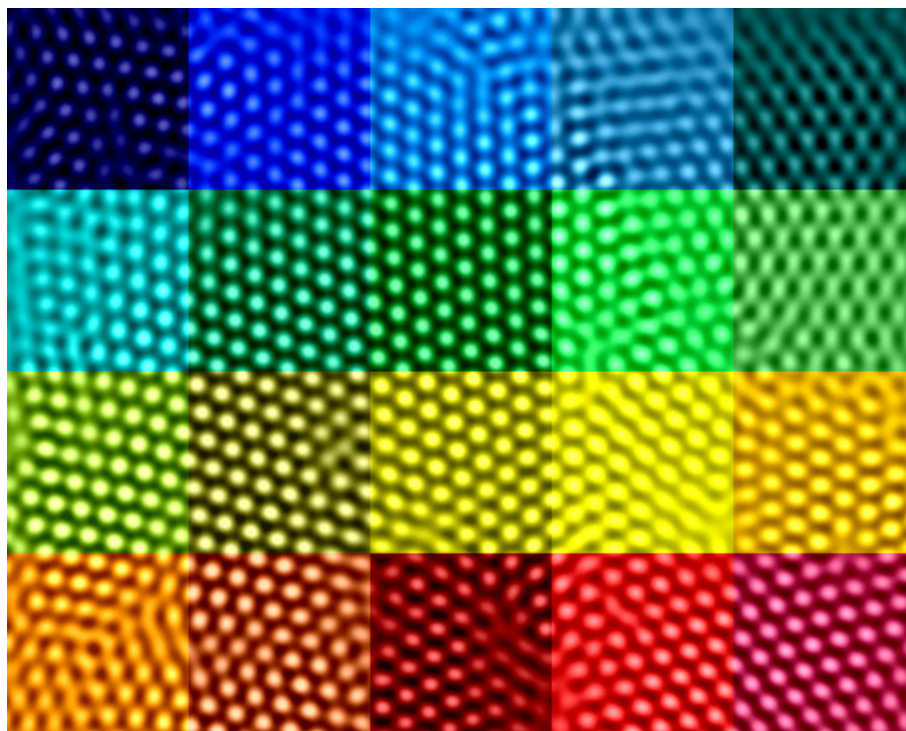


Figure 5.17: Experiment hexagonal pattern from Fig. 5.6 with 5×4 colored tiles. The Minkowski functionals are shown below. Each graph is shown in the same color as the corresponding tile in the pattern.

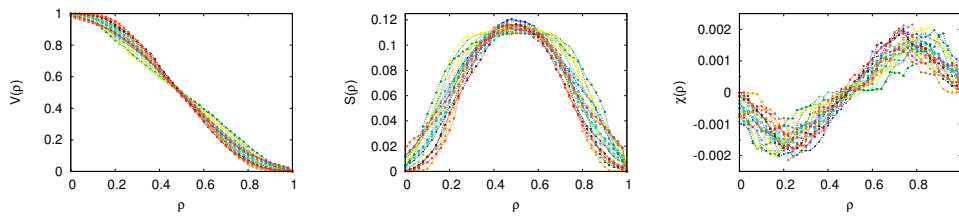


Figure 5.18: Experiment lamellar pattern from Fig. 5.6 with 5×4 colored tiles. The Minkowski functionals are shown below. Each graph is shown in the same color as the corresponding tile in the pattern.

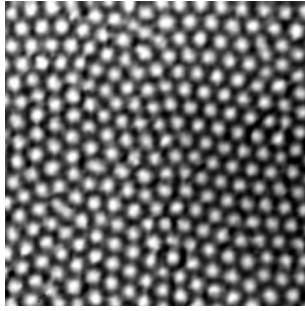
5.6 Minkowski analysis of the CDIMA reaction (De Kepper et al.)

This section analyzes experimental datasets of the CDIMA reaction, i.e. of a different experimental system. It is shown that morphologically the two different experimental techniques reproduce similar results, when compared to the simulated patterns. In the corresponding Ref. [54] Rudovics et al. reported a quantitative comparison of the CDIMA reaction and the LE model. They showed a good agreement with respect to the parameter space and the pattern wavelengths. The CDIMA reaction is well established as the underlying mechanism, which accounts for pattern formation in the CIMA reaction as discussed in chapter 2. A Minkowski analysis shows that patterns from the CDIMA reaction measured in Ref. [54] morphologically agree well with those of the CIMA reaction from Ref. [47]. Fig. 5.19 shows a hexagonal and a lamellar pattern from Ref. [54] and the corresponding Minkowski functionals. P_V , P_S and P_χ as well as the polynomial fits are shown in Fig. 5.20 with the polynomial coefficients in Table 5.5.

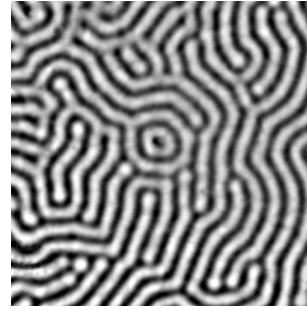
Both the hexagonal and the lamellar pattern appear very ordered. The images cover about 15% of the whole gel disk, so no statement about the morphology of a larger experimental pattern in the CDIMA reaction can be made. The Minkowski functionals appear to be in between those of the whole experimental pattern in the CIMA reaction and its ordered parts. In agreement with Ref. [37] the morphology is well characterized by the polynomial coefficients, as the fit in Fig. 5.20 shows, although a quantitative change in the coefficients when compared to the larger CIMA patterns can be observed and may be the result of the small region the pattern shows, when compared to the CIMA patterns.

Table 5.5: Polynomial fit coefficients found for the numerical patterns from Fig. 5.20 with the corresponding plots.

Pattern type, μ	$P_\mu^{(0)}$	$P_\mu^{(1)}$	$P_\mu^{(2)}$	$P_\mu^{(3)}$	$P_\mu^{(4)}$
Hexagon, V	-0.37	-0.95	0.48	-1.33	–
Hexagon, S	0.35	-0.018	0.15	-0.0071	0.29
Hexagon, χ	0.015	0.019	-0.019	0.041	–
Lamellae, V	0.097	-0.76	-0.14	-1.72	–
Lamellae, S	0.33	-0.026	0.26	-0.054	0.30
Lamellae, χ	0	-0.0028	-0.0020	0.064	–



(a) Experimental hexagonal pattern. Initial concentrations are $[\text{ClO}_2]_0 = 0.6 \text{ mM}$, $[\text{I}_2]_0 = 0.3 \text{ mM}$, $[\text{PVA}]_0 = 10 \text{ g/L}$, $[\text{MA}]_0 = 1.25 \text{ mM}$ and $T = 4.5 \text{ }^\circ\text{C}$. See Fig. 10 in [54]



(b) Experimental lamellar pattern. Initial concentrations are $[\text{ClO}_2]_0 = 0.6 \text{ mM}$, $[\text{PVA}]_0 = 10 \text{ g/L}$, $[\text{MA}]_0 = 1.9 \text{ mM}$ and $T = 4.5 \text{ }^\circ\text{C}$. See Fig. 10 in Ref. [54]

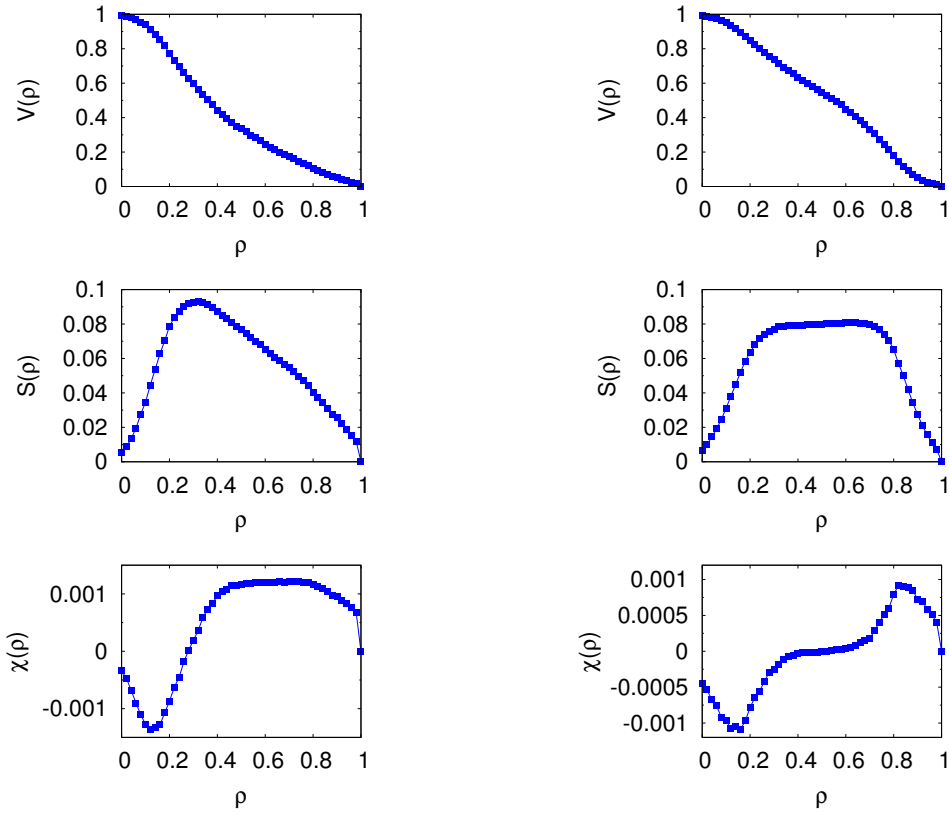
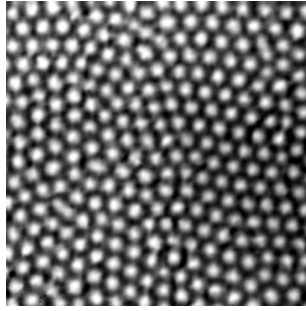
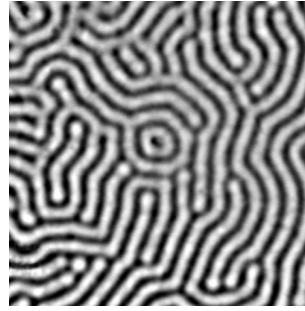


Figure 5.19: Hexagonal and lamellar Turing patterns obtained in the CDIMA-reaction (see Ref. [54]) with corresponding Minkowski functionals shown below each pattern.



(a) Experimental hexagonal pattern. Initial concentrations are $[\text{ClO}_2]_0 = 0.6 \text{ mM}$, $[\text{I}_2]_0 = 0.3 \text{ mM}$, $[\text{PVA}]_0 = 10 \text{ g/L}$, $[\text{MA}]_0 = 1.25 \text{ mM}$ and $T = 4.5 \text{ }^\circ\text{C}$. See Fig. 10 in [54]



(b) Experimental lamellar pattern. Initial concentrations are $[\text{ClO}_2]_0 = 0.6 \text{ mM}$, $[\text{PVA}]_0 = 10 \text{ g/L}$, $[\text{MA}]_0 = 1.9 \text{ mM}$ and $T = 4.5 \text{ }^\circ\text{C}$. See Fig. 10 in Ref. [54]

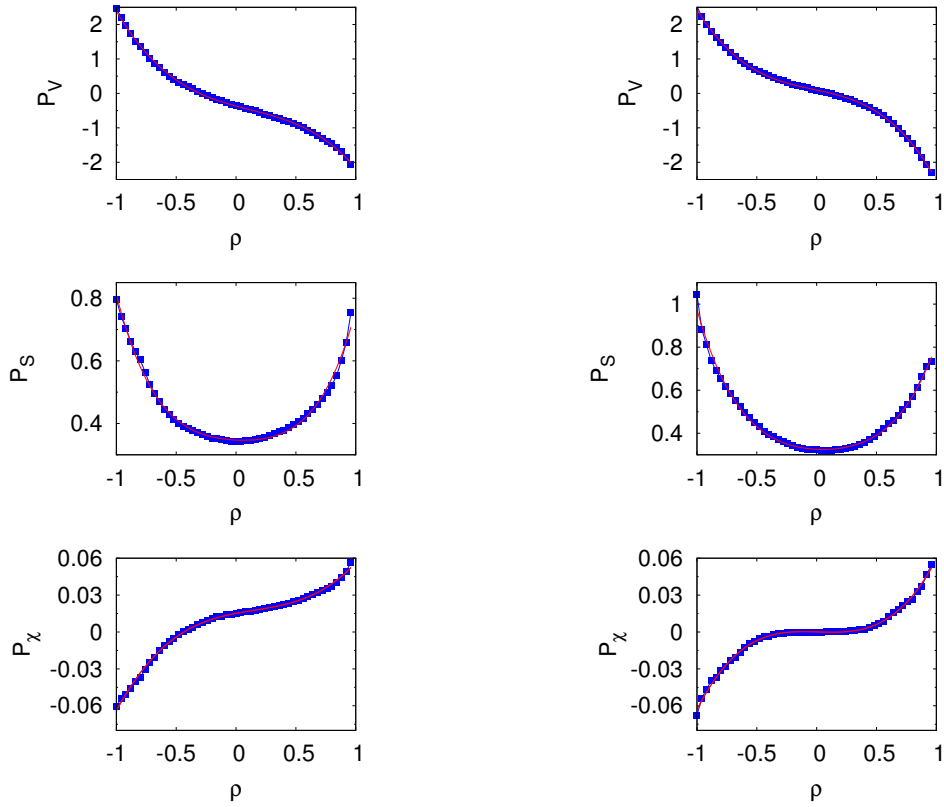


Figure 5.20: Functions defined by Eq. (5.4 - 5.6) (blue) calculated from the Minkowski functionals of the experimental patterns and polynomial fit according to Eq. (5.7), (5.8) and (5.9) (red, solid).

5.7 Minkowski functionals of patterns in other reaction-diffusion models

Stationary hexagonal and lamellar patterns obtained numerically in the Brusselator and Barrio's generic model from section 2.3 are shown in Fig. 5.21 and Fig. 5.22 with the corresponding Minkowski functionals. The numerical parameters $\Delta t = 0.01$ and $\Delta = 1$ are the same as for the numerical solution of the LE model. Patterns in the Brusselator model converge after a similar number of time-steps as for the LE model, i.e. about 50,000. However the generic Brusselator takes longer to converge for the analyzed parameters, i.e. about 300,000 time-steps, which can be attributed to the smaller diffusion coefficient chosen for the numerical solution of the generic model.

No qualitative change in the functional form of the Minkowski functionals can be observed when compared to those obtained in the LE model in section 5.3, i.e. the characteristic plateaus that form for the numerical patterns in the Euler characteristic, which are the result of the well-ordered structure of the patterns, also occur for other reaction-diffusion systems. This also indicates that morphological differences between stationary numerical and experimental patterns do not depend on the exact form of the nonlinear terms in the deterministic reaction-diffusion equation but have a more fundamental reason.

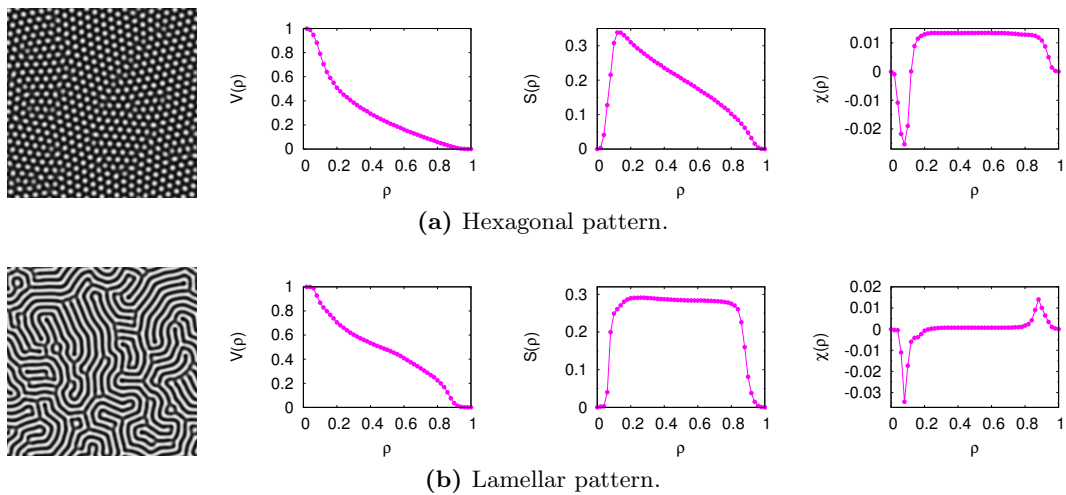


Figure 5.21: Hexagonal and lamellar solution of the Brusselator model for parameters: $D_u = 3$, $D_v = 14$, $a = 4$ and $b = 8.2$ (hex), $b = 10$ (lam). No qualitative morphological difference between numerical patterns in the Brusselator and the LE model is indicated.

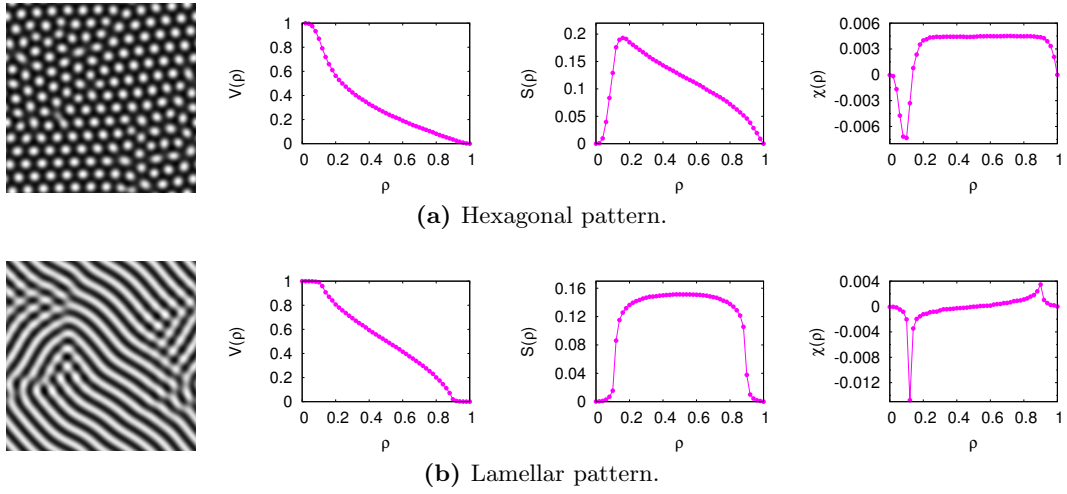


Figure 5.22: Hexagonal and lamellar solution of the generic model from Eq. (2.34) and Eq. (2.35) for $D = 0.516$, $\delta = 2$, $\alpha = 0.899$, $\beta = 0.91$, $r_1 = 3.5$ and $r_2 = 0.6$ (hex), $r_2 = 0$ (lam). No qualitative morphological difference between numerical patterns in the generic Brusselator and the LE model is indicated.

Chapter 6

Influence of additive noise on pattern formation in the LE model

Numerical analysis of the LE model with additive noise shows that patterns are very robust against noise for all states. However the maximum noise intensity until a pattern breaks down depends on the state. While hexagons are less robust, inverted hexagonal patterns are more stable. Although additive noise influences the pattern formation depending on the intensity, a Minkowski analysis shows that morphological differences of experimental and numerical patterns persist even for strong noise.

6.1 Influence on pattern stability

The effect of Gaussian white noise on Turing pattern formation has been studied for 2D and 3D systems in Ref. [33] and Ref. [31] using the generic Brusselator model for the reaction kinetics with nonlinear coupling terms up to third order from section 2.3, as introduced in Ref. [6].

Therein pattern formation is shown to be extremely robust against noise. Here we perform a similar analysis for 2D patterns in the LE model with additive noise. The corresponding stochastic partial differential equation (SPDE) is given by

$$\frac{\partial u}{\partial t} = \nabla^2 u + a - u - 4 \frac{u v}{1 + u^2} + \zeta_u \xi_u(\mathbf{r}, t), \quad (6.1)$$

$$\frac{\partial v}{\partial t} = \sigma \left[c \nabla^2 v + b \left(u - \frac{u v}{1 + u^2} \right) \right] + \zeta_v \xi_v(\mathbf{r}, t), \quad (6.2)$$

and solved via the explicit FTCS scheme with additive noise as described in section 3.5.

In agreement with Ref. [33] the inverted hexagonal pattern, which corresponds to a hexagonal pattern in their convention, can sustain larger noise values, than the lamellar and hexagonal patterns.

Fig. 6.1 shows representative patterns of each state with increasing noise strength ζ .

Comparing the noise strength ζ with the signal strength, i.e. the range of concentrations ΔI in the concentration profiles of Fig. 6.1 without noise, in agreement with

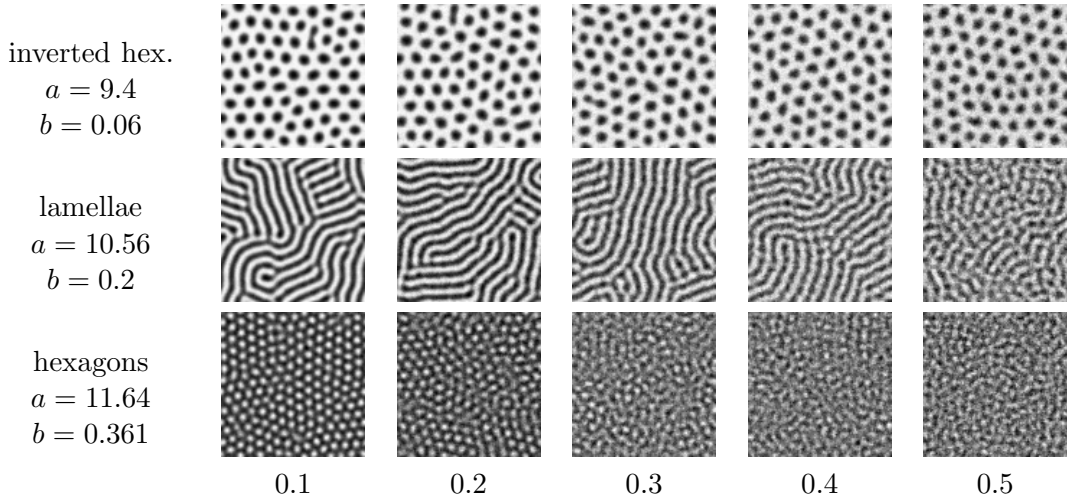


Figure 6.1: Series of patterns in the hexagonal, lamellar and inverted hexagonal state with increasing noise strength ζ .

Ref. [31], pattern formation turns out to be stable for $\zeta/\Delta I \sim 0.13$ (hexagonal) to ~ 0.24 (inverted hexagonal).

6.2 Influence on convergence

Not only the pattern stability but also the convergence rate is affected by the presence of white noise. As reported in Ref. [31] there is the decrease of time-steps until the system shows a stable structure for weak noise, which facilitates to overcome metastable states during time evolution [31]. This is also found for the hexagonal pattern in the LE model from Fig. 6.2.

The curves are characterized by a constant absolute change in the concentrations from about 10,000 time-steps. This can be attributed to the additive noise term and remains constantly at about 0.08, i.e. of the same order as the noise intensity ζ .

6.3 Influence of noise on pattern morphology

In this section numerical patterns with white noise are compared to experimental patterns for the hexagonal and lamellar case. Strong noise, which can hardly be justified physically, improves the agreement of numerical and experimental data, but significant differences persist.

Hexagonal and lamellar patterns with a noise strength of $\zeta = 0.2$, where the hexagonal patterns are barely stable, are compared with the experimental patterns. Fig. 6.3 shows the corresponding patterns and Minkowski functionals.

While the agreement of noisy numerical and experimental hexagonal pattern slight improves qualitatively, there is still a strong deviation, particularly for the lamellar

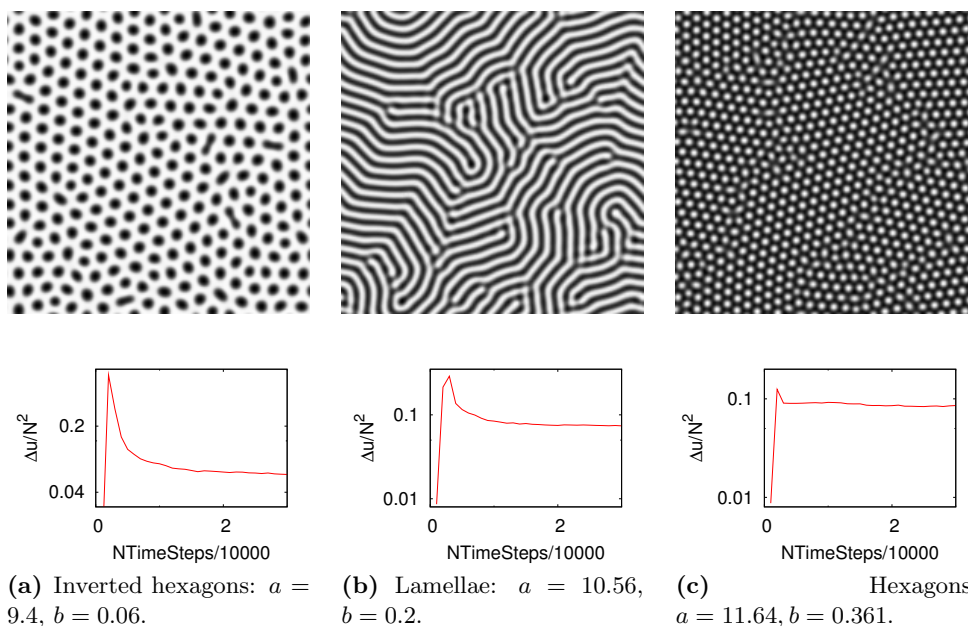


Figure 6.2: Convergence of LE patterns influenced by noise of strength $\zeta = 0.1$. Common parameters are $\sigma = 20$ and $c = 1$. The hexagonal state converges faster, as the noise facilitates to overcome a metastable transient state of the deterministic solution.

state. For a noise strength of $\zeta = 0.5$, i.e. $\zeta/\Delta I = 0.24$, where the hexagonal pattern breaks down, the morphological agreement of noisy numerical and experimental lamellar pattern improves, as shown in Fig. 6.4

However a slightly better qualitative agreement for very noisy patterns led to the assumption that a different statistical process might influence the experimental patterns. While the additive Gaussian noise itself has a nearly scale invariant spectrum, the turbulent patterns obviously are not scale invariant. A simple statistical model would therefore have to preserve a characteristic length scale. Such a model is proposed in chapter 7 based on random superposition of basic patterns, which brings together the results of this chapter and the influence of local variations discussed in chapter 5.

Nevertheless even a noise strength of about 0.2, which corresponds to $\zeta/\Delta I = 0.13$ for the hexagonal pattern can hardly be justified by thermal fluctuations in the experiment and the results show that the difference between experimental and numerical patterns persist under additive noise. Consequently additive Gaussian white noise cannot explain the differences between numerical and experimental patterns.

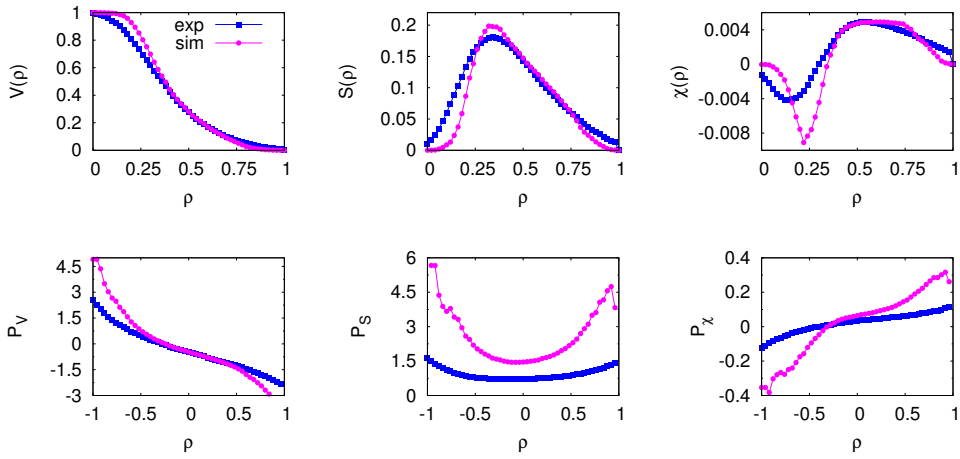
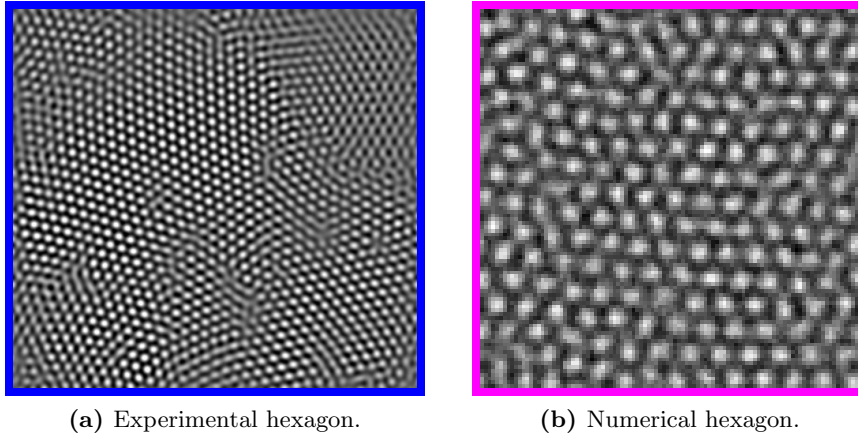


Figure 6.3a: Comparison of hexagonal experimental (blue) and noisy simulated pattern (magenta) with a noise intensity of $\zeta = 0.2$ and $a = 11.64$, $b = 0.361$. Differences between numerical and experimental patterns persist.

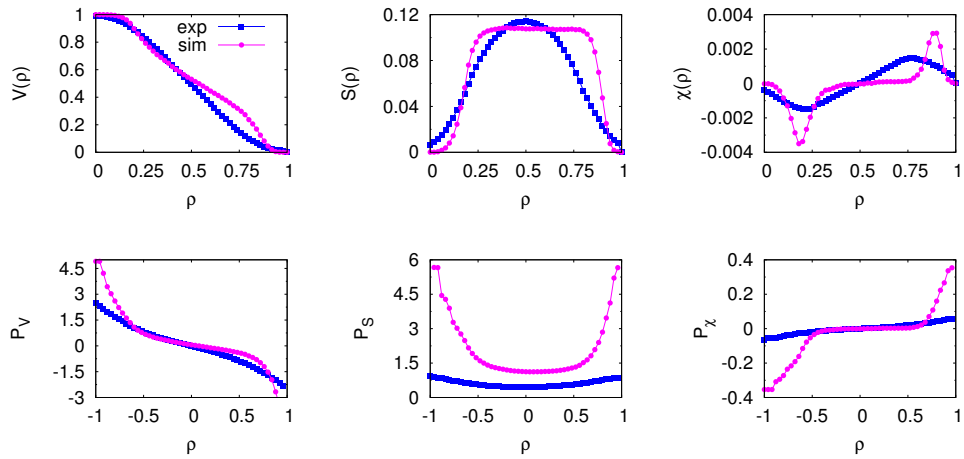
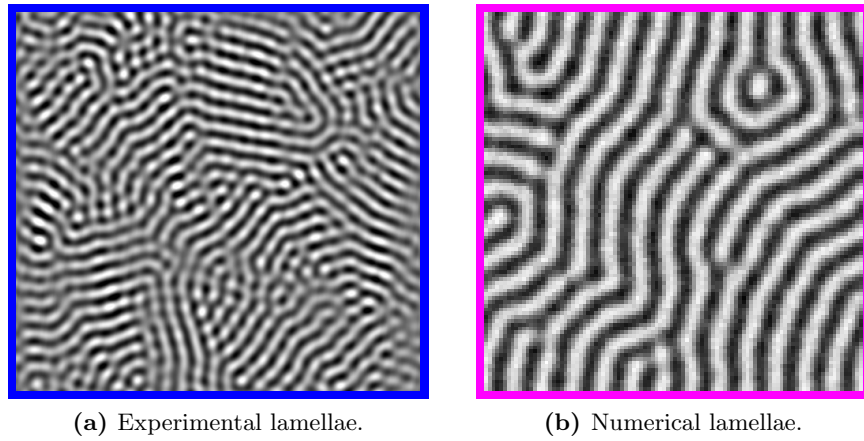
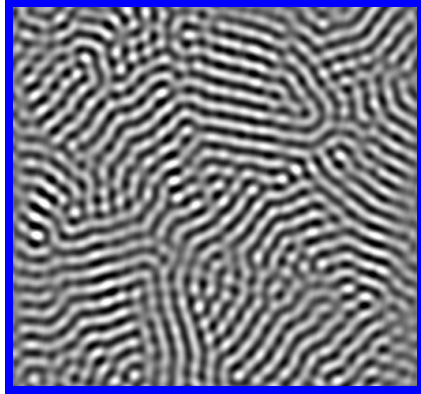
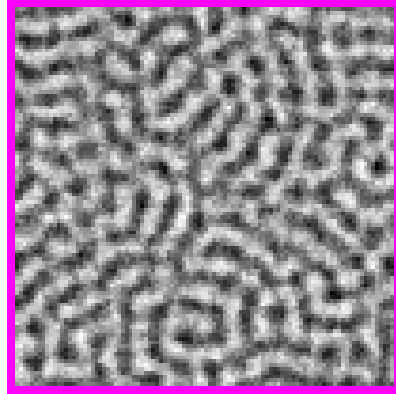


Figure 6.3b: Comparison of the lamellar experimental (blue) and the noisy simulated pattern (magenta) with a noise intensity of $\zeta = 0.2$ and $a = 10.56$, $b = 0.2$. Differences between numerical and experimental patterns persist.



(a) Experimental lamellae.



(b) Numerical lamellae.

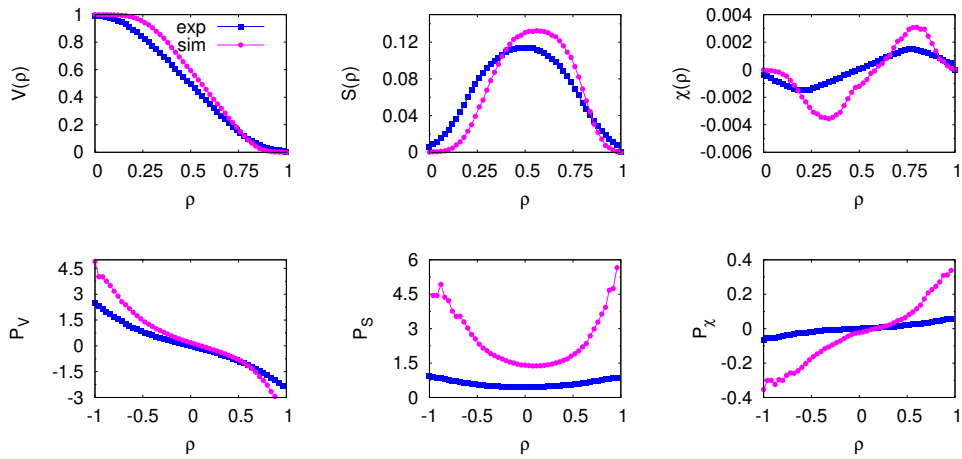


Figure 6.4: Comparison of the lamellar experimental (blue) and the noisy simulated pattern (magenta) with a noise intensity of $\zeta = 0.5$ and $a = 10.56$, $b = 0.2$. Although a better qualitative agreement is indicated, the morphological differences persist even for strong noise.

Chapter 7

Statistical ensemble of superposed basic patterns

A simple model for pattern formation based on statistical superposition of basic patterns is proposed that quantitatively reproduces the morphology of the experimental patterns. The model involves M randomly rotated copies of the same pattern that are superposed with the original pattern using an adjustable amplitude A . In addition to reproducing the morphology of the experimental hexagonal and lamellar patterns, this model also suggests, for the first time, an explanation of the turbulent phase, experimentally observed in Ref. [47], as a dynamically fluctuating superposition of the basic patterns.

7.1 A simple model with superposition of patterns

As the local Minkowski analysis of chapter 5 indicates the differences between numerical and experimental patterns can be attributed to unordered regions in the experimental concentration profiles. Those defects are characterized by the loss or the distortion of the local hexagonal or lamellar symmetry. A phenomenological explanation can be given by a superposition of basic numerical patterns. The superposition of differently orientated patterns leads to unordered parts, where the patterns overlap out of phase, similar to those observed in the experiment. Therefore a numerical pattern, i.e. a greyscale image of size $N \times N$ that represents a stationary numerical intensity profile of the deterministic reaction-diffusion equations is obtained and rotated M times with random angles α_i with $1 \leq i \leq M$. Then a square of size $N/\sqrt{2} \times N/\sqrt{2}$ is cut from the middle of each rotated and the original pattern as shown in Fig. 7.1. The resulting patterns u_0, u_1, \dots, u_M are superposed by

$$u_{\text{sp}} = u_0 + A \cdot \sum_{i=1}^M u_i \quad \text{where } A \in [0, 1], \quad (7.1)$$

where A gives the amplitude of the superposed rotated patterns. The pattern u_0 , with fixed amplitude 1, gives a preferential direction in the superposition. The M rotated and superposed patterns give a turbulent background without any preferential direction, while the intensity of this background is adjusted by the amplitude A .

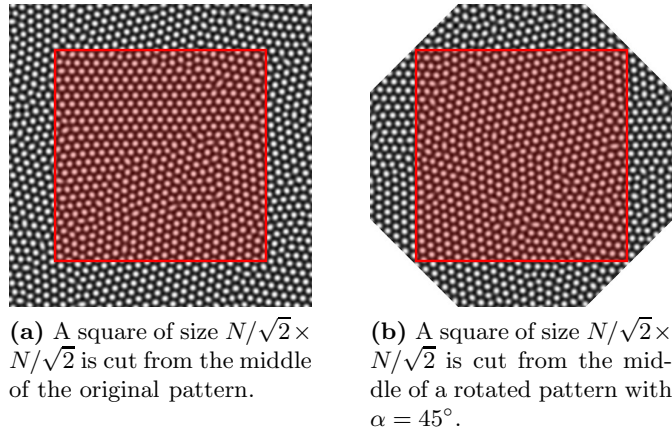


Figure 7.1: The numerical patterns of size $N \times N$ are rotated with random angles α_i and a square of size $N/\sqrt{2} \times N/\sqrt{2}$ is cut from the middle of each pattern.

Depending on A the morphology of u_{sp} changes significantly. To illustrate this dependence, a sequence of superpositions with increasing amplitude is shown in Fig. 7.2.

Consider a random superposition of patterns with $A = 1$, i.e. without a preferential direction in the superposed patterns and the morphology determined by the turbulent background. The resulting pattern u_{sp} loses its hexagonal or lamellar symmetry and morphologically resembles the snapshots of turbulent patterns in the CIMA reaction, which is indicated in Fig. 7.2 and shown in section 7.2.3.

Choosing an amplitude A below unity corresponds to a symmetry breaking. As mentioned above, u_0 gives a preferential direction for the resulting system, because it has a larger relative intensity in the superposition described by Eq. (7.1). However for large numbers of M no morphological change in the patterns is visible above a certain threshold, because the overall intensity of the turbulent background becomes larger the more patterns are included in the sum. For example in Fig. 7.2 no qualitative morphological difference can be observed between the pattern for $A = 0.5$ and the pattern for $A = 1$. For a decreasing amplitude the superpositions show more and more crystalline regions. For small A the morphology is mainly determined by u_0 and only a few blurred regions remain.

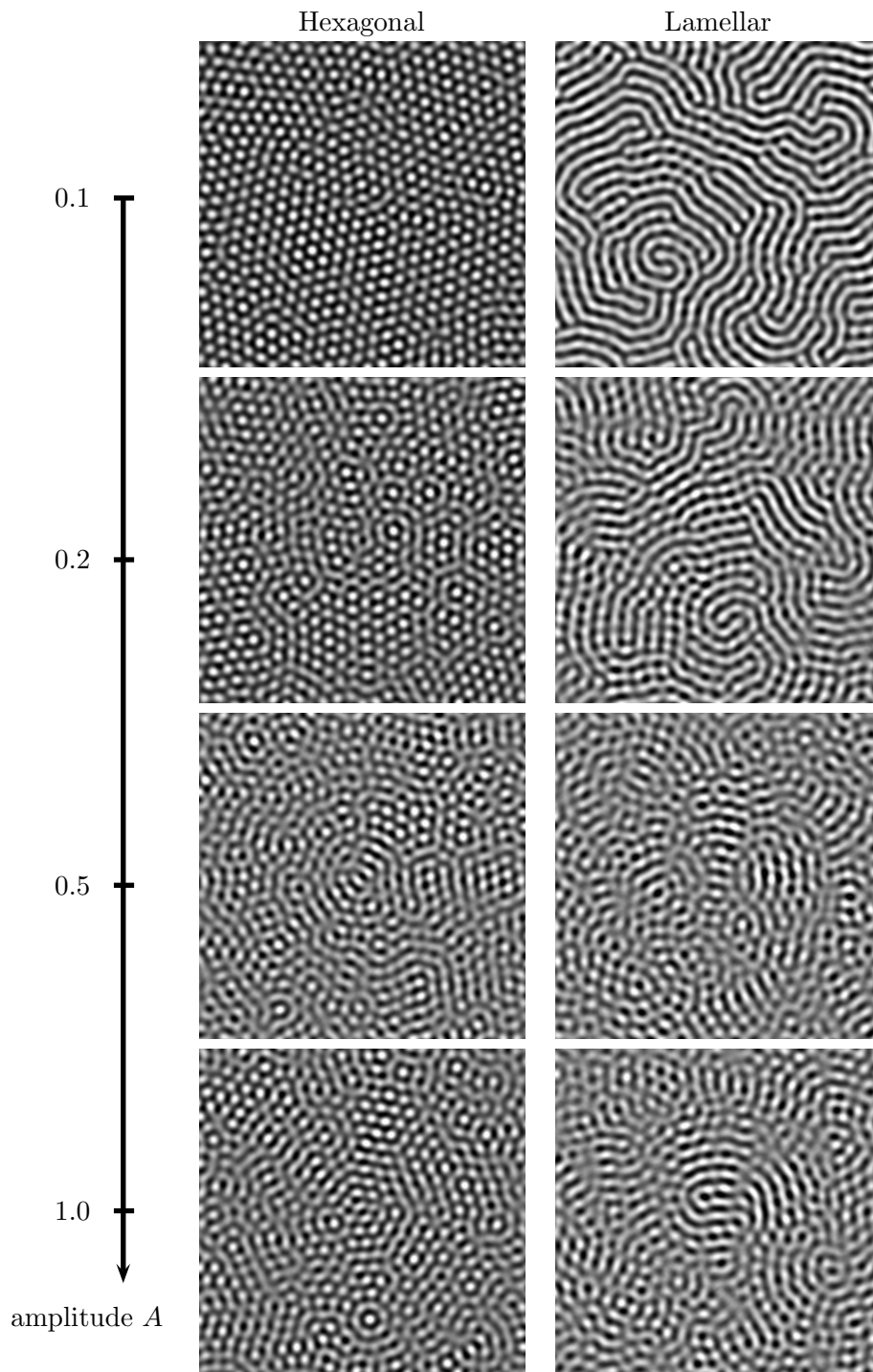


Figure 7.2: A sequence of superposed numerical hexagonal and lamellar patterns for increasing amplitudes $A = 0.1, 0.2, 0.5, 1.0$.

7.2 Minkowski analysis for superposed patterns

Minkowski functionals are calculated for superposed numerical patterns and compared to the experimental patterns. Depending on the amplitude A the superposed images show an almost perfect morphological agreement with the experimental patterns for the hexagonal and lamellar state. Additionally the morphology of turbulent patterns can be reproduced by superpositions with large amplitude.

7.2.1 Hexagonal state

A series of $A = 0.1, 0.2, 0.3, 0.4, 0.5$ with $M = 12$ has been generated and analyzed via Minkowski functionals. M has been chosen with respect to the occurring transition to the turbulent state for a large amplitude, i.e. $A = 0.5$, which can only be found in our analysis if a sufficient number of patterns are superposed. However $M = 12$ is only a rough estimate here, as no rigorous analysis of the dependence on the number of superposed patterns has been done yet. As shown in Fig. 7.3, for $A = 0.2$ very good agreement of the Minkowski functionals between experimental and numerical data is found for the hexagonal patterns.

Excellent agreement is also found for P_V , P_S and P_χ . The fit coefficients for the superpositions are given in Table 7.1 with the experimental values in parenthesis. As the coefficients show, the qualitative form of P_V , P_S and P_χ is reproduced by the superposed numerical patterns. Intuitively the randomly superposed patterns introduce the unordered and blurred parts to the image that can be locally observed for the experimental patterns. The slow movement of the grain boundaries and unordered parts, reported in Ref. [47], is another indication that a superposed background is observed in the experiment.

As only rotations of one basic pattern with a fixed amplitude are considered in the superposition, the model is of course a great simplification. This may account for the fact that while in the numerical pattern unordered parts are distributed over the whole pattern, large crystalline regions that appear ordered, cannot be seen. An extended numerical model could include translations and different amplitude distributions for the superposed patterns.

Table 7.1: The fit coefficients for superposed numerical hexagonal patterns from Fig. 7.3. Experimental values are shown in parenthesis.

Type, μ	$P_\mu^{(0)}$	$P_\mu^{(1)}$	$P_\mu^{(2)}$	$P_\mu^{(3)}$	$P_\mu^{(4)}$
Hexagons, V	-0.38 _(-0.50)	-1.44 _(-1.46)	0.31 _(0.46)	-1.10 _(-1.00)	–
Hexagons, S	0.69 _(0.72)	0.13 _(0.15)	0.49 _(0.31)	-0.17 _(-0.20)	0.25 _(0.54)
Hexagons, χ	0.026 _(0.033)	0.067 _(0.058)	-0.027 _(-0.034)	0.047 _(0.059)	–

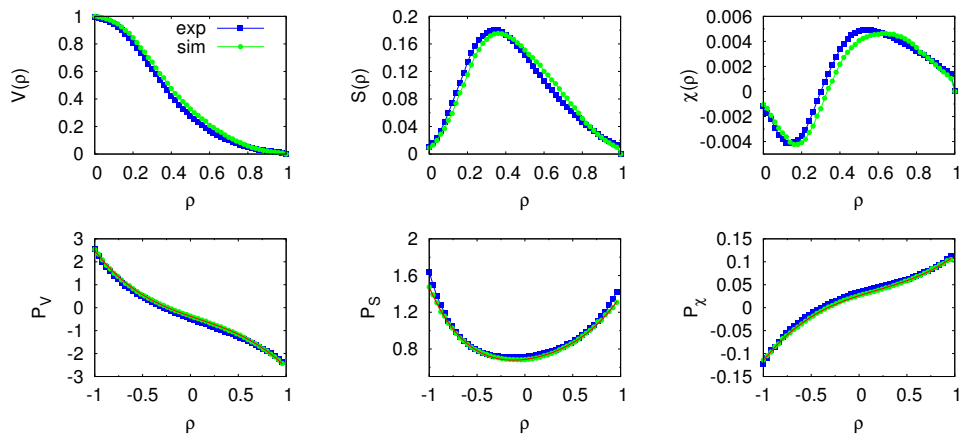
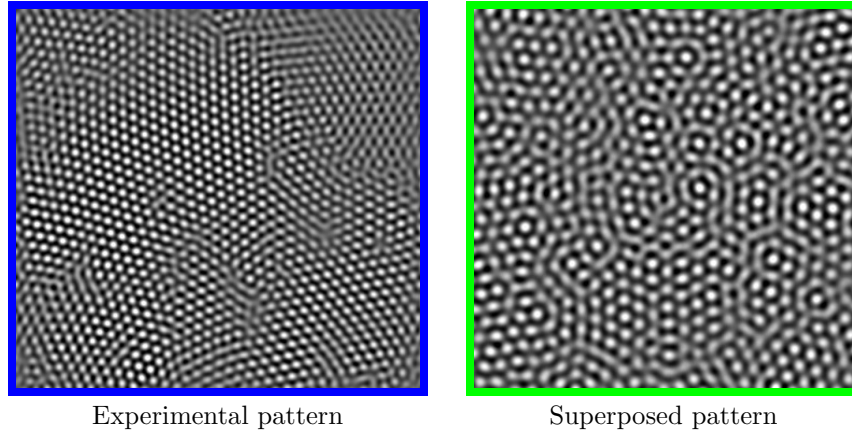


Figure 7.3: Superposed numerical hexagonal pattern (green) for $A = 0.2$ with simulation parameters $\sigma = 20$, $c = 1$, $a = 12$, $b = 0.37$, compared with the experimental hexagonal pattern (blue) from Fig. 5.7. Excellent agreement is found for the Minkowski functionals and P_V , P_S and P_χ , which are shown with the corresponding fits for the numerical pattern (red, solid).

Table 7.2: The fit coefficients for superposed numerical lamellar patterns from Fig. 7.4. Experimental values are shown in parenthesis.

Type, μ	$P_\mu^{(0)}$	$P_\mu^{(1)}$	$P_\mu^{(2)}$	$P_\mu^{(3)}$	$P_\mu^{(4)}$
Lamellar, V	-0.026 _(-0.021)	-1.39 _(-1.42)	-0.023 _(0.011)	-1.12 _(-1.08)	–
Lamellar, S	0.45 _(0.45)	0.028 _(0.017)	0.43 _(0.48)	-0.013 _(-0.034)	0.064 _(-0.006)
Lamellar, χ	0.0004 _(0.0006)	0.037 _(0.030)	0.0005 _(-0.0004)	0.038 _(0.035)	–

7.2.2 Lamellar state

Similar to the hexagonal case a series of superpositions for $A = 0.1, 0.2, 0.3, 0.4, 0.5$ with $M = 12$ has been analyzed. Again for $A = 0.2$ superposed and experimental lamellar pattern agree morphologically, as shown in Fig. 7.3, where the patterns and the corresponding Minkowski functionals, as well as P_V , P_S and P_χ are shown.

A good agreement is also found for P_V , P_S and P_χ . However a small difference in the Euler characteristic is still visible. A more detailed search for an amplitude of best agreement might take account of this difference. The fit coefficients for the superpositions are given in Table 7.2 with the experimental values in parenthesis. Their qualitative form is reproduced by the superposed numerical patterns. For the lamellar patterns, no larger crystalline regions appear in the experimental patterns. Consequently the patterns are well described by the simple model, which also indicates that the experimental lamellar patterns were influenced by a stronger turbulent background superposition than the hexagonal patterns.

7.2.3 Turbulent state

For a large amplitude A the sum of the randomly rotated patterns dominates the resulting patterns. For the considered superposition of the same basic hexagonal and lamellar patterns from section 7.2.1 and 7.2.2, an amplitude of $A = 0.5$ yields an excellent morphological agreement of superposed hexagonal and lamellar patterns and the experimental snapshots of turbulent structures, as shown in Fig. 7.5. The corresponding fit coefficients for P_V , P_S and P_χ are given in Table 7.3. In both cases the functional form is qualitatively reproduced, i.e. the leading fit coefficients only show minor differences of less than 12%, which is of the same order than the deviations between different experimental patterns. This agreement does not depend on the initial symmetry of the superposed patterns. Both, lamellar and hexagonal superposition reproduce a turbulent state, however a larger number of superposed hexagonal patterns was often needed in the numerical calculations. 12 patterns were required for the hexagonal superposition but a smaller number of patterns can be sufficient in the lamellar case. This indicates that a full physical model of the superposition should include a superposition of basic patterns of all states.

In this model no dynamics are explicitly considered, which results in stationary images that share the morphology of the turbulent snapshots, but not the temporal behavior. To include these dynamics, the superposition of the patterns would have to include dynamically fluctuating orientations, while the distribution of amplitudes among the patterns remains constant.

Table 7.3: Fit coefficients for the numerical superpositions of hexagonal (hex) and lamellar (lam) patterns from Fig. 7.5. Experimental values are shown in parenthesis.

Type, μ	$P_\mu^{(0)}$	$P_\mu^{(1)}$	$P_\mu^{(2)}$	$P_\mu^{(3)}$	$P_\mu^{(4)}$
Turb.(hex), V	-0.17 _(-0.092)	-1.87 _(-1.85)	0.11 _(0.09)	-0.67 _(-0.66)	—
Turb.(hex), S	0.48 _(0.49)	0.063 _(0.025)	0.39 _(0.44)	-0.10 _(-0.043)	0.036 _(-0.018)
Turb.(hex), χ	0.0074 _(0.0038)	0.064 _(0.061)	-0.008 _(-0.003)	0.0065 _(0.0091)	—
Turb.(lam), V	-0.029 _(-0.063)	-1.89 _(-2.08)	0.033 _(0.054)	-0.67 _(-0.45)	—
Turb.(lam), S	0.58 _(0.59)	0.0045 _(0.024)	0.51 _(0.55)	0.010 _(-0.060)	0.0025 _(-0.12)
Turb.(lam), χ	0.0010 _(0.0028)	0.075 _(0.085)	-0.001 _(-0.004)	0.0085 _(-0.0065)	—

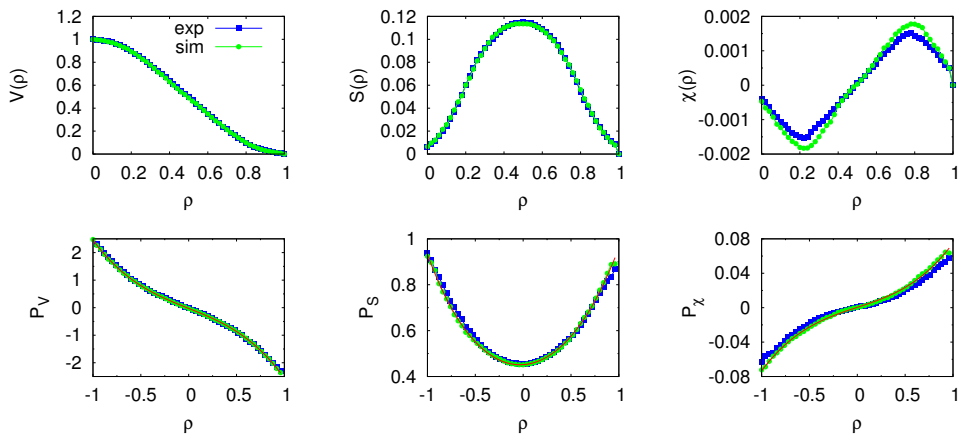
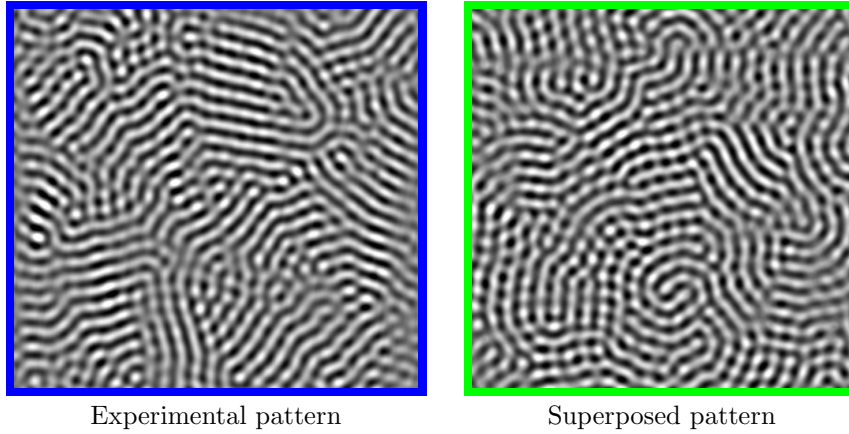


Figure 7.4: Superposed numerical lamellar pattern (green) for $A = 0.2$ with simulation parameters $\sigma = 20$, $c = 1$, $a = 12.2$, $b = 0.3$ compared with the experimental lamellar pattern (blue) from Fig. 5.7. Excellent agreement is found for the Minkowski functionals and P_V , P_S and P_χ , which are shown with the corresponding fits for the numerical pattern (red, solid).

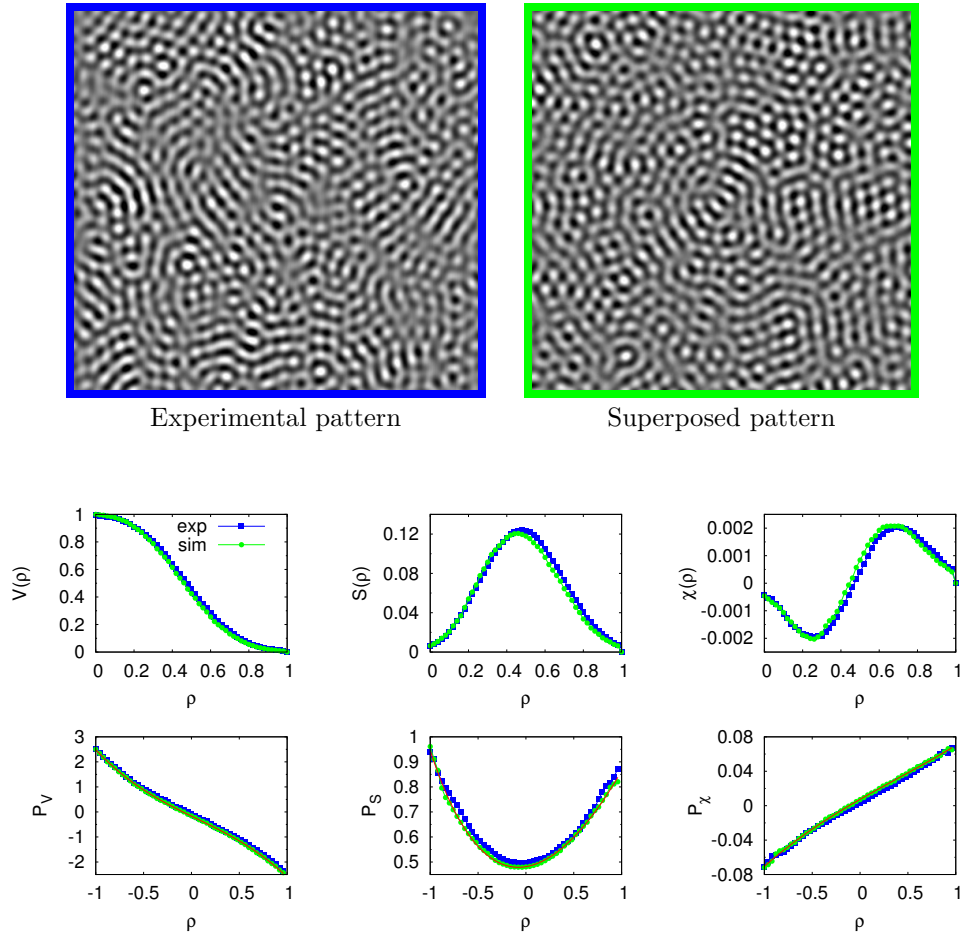


Figure 7.5a: Superposition of hexagonal patterns (green) with $A = 0.5$ with simulation parameters $\sigma = 20$, $c = 1$, $a = 12$, $b = 0.37$, compared to a snapshot of a turbulent experimental state (blue). The Minkowski functionals and P_V , P_S and P_χ are shown below, with the corresponding fits for the numerical pattern (red, solid).

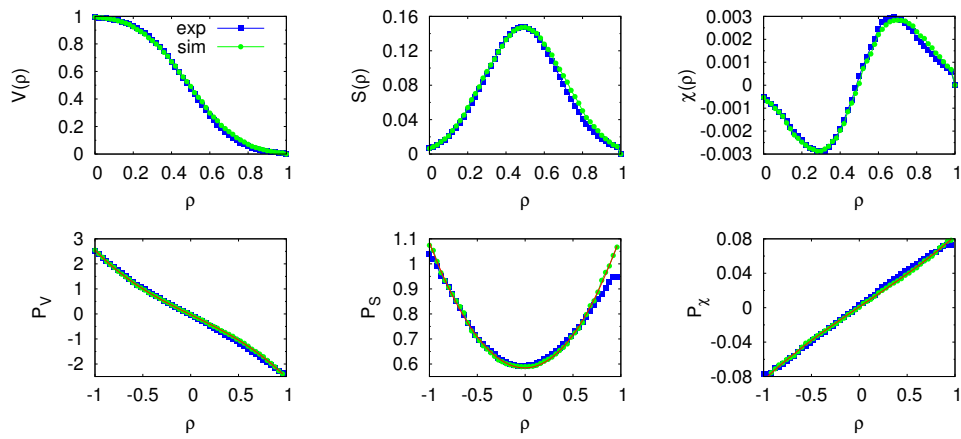
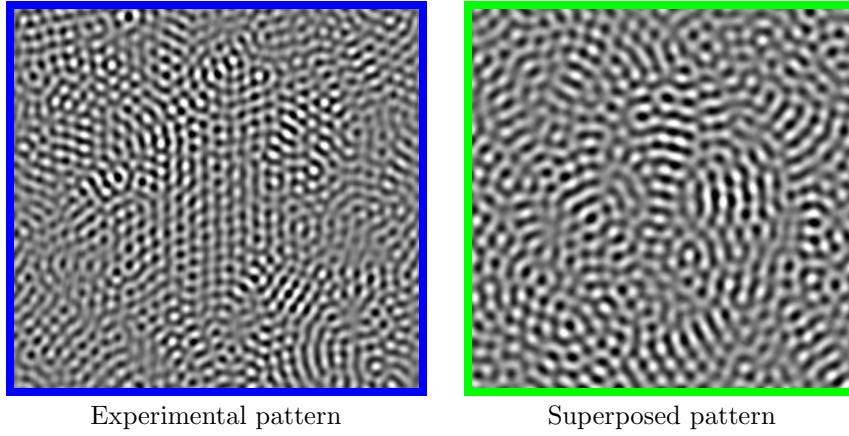


Figure 7.5b: Superposition of lamellar patterns (green) with $A = 0.5$ with simulation parameters $\sigma = 20$, $c = 1$, $a = 12.2$, $b = 0.3$, compared to a snapshot of a turbulent experimental state (blue). The Minkowski functionals and P_V , P_S and P_χ are shown below, with the corresponding fits for the numerical pattern (red, solid).

7.3 Interacting pattern gas

In this section the superposition of patterns is characterized physically by a measure for the interaction energy between patterns.

7.3.1 Derivation of the interaction energy

The fields u, v are written as a vector \mathbf{u} with $u_1 = u$ and $u_2 = v$. To obtain the relaxation dynamics for \mathbf{u} a variational ansatz is used:

$$\frac{\partial \mathbf{u}}{\partial t} = -\Gamma \frac{\delta F[\mathbf{u}]}{\delta \mathbf{u}} \quad (7.2)$$

with the “Free-Energy-Functional” (Lyapunov functional):

$$F[\mathbf{u}] = \int_V d\mathbf{r} \left(\frac{1}{2} \sum_{i,j} D_{ij} \nabla u_i \nabla u_j + f(\mathbf{u}) \right) \quad (7.3)$$

where the diffusion coefficients are written as

$$D_{ij} = D_i \delta_{ij}. \quad (7.4)$$

The stationary solutions are then given by

$$\frac{\delta F[\mathbf{u}]}{\delta \mathbf{u}} \stackrel{!}{=} 0 = D_i \nabla^2 u_i - \frac{\partial f(\mathbf{u})}{\partial u_i}. \quad (7.5)$$

To find the energy of interacting patterns let us consider a superposition of N stationary solutions:

$$\underline{\mathbf{u}} := \frac{1}{N} \sum_{\nu=1}^N \mathbf{u}^{(\nu)}. \quad (7.6)$$

The interaction energy is given by the difference in the free energy of the basic and the superposed patterns:

$$\Delta F := F[\underline{\mathbf{u}}] - \frac{1}{N} \sum_{\nu=1}^N F[\mathbf{u}^{(\nu)}]. \quad (7.7)$$

Although the existence of a potential f is not guaranteed for any reaction-diffusion model, only the derivatives occur in the following calculations, which are well defined for any model. A full variational treatment might have to include a potential of a different form.

7.3.2 Second order approximation

For a second order approximation of Eq. (7.7) let $\mathbf{u}^{(\nu)}$ be the minima of $F[\underline{\mathbf{u}}]$ and

$$\delta^{(\nu)} = \underline{\mathbf{u}} - \mathbf{u}^{(\nu)}. \quad (7.8)$$

This expression

$$F[\underline{\mathbf{u}}] = \frac{1}{N} \sum_{\nu=1}^N F[\mathbf{u}^{(\nu)} + \delta^{(\nu)}] \quad (7.9)$$

can be expanded in $\delta^{(\nu)}$:

$$\Delta F = \frac{1}{N} \sum_{\nu=1}^N \left(F[\mathbf{u}^{(\nu)} + \delta^{(\nu)}] - F[\mathbf{u}^{(\nu)}] \right) \approx \frac{1}{2N} \sum_{\nu=1}^N \delta^{(\nu)\text{T}} \left. \frac{\delta^2 F}{\delta \mathbf{u}^2} \right|_{\mathbf{u}=\mathbf{u}^{(\nu)}} \delta^{(\nu)} \quad (7.10)$$

and with the matrix elements

$$\underline{\underline{\mathbf{u}}}^{\nu} := \left. \frac{\delta^2 f}{\delta \mathbf{u}^2} \right|_{\mathbf{u}=\mathbf{u}^{(\nu)}}. \quad (7.11)$$

the resulting interaction energy in second order approximation would be

$$\Delta F = \frac{1}{2N^2} \sum_{\langle \nu\mu \rangle} \left[\left(\mathbf{u}^{(\nu)} - \mathbf{u}^{(\mu)} \right)^{\text{T}} \underline{\underline{\mathbf{u}}}^{\nu} \left(\mathbf{u}^{(\nu)} - \mathbf{u}^{(\mu)} \right) + \sum_i D_i \left(\nabla u_i^{(\nu)} - \nabla u_i^{(\mu)} \right)^2 \right], \quad (7.12)$$

where the sum denotes the sum over all pairs of patterns. With this result we can define the Hamiltonian

$$\mathcal{H} = \frac{1}{2N^2} \sum_{\langle \nu\mu \rangle} h_{\nu\mu} \quad (7.13)$$

with

$$h_{\nu\mu} = \int_V d\mathbf{r} \sum_{\langle \nu\mu \rangle} \left[\left(\mathbf{u}^{(\nu)} - \mathbf{u}^{(\mu)} \right)^{\text{T}} \underline{\underline{\mathbf{u}}}^{\nu} \left(\mathbf{u}^{(\nu)} - \mathbf{u}^{(\mu)} \right) + \sum_i D_i \left(\nabla u_i^{(\nu)} - \nabla u_i^{(\mu)} \right)^2 \right]. \quad (7.14)$$

For the LE model we have

$$\underline{\underline{\mathbf{u}}}^{\nu} = \begin{pmatrix} f_u & f_v \\ g_u & g_v \end{pmatrix} = \begin{pmatrix} -1 - 4v \frac{1-u^2}{(1+u^2)^2} & -4 \frac{u}{1+u^2} \\ \sigma b \left[1 - v \frac{1-u^2}{(1+u^2)} \right] & -\sigma b \frac{u}{1+u^2} \end{pmatrix}. \quad (7.15)$$

For the model in section 7.1 the matrix elements $h_{\nu\mu}$ would be a function of the rotational angle between two basic patterns ν and μ . The specific form of the function $h_{\nu\mu}$ could indicate a possible superposition if a minimum in the interaction energy between two patterns is found for appropriate regions of the parameter space.

7.3.3 Numerical results

In this section the matrix elements $h_{\mu\nu}$ are evaluated numerically for a part of the parameter space that shows homogeneous, hexagonal and lamellar stationary patterns. The form of the interaction energy in dependence of the rotational angle normalized to 2π is illustrated for a hexagonal and a lamellar pattern in Fig. 7.6. In general the functional form resembles the given examples, but the height of the plateau depends on the parameters of the state.

The interaction strength for the superposition of equal patterns, i.e. at $\alpha = 0$ and $\alpha = 1$ is zero as expected. It grows rapidly for intermediate values and forms a plateau with oscillations of small amplitude. The curves are symmetric around 180° , because the relative rotational angle between two similar patterns is always less than π . Minor deviations for rotation angles larger than π result from differences in the interpolation used in the rotation algorithm. Possible superposition of patterns could be indicated if the height of the plateau would significantly decrease in regions of the parameter space with stationary pattern formation. In Fig. 7.7 the value of $h_{\mu\nu}$ for $\alpha = 0.5$ as an approximation of the plateau height, is shown for a part of the parameter space, analyzed in chapter 4, where stationary hexagonal and lamellar patterns and homogeneous states are found.

The strength of the interaction remains zero for homogeneous patterns, as expected, because homogeneous patterns are rotationally invariant, so no difference in original and rotated patterns should be observed. Hexagonal and lamellar patterns occur in regions with lower and higher interaction energy, which could indicate a transition from stable stationary patterns in regions with large $h_{\mu\nu}$, where superposition require large energy, to chemical turbulence in the parameter space with smaller $h_{\mu\nu}$, where superpositions require less energy.

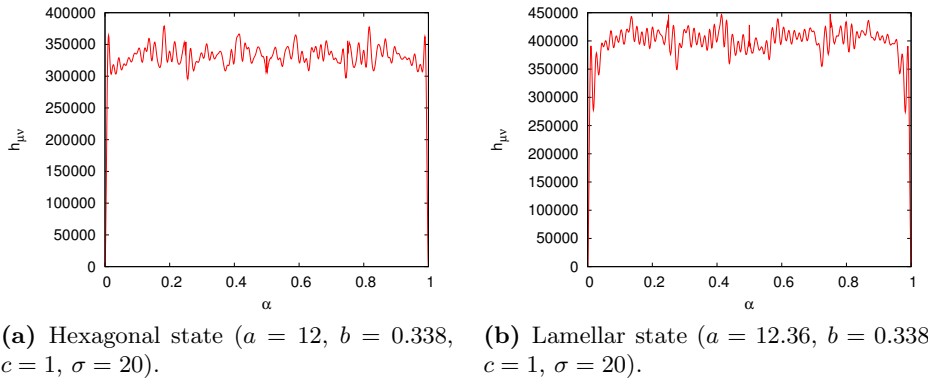


Figure 7.6: Interaction strength $h_{\mu\nu}$ between original and rotated patterns calculated numerically as a function of the rotational angle α for a hexagonal and a lamellar state.

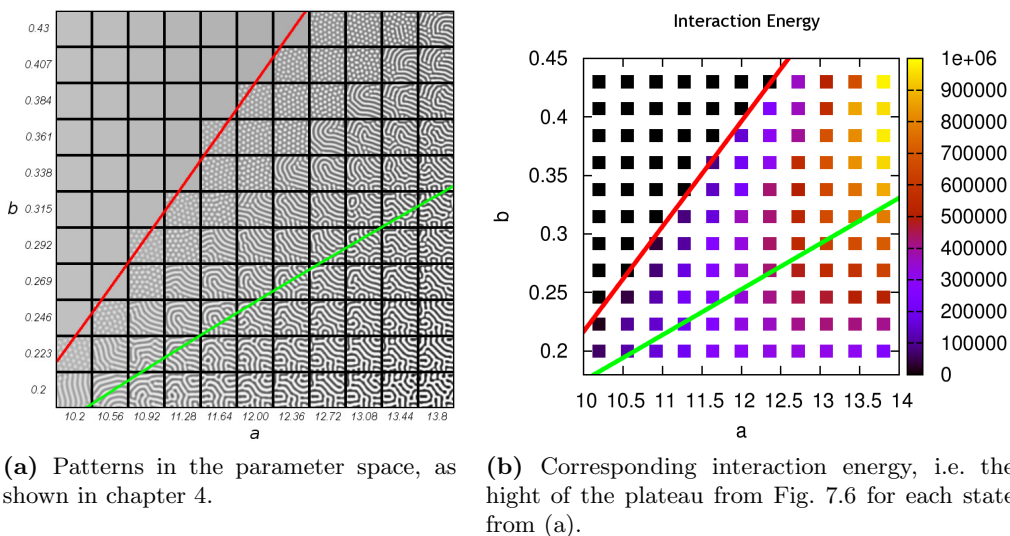


Figure 7.7: Interaction energy (b) in the IGP model calculated in the second order approximation for a region of the parameter space (a). Turing and Hopf Bifurcation are shown for convenience.

Although the numerical parameters for the LE model cannot be easily associated with the experimental parameters in the CIMA reaction, a transition from turbulent patterns to lamellar structures as found in the original CIMA experiment is indicated in Fig. 7.7. The parameter a is the only parameter in the LE model that is proportional to the concentration of malonic acid, as shown in section 2.2.1. As illustrated in Fig. 7.8 for $b = 0.246$ the interaction strength raises constantly from the Turing bifurcation until it reaches a saturation at $a = 13.8$. However the experiments indicate a first order phase transition, while the functional form of the numerical interaction energy yields a continuous phase transition [47]. However a continuous phase transition was also found in the CIMA experimental for sulfuric acid as a control parameter [37], which is treated as constant in the LE model. Also for a fixed parameter a a different transition in the interaction energy can be found numerically, with a rapidly falling intensity for increasing b , as shown in Fig. 7.8. While the relation between the experimental parameters in the CIMA reaction and the numerical parameters for the LE model is very complicated, depending on the actual three dimensional design of the experiment, a quantitative comparison could be possible for the parameter space of compartment concentrations in the CDIMA reaction.

7.4 Conclusion

The model presented here is intentionally kept as simple as possible. It demonstrates that the average morphology of the concentration profiles of experimental Turing

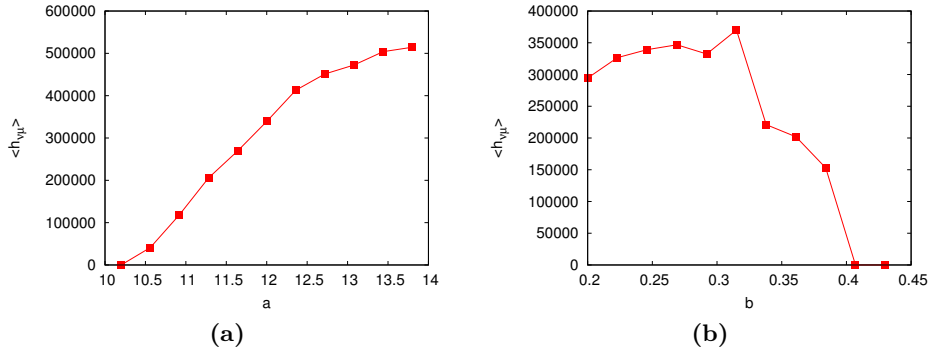


Figure 7.8: The value of the interaction energy from Fig. 7.7 shown for a fixed value of the parameters a and b respectively.

patterns is matched by a statistical superposition of randomly rotated deterministic patterns. This suggests a novel approach to pattern formation as a statistical mechanics problem. Additionally it explains, for the first time, the formation of turbulent patterns found in Ref. [47].

Evidently the hexagonal experimental patterns also show a “polycrystalline” character, i.e. regions that appear quite ordered separated by regions which are significantly unordered or blurred. This spatial heterogeneity is not incorporated in the model discussed here. However, the good agreement of the Minkowski functionals of experimental and superposed patterns shows that polycrystallinity is only of secondary relevance to the average measures.

The dynamics of the turbulent patterns could be included in the model by randomly fluctuating orientations in the superposed patterns. The distribution of amplitudes among the superposed patterns is an open question, however it could be answered by the analytic interaction pattern gas approach, which introduces a measure for the interaction energy between patterns.

Chapter 8

Summary and outlook

A quantitative analysis of patterns in the numerical LE model and experimental concentration profiles from the CIMA reaction reveal significant differences between the model and the experiment. These differences persist for all regions of the analyzed parameter space. Numerical analysis of other phenomenological reaction-diffusion models also indicates that the differences do not depend on the precise form of the reaction term in the LE model, but are generic to all analyzed reaction-diffusion models. This shows that deterministic reaction-diffusion models only partially capture pattern formation mechanisms in the CIMA reaction.

A local Minkowski analysis shows that the differences between experimental and numerical patterns are the result of unordered local parts in the experimental concentration profiles. This has not been considered in any other analysis of the experimental CIMA patterns. This leads to the assumption that a statistical model based on the superposition of basic patterns accounts for the observed differences, as unordered parts are the result of patterns that overlap out of phase, while ordered parts are observed when patterns overlap in phase.

A simplified model based on the statistical superposition of basic patterns from the LE model is suggested and produces patterns with good morphological agreement to the experimental patterns. The snapshots of turbulent patterns can be reproduced morphologically by the numerical model for sufficient parameters,

No other model has yet explained the formation of the turbulent states from Ref. [47]. As indicated in Ref. [53] only a very small region of the parameter space might produce stable spatio-temporal states, which consist of oscillating hexagons only and the spatio-temporal effects reported for the Brusselator in Ref. [10] are obviously morphologically different. The experiments however yield a large region in the parameter space where turbulent patterns occur. Furthermore the difference between stationary experimental and numerical patterns indicate that differences in the concentration profiles are not the result of spatio-temporal dynamics in the deterministic model, but of statistical origin.

The numerical model proposed in chapter 7 could be extended to a statistical distribution of amplitudes among the different superimposed patterns and include patterns of all states. The open question is how does this distribution depend on the experimental parameters. In order to answer this question the interaction between patterns has to be characterized quantitatively, which could be possible in the proposed interacting pattern gas (IPG) model.

Chapter 9

Pattern formation in granular systems

Pattern formation in a vertically shaken granular material is analyzed with a simple experimental setup. The types of patterns found agree well with those first found in Ref. [39]. This system is another example for nonlinear pattern formation albeit based on a different type of interaction than in the CIMA reaction.

9.1 Experimental setup

The experimental setup consists of function generator, a hifi-amplifier and a bass speaker. A circular bowl with a diameter of 12 cm and a flat ground is attached to the speaker membrane using silicone caulk. The bowl is filled with a thin layer of soldering balls, i.e. (60/40) tin-lead alloy beads 0.3 mm in diameter. The experimental setup is shown in Fig. 9.1

Adjustable parameters are the frequency and amplitude, i.e. the voltage of the driving signal and the height of the bead layer. To measure the amplitude of the membrane oscillations a thin black cardboard stripe has been attached to the bowl and photographed with bulb exposure over a few oscillations.

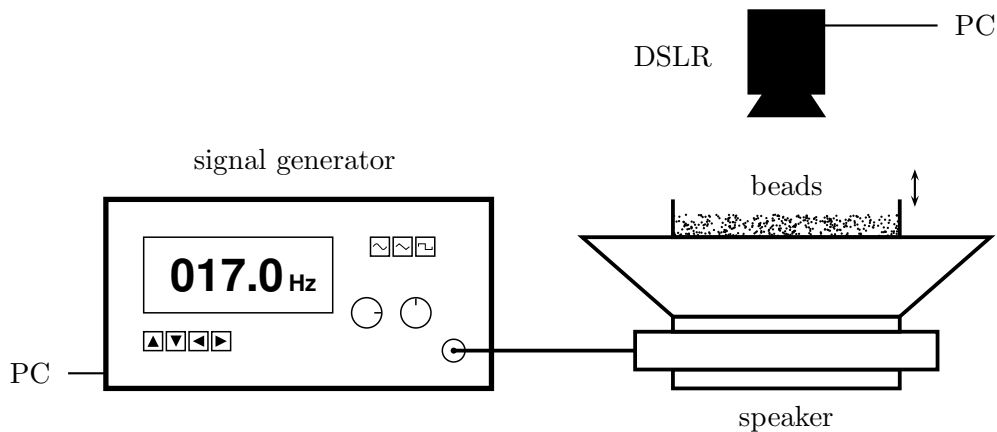


Figure 9.1: A signal generator drives a speaker at a given frequency and amplitude. A circular bowl with a diameter of 12 cm filled with beads is attached to the membrane. Measurements are taken via a digital SLR camera (DSLR). Signal and DSLR can be controlled remotely from a PC.

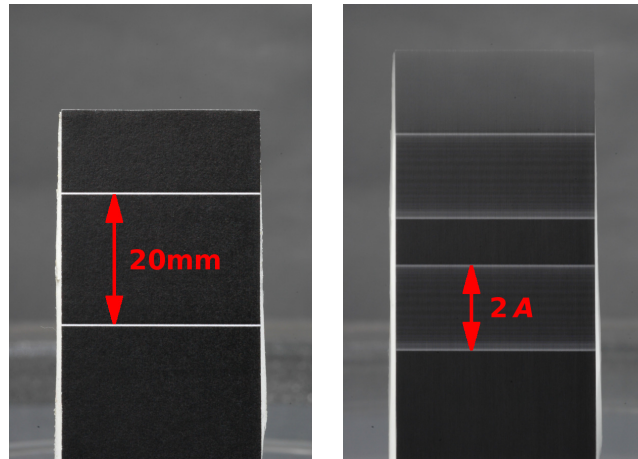


Figure 9.2: A cardboard stripe attached to the bowl is used to measure the amplitude of the oscillation for the calibration. The thin stripes form light regions due to bulb exposure over a few oscillations with a height of $2A$.

As shown in Fig. 9.2 the stripe has two white lines printed on the front, which act as reference length for the measure. Due to the bulb exposure those lines form light regions, whose height can easily be measured numerically.

9.2 Measurements and observed patterns

A series of measurements has been taken for frequencies between $f = 15\text{Hz} - 42\text{Hz}$ and amplitudes given by the dimensionless factor of $\Gamma = 2 - 10$, which is related to the amplitude of the oscillation by $\Gamma = 4\pi^2 f^2 A/g$, which can be obtained by a calibration measurement as described in the previous section. Different types of patterns, i.e. squares, lamellar and mixed patterns are observed, which agrees with [39].

Period doubling, with phase-separation, as reported in Ref. [40] can be observed for various pattern types, as shown in Fig. 9.4. Regions with opposite phase are separated by so-called kinks or interfaces, which are especially interesting when they separate two flat oscillating regions forming a zig-zag structure with small circular cells near the boundary line [4]. States with kinks also show hysteresis depending on frequency and amplitude [40].

The measurements reveal different pattern regions in the frequency-amplitude space. Figure 9.5 shows the observed pattern types. Localized phenomena, such as the stable oscillons found in Ref. [63], are not observed. An evacuated container might be needed for the formation of stable oscillons, as many phenomena in vertically shaken granular media are influenced by the surrounding gas, such as heap formation [13]. A more detailed overview on the topic can be found in Ref. [3], where also theoretical concepts and numerical simulations related to the experiment are discussed.

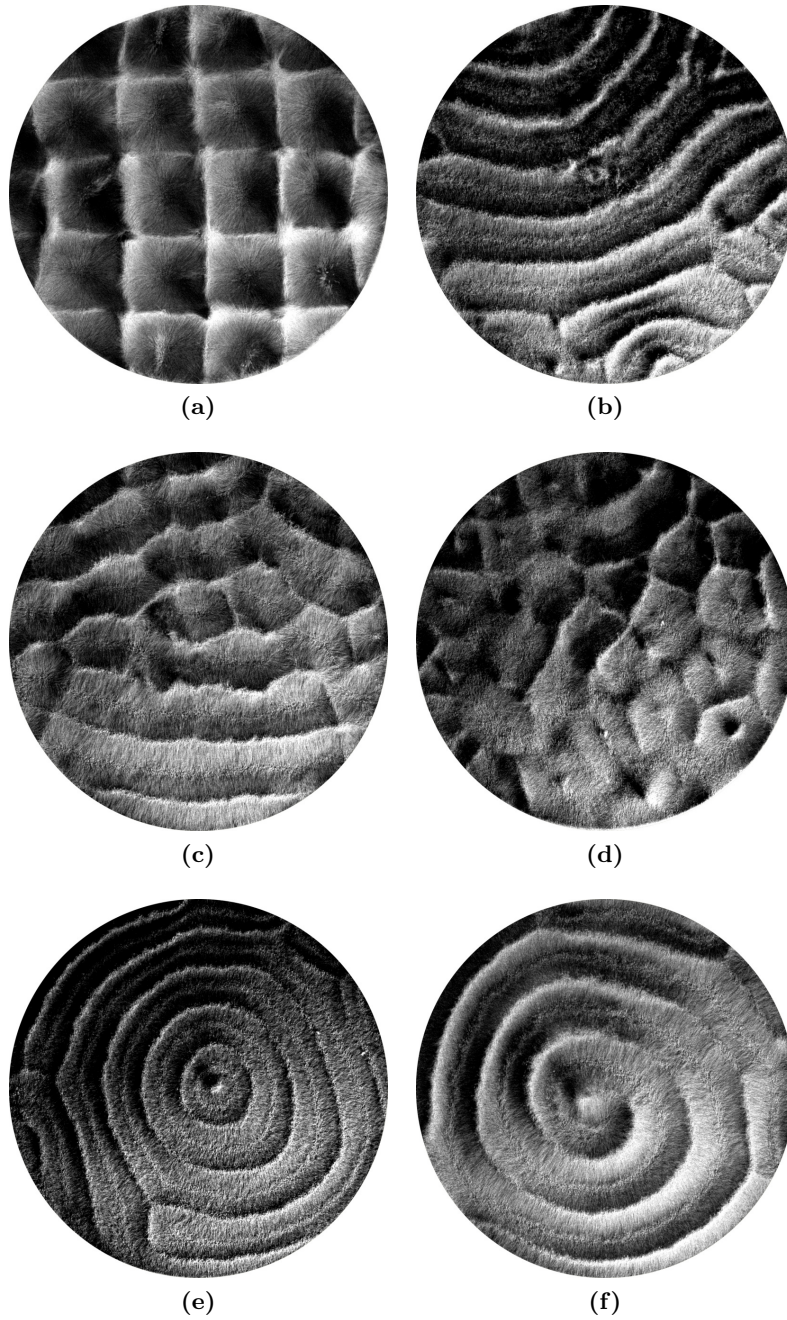


Figure 9.3: Patterns found for different parameters for a 2-3 mm deep layer: (a) square pattern ($f = 15\text{Hz}$, $\Gamma = 3.7$); (b) striped pattern ($f = 25\text{Hz}$, $\Gamma = 6.3$); (c) mixed pattern ($f = 20\text{Hz}$, $\Gamma = 4.1$); (d) mixed with hexagons ($f = 42\text{Hz}$, $\Gamma = 8.3$); (e) transient target pattern ($f = 27\text{Hz}$, $\Gamma = 5.1$); (f) transient spiral pattern ($f = 22\text{Hz}$, $\Gamma = 5.0$). The diameter of the patterns is about 12 cm.

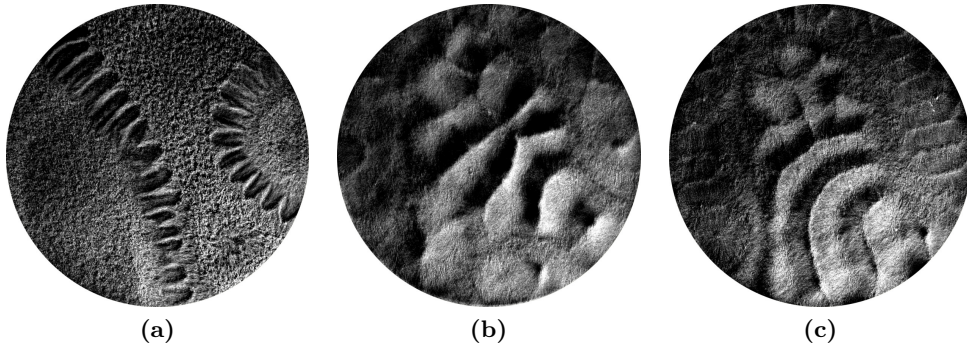


Figure 9.4: Flat surface and patterns with opposite phase separated by so called kinks: (a) flat with kinks ($f = 30\text{Hz}$, $\Gamma = 5.6$); (b) mixed with phase-separation ($f = 37\text{Hz}$, $\Gamma = 6.9$); (c) stripes with phase-separation ($f = 42\text{Hz}$, $\Gamma = 8.3$). The diameter of the patterns is about 12 cm.

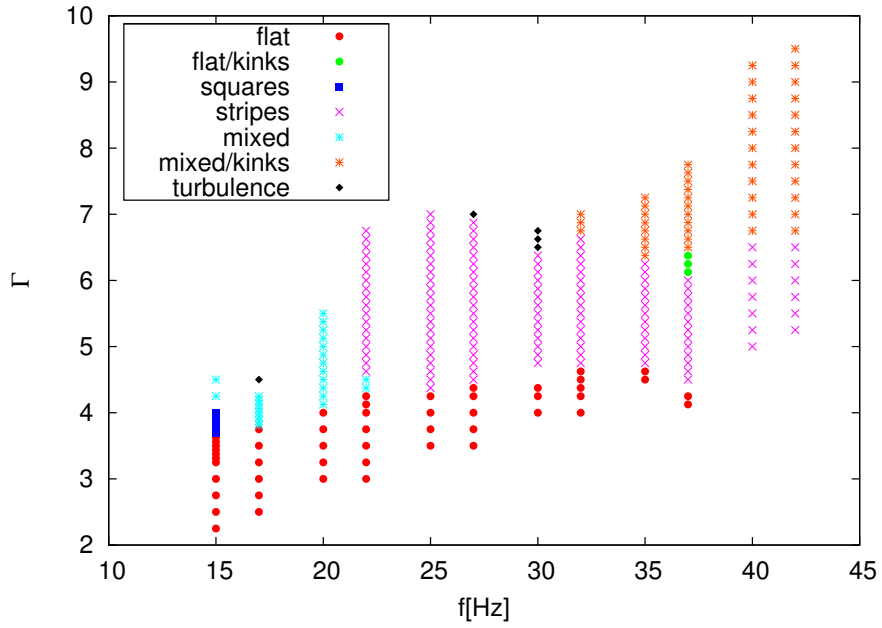


Figure 9.5: Pattern types in the parameter-space. Flat, squares, stripes and mixed states with and without kinks can be found.

Appendix A

Details on experimental datasets

The experimental CIMA concentration profiles used in this thesis are the original data of Klaus Mecke from Ref. [37], measured in the corresponding experiments by Qi Ouyang and Harry Swinney in Ref. [47]. Additional CDIMA concentration profiles are the original postscript files used in Ref. [54] Fig. 10 provided by Patrick De Kepper. The following list gives the name and path of each file for the corresponding figure in the thesis.

- Figs. 2.3, 5.6, 5.7: (a) phase-chaos.fig/cl20h100_2.pgm,
(b) t2_strp-chaos.fig/ma011_6.pgm,
(c) phase-chaos.fig/cl20h10_4.pgm
- Figs. 5.19, 5.20: (a) dk/dk-hex.pgm, (b) dk/dk-lam.pgm
- Figs. 6.3a, 7.3: phase-chaos.fig/cl20h100_2.pgm
- Figs. 6.3b, 6.4, 7.4: t2_strp-chaos.fig/ma011_6.pgm
- Fig. 7.5a: phase-chaos.fig/cl16h01_1.pgm
- Fig. 7.5b: t2_strp-chaos.fig/ma08_1.pgm

Bibliography

- [1] K. Agladze, E. Dulos, and P. De Kepper. Turing patterns in confined gel and gel-free media. *The Journal of Physical Chemistry*, 96:2400 – 2403, 1992.
- [2] E. J. Allen, S. J. Novosel, and Z. Zhang. Finite element and difference approximation of some linear stochastic partial differential equations. *Stochastics An International Journal of Probability and Stochastic Processes: formerly Stochastics and Stochastics Reports*, 64:117 – 142, 1998.
- [3] I. Aranson and L. Tsimring. *Granular Patterns*. Oxford University Press, USA, New York, hardback, 352 pages edition, 2009.
- [4] I. S. Aranson, D. Blair, W. K. Kwok, G. Karapetrov, U. Welp, G. W. Crabtree, V. M. Vinokur, and L. S. Tsimring. Controlled dynamics of interfaces in a vibrated granular layer. *Phys. Rev. Lett.*, 82(4):731–734, Jan 1999.
- [5] Philip Ball. *The Self-Made Tapestry: Pattern Formation in Nature*. Oxford University Press, USA, January 1999.
- [6] R. A. Barrio, C. Varea, J. L. Aragón, and P. K. Maini. A two-dimensional numerical study of spatial pattern formation in interacting Turing systems. *Bulletin of Mathematical Biology*, 61:483 – 505, 1999.
- [7] V. Castets, E. Dulos, J. Boissonade, and P. De Kepper. Experimental evidence of a sustained standing Turing-type nonequilibrium chemical pattern. *Phys. Rev. Lett.*, 64(24):2953 – 2956, Jun 1990.
- [8] M. D. Cowley and R. E. Rosensweig. The interfacial stability of a ferromagnetic fluid. *Journal of Fluid Mechanics Digital Archive*, 30(04):671–688, 1967.
- [9] P. De Kepper and I. R. Epstein. Mechanistic study of oscillations and bistability in the briggs-rauscher reaction. *Journal of the American Chemical Society*, 104:49 – 55, 1982.
- [10] A. De Wit, D. Lima, G. Dewel, and P. Borckmans. Spatiotemporal dynamics near a codimension-two point. *Phys. Rev. E*, 54(1):261–271, Jul 1996.
- [11] V. Dufiet and J. Boissonade. Conventional and unconventional Turing patterns. *The Journal of Chemical Physics*, 96(1):664–673, 1992.
- [12] Dulos E., Davies P., Rudovics B., and De Kepper P. From quasi-2d to 3d Turing patterns in ramped systems. *Physica D*, 98:53 – 66, 1 November 1996.

- [13] P. Evesque and J. Rajchenbach. Instability in a sand heap. *Phys. Rev. Lett.*, 62(1):44–46, Jan 1989.
- [14] R. FitzHugh. Impulses and physiological states in theoretical models of nerve membrane. *Biophysical Journal*, 1:445 – 466, 1961.
- [15] A. Gierer and H. Meinhardt. A theory of biological pattern formation. *Biological Cybernetics*, 12:30 – 39, 1972.
- [16] P. Glansdorff and I. Prigogine. *Thermodynamic Theory of Structure, Stability and Fluctuations*. Wiley, 1971.
- [17] G. H. Gunaratne, Q. Ouyang, and H. L. Swinney. Pattern formation in the presence of symmetries. *Phys. Rev. E*, 50(4):2802 – 2820, Oct 1994.
- [18] H. Holden, B. Oksendal, J. Uboe, and T. Zhang. *Stochastic partial differential equations: a modeling, white noise functional approach*. Birkhauser Boston Inc., Cambridge, MA, USA, 1996.
- [19] J. Horvath, I. Szalai, and P. De Kepper. An Experimental Design Method Leading to Chemical Turing Patterns. *Science*, 324(5928):772–775, 2009.
- [20] O. Jensen, E. Mosekilde, P. Borckmans, and G. Dewel. Computer simulation of Turing structures in the chlorite-iodide-malonic acid system. *Physica Scripta*, 53(2):243–251, 1996.
- [21] O. Jensen, V. O. Pannbacker, E. Mosekilde, G. Dewel, and P. Borckmans. Localized structures and front propagation in the lengyel-epstein model. *Phys. Rev. E*, 50(2):736–749, Aug 1994.
- [22] D. M. Kern and C. Kim. Iodine catalysis in the chlorite-iodide reaction. *Journal of the American Chemical Society*, 87:5309 – 5313, 1965.
- [23] P. E. Kloeden and E. Platen. *Numerical solution of stochastic differential equations*. Springer-Verlag, Berlin ; New York, 1992.
- [24] K. J. Lee, W. D. McCormick, Q. Ouyang, and H. L. Swinney. Pattern Formation by Interacting Chemical Fronts. *Science*, 261(5118):192 – 194, 1993.
- [25] I. Lengyel and I. R. Epstein. Modeling of Turing Structures in the Chlorite–Iodide–Malonic Acid–Starch Reaction System. *Science*, 251(4994):650–652, 1991.
- [26] I. Lengyel and I. R. Epstein. A chemical approach to designing Turing patterns in reaction-diffusion systems. *Proceedings of the National Academy of Sciences of the United States of America*, 89(9):3977 – 3979, 1992.
- [27] I. Lengyel, S. Kádár, and I. R. Epstein. Quasi-two-dimensional Turing patterns in an imposed gradient. *Phys. Rev. Lett.*, 69(18):2729 – 2732, Nov 1992.

- [28] I. Lengyel and J. A. Pojman. *An Introduction to Nonlinear Chemical Dynamics: Oscillations, Waves, Patterns, and Chaos*. Oxford University Press, USA, New York, ninth dover printing, tenth gpo printing edition, 1998.
- [29] I. Lengyel, G. Rabai, and I. R. Epstein. Experimental and modeling study of oscillations in the chlorine dioxide-iodine-malonic acid reaction. *Journal of the American Chemical Society*, 112:9104 – 9110, 1990.
- [30] I. Lengyel, G. Rabai, and I. R. Epstein. Systematic design of chemical oscillators. part 65. batch oscillation in the reaction of chlorine dioxide with iodine and malonic acid. *Journal of the American Chemical Society*, 112:4606 – 4607, 1990.
- [31] T. Leppänen, M. Karttunen, R. A. Barrio, and K. Kaski. The effect of noise on Turing patterns. *Progress of Theoretical Physics Supplement*, 150:367 – 370, 2003.
- [32] T. Leppänen, M. Karttunen, R. A. Barrio, and K. Kaski. Morphological transitions and bistability in Turing systems. *Phys. Rev. E*, 70(6):066202, Dec 2004.
- [33] T. Leppänen, M. Karttunen, K. Kaski, R. A. Barrio, and L. Zhang. A new dimension to Turing patterns. *Physica D: Nonlinear Phenomena*, 168 – 169:35 – 44, 2002.
- [34] Q. Li, C-G. Zheng, N-C. Wang, and B-C. Shi. LBGK simulations of Turing patterns in cima model. *Journal of Scientific Computing*, 16:121–134(14), June 2001.
- [35] H. Mantz, K. Jacobs, and K. R. Mecke. Utilizing Minkowski functionals for image analysis: a marching square algorithm. *Journal of Statistical Mechanics: Theory and Experiment*, 2008(12):P12015 (29pp), 2008.
- [36] Edward A. McGehee and Enrique Peacock-López. Turing patterns in a modified lotka-volterra model. *Physics Letters A*, 342(1-2):90 – 98, 2005.
- [37] K. R. Mecke. Morphological characterization of patterns in reaction-diffusion systems. *Phys. Rev. E*, 53(5):4794 – 4800, May 1996.
- [38] K. R. Mecke. Integral geometry in statistical physics. *International Journal of Modern Physics B*, 12:861 – 899, 1998.
- [39] F. Melo, P .B. Umbanhowar, and H. L. Swinney. Transition to parametric wave patterns in a vertically oscillated granular layer. *Phys. Rev. Lett.*, 72(1):172 – 175, Jan 1994.
- [40] F. Melo, P. B. Umbanhowar, and H. L. Swinney. Hexagons, kinks, and disorder in oscillated granular layers. *Phys. Rev. Lett.*, 75(21):3838 – 3841, Nov 1995.

- [41] W. Mickel, S. Münster, L. M. Jawerth, D. A. Vader, D. A. Weitz, A. P. Sheppard, K. Mecke, B. Fabry, and G. E. Schröder-Turk. Robust pore size analysis of filamentous networks from three-dimensional confocal microscopy. *Biophysical Journal*, 95:6072 – 6080, 2008.
- [42] D. G. Miguez, S. Alonso, A. P. Munuzuri, and F. Sagues. Experimental evidence of localized oscillations in the photosensitive chlorine dioxide-iodine-malonic acid reaction. *Physical Review Letters*, 97(17):178301, 2006.
- [43] J. D. Murray. *Mathematical Biology I. An Introduction*. Springer Science+Business Media, LCC, New York, 3rd ed. 2002. corr. 2nd printing, 2008, xxiii, 551 p. 164 illus., hardcover edition, 2002.
- [44] J. D. Murray. *Mathematical Biology II. Spatial Models and Biomedical Applications*. Springer Science+Business Media, LCC, New York, 3rd ed. 2003. corr. 2nd printing, 2008, xxv, 811 p. 296 illus., hardcover edition, 2003.
- [45] Q. Ouyang, G. H. Gunaratne, and H. L. Swinney. Rhombic patterns: Broken hexagonal symmetry. *Chaos: An Interdisciplinary Journal of Nonlinear Science*, 3(4):707–711, 1993.
- [46] Q. Ouyang, Z. Noszticzius, and Harry L. Swinney. Spatial bistability of two-dimensional Turing patterns in a reaction-diffusion system. *The Journal of Physical Chemistry*, 96:6773 – 6776, 1992.
- [47] Q. Ouyang and H. L. Swinney. Transition to chemical turbulence. *Chaos: An Interdisciplinary Journal of Nonlinear Science*, 1(4):411 – 420, 1991.
- [48] B. Peña and C. Pérez-García. Stability of Turing patterns in the Brusselator model. *Phys. Rev. E*, 64(5):056213, Oct 2001.
- [49] J. E. Pearson. Complex patterns in a simple system. *Science*, 261(5118):189 – 192, 1993.
- [50] William Press, Saul Teukolsky, William Vetterling, and Brian Flannery. *Numerical Recipes in C*. Cambridge University Press, Cambridge, UK, 2nd edition, 1992.
- [51] S. Rehse, K. Mecke, and R. Magerle. Characterization of the dynamics of block copolymer microdomains with local morphological measures. *Physical Review E (Statistical, Nonlinear, and Soft Matter Physics)*, 77(5):051805, 2008.
- [52] T. Reichenbach, M. Mobilia, and E. Frey. Self-organization of mobile populations in cyclic competition. *Journal of Theoretical Biology*, 254(2):368 – 383, 2008.
- [53] A. Rovinsky and M. Menzinger. Interaction of Turing and Hopf bifurcations in chemical systems. *Phys. Rev. A*, 46(10):6315 – 6322, Nov 1992.

- [54] B. Rudovics, E. Barillot, P. W. Davies, E. Dulos, J. Boissonade, and P. De Kepper. Experimental studies and quantitative modeling of Turing patterns in the (chlorine dioxide, iodine, malonic acid) reaction. *The Journal of Physical Chemistry A*, 103(12):1790 – 1800, 1999.
- [55] B. Rudovics, E. Dulos, and P. De Kepper. Standard and nonstandard Turing patterns and waves in the cima reaction. *Physica Scripta*, T67:43–50, 1996.
- [56] M. Saitou and Y. Fukuoka. Stripe pattern formation in ag-sb co-electrodeposition. *Electrochimica Acta*, 50(25-26):5044 – 5049, 2005. Electrochemistry: from Nanostructures to Power Plants - Selection of papers from the 55th Annual Meeting of the International Society of Electrochemistry (ISE)19-24 September 2004, Thessaloniki, Greece.
- [57] J. Schnakenberg. Simple chemical reaction systems with limit cycle behaviour. *Journal of Theoretical Biology*, 81(3):389 – 400, 1979.
- [58] H. Shoji, K. Yamada, and T. Ohta. Interconnected turing patterns in three dimensions. *Phys. Rev. E*, 72(6):065202, Dec 2005.
- [59] S. H. Strogatz. *Nonlinear Dynamics and Chaos: With Applications to Physics, Biology, Chemistry and Engineering*. Perseus Books,U.S., illustrated edition edition, 2000.
- [60] D. Thomas. *Artificial membranes: transport, memory, and oscillatory phenomena*. In: *Analysis and Control of Immobilized Enzyme Systems*. Springer-Verlag, Berlin-Heidelberg-New York, 1975.
- [61] A. M. Turing. The chemical basis of morphogenesis. *Philosophical Transactions of the Royal Society of London. Series B, Biological Sciences*, 237(641):37 – 72, 1952.
- [62] R. Tyson, S. R. Lubkin, and J. D. Murray. A minimal mechanism for bacterial pattern formation. *Proceedings of the Royal Society of London. Series B: Biological Sciences*, 266(1416):299 – 304, 1999.
- [63] P. B. Umbanhowar, F. Melo, and H. L. Swinney. Localized excitations in a vertically vibrated granular layer. *Nature*, 382:796 – 769, 1996.
- [64] V. Volterra. Variations and fluctuations of the number of individuals in animal species living together. *Animal Ecology*, 1931.
- [65] N. Wiberg, A. Holleman, and E. Wiberg. *Holleman-Wiberg's Inorganic Chemistry*. Academic Press, paperback, 1924 pages edition, 2001.
- [66] Y-N. Wu, P-J. Wang, C-J. Hou, C-S. Liu, and Z-G. Zhu. Turing patterns in a reaction-diffusion system. *Communications in Theoretical Physics*, 45(4):761–764, 2006.

- [67] L. Yang, M. Dolnik, A. M. Zhabotinsky, and I. R. Epstein. Spatial resonances and superposition patterns in a reaction-diffusion model with interacting Turing modes. *Phys. Rev. Lett.*, 88(20):208 – 303, May 2002.

Erklärung

Hiermit bestätige ich, dass ich diese Arbeit selbstständig verfasst, sowie keine anderen als die angegebenen Quellen und Hilfsmittel benutzt habe.

Erlangen, den 11. August 2009

Christian Scholz